

9. SITE 1228¹

Shipboard Scientific Party²

BACKGROUND AND OBJECTIVES

Site 1228 was one of three Leg 201 sites selected for drilling on the continental shelf of Peru. These shelf sites were collectively selected to provide records of microbial activities, communities, and geochemical consequences in organic-rich ocean-margin sediments.

The principal objectives at this site were

1. To test by comparison with other sites drilled during this expedition whether microbial communities, microbial activities, and the nature of microbe-environment interactions are different in organic-rich ocean-margin sediments than in open-ocean sediments with less organic matter and
2. To test how the presence of sulfate-bearing subsurface brine affects microbial activities, microbial communities, and microbial influence on environmental properties in organic-rich, sulfate-rich sediments.

Site 1228 is in the immediate vicinity of Leg 112 Site 680. As described in "**Principal Results**," p. 2, in the "Site 1227" chapter, geochemical studies of Leg 112 sites show that brine is present below the seafloor in the Trujillo and Salaverry Basins (Suess, von Huene, et al., 1988). Interestingly, at Site 680 the deep brine source of sulfate prevents the interstitial water concentration of sulfate from becoming depleted at any depth. Site 1228 therefore provides an opportunity to study how the introduction of sulfate-bearing brine affects subseafloor life in organic-rich, sulfate-rich sediments. Consequently, it provides an excellent standard of comparison for Sites 1227 and 1229, which are, respectively, affected by the intrusion of sulfate-free brine and sulfate-rich brine into organic-rich, sulfate-depleted sediments.

¹Examples of how to reference the whole or part of this volume.

²Shipboard Scientific Party addresses.

Site 1228 is located in 252 m water depth on the outer shelf edge in the middle of the modern oxygen minimum zone of the Peruvian high-productivity upwelling system. At this depth on the Peru shelf, an oxidized sediment zone is practically absent at the sediment/water interface and sulfate reduction is the predominant mineralization process to the very surface (Rowe and Howarth, 1985; Fossing, 1990; Parkes et al., 1993). The organic content is high at Site 680 (3%–10% total organic carbon [TOC]), and sulfate reduction rates are still detectable with radiolabeled sulfate in samples taken from as deep as 80 meters below seafloor (mbsf) (Parkes et al., 1990).

The lithologic and physical properties at Site 680 change strongly through the 200-m-deep interval drilled during Leg 112 (Shipboard Scientific Party, 1988b). The sediment mainly consists of diatom mud in the upper 50 m of the Pleistocene deposit. Below 50 mbsf, the terrestrial component of the mud is higher but the sediment is primarily biogenic. The lower part of the sediment column consists of a coarse-grained phosphate and feldspar gravel interpreted as drilling artifacts overlying coarse-grained sand cemented by dolomite (Shipboard Scientific Party, 1988b). Dolomite is the primary authigenic phase, but calcite and apatite are also common.

Shipboard chemical analyses from Leg 112 indicate that concentrations of methane at Site 680 are in the range of 10–100 $\mu\text{L/L}$ (0.4–4 μM) in the upper 100 m of the sediment column. Methane was not analyzed at greater depths at Site 680. Concentrations of dissolved sulfate decline from a near-seawater value to a minimum of 6 mM over the uppermost ~50 mbsf and then rise toward higher values in the underlying sediment as a result of diffusion from the underlying sulfate-rich brine (Shipboard Scientific Party, 1988b). A peak sulfide concentration is present between 20 and 40 mbsf (Mossman et al., 1990). Sulfide concentrations were not measured in deeper portions of the underlying brine-affected interval.

Chloride concentrations increase steadily to the base of the hole, and ammonium steadily increases to at least 80 mbsf. Alkalinity exhibits a maximum value at 20 mbsf. Concentrations of calcium and magnesium exhibit minimum values at 5 and 20 mbsf, respectively, and then increase steadily to the base of the hole. The magnesium/calcium ratio peaks at ~5 mbsf and also steadily declines to the base of the hole (Shipboard Scientific Party, 1988b; Kastner et al., 1990).

These downhole profiles of dissolved chemical concentrations are inferred to result from relatively high levels of biological activity throughout the sediment column, coupled with diffusive exchange with the overlying ocean water and with a sulfate-bearing brine introduced at depth. Prokaryotic cell counts and activities were studied to a depth of 9.1 mbsf at Site 680. Nearly 10^9 cells/mL were present in all samples analyzed. In most probable number (MPN) cultivation studies, 10^1 to 10^5 cells/mL were found to be viable (Cragg et al., 1990; Parkes et al., 1990). The subsurface extent of key electron donors (hydrogen, acetate, and formate) and electron acceptors with standard free-energy yields greater than that of sulfate (oxygen, nitrate, manganese oxide, and iron oxides) was not determined for Site 680.

PRINCIPAL RESULTS

Continuous advanced hydraulic piston corer (APC) coring from the seafloor to 200 mbsf enabled high-quality sampling for geochemistry

and microbiology throughout the drilled sediment column of Site 1228. Because of the overall predominance of sulfate reduction in the highly sulfidic sediment and the presence of sulfate throughout the sediment column, there were no distinct chemical interfaces to target in the sampling scheme for Site 1228. Concentrations of chloride range linearly from a typical seawater concentration at 0 mbsf to twice the seawater concentration at 200 mbsf. This linear profile demonstrates the long-term stability of brine diffusion and provides a reference for all other interstitial water constituents. Analyzed nonconservative species that are affected by microbial activity in the subsurface included sulfate, dissolved inorganic carbon (DIC), and ammonium. Interstitial water analyses at high depth resolution show unexpected details with implications for both the rates of long-term processes and for more recent changes.

Sulfate reduction in the upper 50 m of the sediment column is not sufficient to deplete sulfate at depth. The overall sulfate distribution shows a steep drop in concentrations over the first few meters below the sediment/water interface, a sigmoidal curve in dissolved sulfate concentrations over the following 10 m, a decrease to 2.5 mM at 38 mbsf, and then a continuous increase to 30 mM at 200 mbsf. The sigmoidal curve of the first 10 m indicates that the near-surface distribution of sulfate reduction and/or transport processes changed strongly in geologically recent time and that diffusion through the sediment column has not yet fully adjusted to a new steady state. The continuous increase in sulfate concentrations from 40 to 200 mbsf results from upward diffusion of the underlying sulfate-rich brine.

The depth profiles of DIC and ammonium closely match the described sulfate distribution. The overall DIC profile reveals a distinct DIC maximum of 19 mM at 2 mbsf, a decline to 15 mM, a rise to a second, broader maximum of 20 mM at 25 mbsf, and then a gradual downhole decrease to 4 mM. Ammonium similarly increases from ~2000 μM near the sediment surface to a local maximum of 2600 μM at 2 mbsf, declines slightly, and then increases gradually to 5000 μM downhole. Comparison to Site 680 biochronostratigraphic data (Shipboard Scientific Party, 1988b) suggests that the sediment that contains the DIC and ammonium maxima may have been deposited a few tens of thousands of years ago. These near-surface interstitial water anomalies indicate that steady-state diffusion of biologically active chemicals past the upper sediment column was disrupted by late Pleistocene environmental change and has not yet fully recovered. The exact nature of these changes will be analyzed when a more complete data set becomes available.

Concentrations of manganese and iron in the interstitial water are extremely low ($<0.1 \mu\text{M}$) down to ~60–80 mbsf. Below this depth, they increase gradually to ~10 μM (manganese) and 50 μM (iron) at 200 mbsf. The source of these dissolved metals at depth may be either diffusion from below or in situ manganese or iron reduction in the lower sediment column.

In contrast to most other ocean-margin sites, including Site 1227, a sulfate/methane interface is absent from the sediment of Site 1228. Methane concentrations remain low throughout the 200-m sediment column, reaching a maximum of only 8 μM . Yet, the distribution of methane clearly reflects the sulfate distribution, with a maximum coinciding with the sulfate minimum and a general inverse correlation between sulfate and methane concentrations throughout the sediment column. These results indicate that even at a concentration above 9%

of its seawater level (minimum = 2.5 mM; seawater = 28.9 mM), sulfate regulates the ability of methane-oxidizing consortia to take up methane and maintain a low background concentration. In this respect, Site 1228 provides a unique opportunity to analyze the energetics of anaerobic oxidation of methane and to test current theories of the limiting parameters for this key microbial process.

Acetate and formate are important fermentation products as well as substrates for sulfate-reducing bacteria. Their concentrations in this organic-rich shelf sediment are tenfold higher than in deep-sea sediments of the tropical Pacific (Sites 1225 and 1226) but only about one-half their concentrations at Peru shelf Site 1227. The Site 1228 data show considerable scatter with depth. Acetate concentrations fall mostly in the range of 1–4 μM and formate concentrations in the range of 0.5–3 μM . The higher concentrations of both fatty acids are present below 100 mbsf. These concentrations are regulated by uptake mechanisms that are not yet fully understood.

Interestingly, the depth of the distinct sulfate minimum at ~40 mbsf is present in an interval of strong lithologic and physical change. At this depth, the sediment shifts from a diatomaceous silt of predominantly hemipelagic origin to older quartz- and feldspar-bearing silt with a more abundant terrestrial component. At 43 mbsf, there is a distinct minimum in porosity and maxima in density, thermal conductivity, and magnetic susceptibility. It is intriguing to speculate that such a physical boundary may temporarily lock the position of biogeochemical zonations in the sediment column.

The temperature gradient in the Site 1228 sediment column was defined from two discrete temperature measurements taken with the Davis-Villinger Temperature Probe (DVTP). The results were combined with Leg 112 data to define a linear temperature gradient of 34°C/km and a heat flow of 32 mW/m². This heat flow estimate is lower than the 46 mW/m² estimated for Site 680 by the Leg 112 Shipboard Scientific Party (1988b) and confines the previous broad estimate of 20–70 mW/m² for this site (Yamano and Uyeda, 1990). The temperature increases down through the sediment column from an estimated annual mean of 12.5°C at the seafloor to an extrapolated 19.3°C at 200 mbsf. These temperatures are all within the low mesophilic range for prokaryotes.

Samples were taken for total counts, viable (MPN) counts, and isolations of prokaryotes from selected depths throughout the sediment column. Because of the short transfer time between Sites 1227, 1228, and 1229, the acridine orange direct counts (AODCs) of total prokaryotic cell numbers at Site 1228 will be conducted postcruise. A large number of MPN samples and isolation incubations target a broad physiological spectrum of heterotrophic and autotrophic prokaryotes that utilize diverse electron acceptors and donors in their energy metabolism. The selective influence of increased salinity and brine composition is also targeted in some incubations. The expected slow growth of deep subsurface prokaryotes will require long postcruise incubation of samples before definite results are obtained from these experiments. This is also the case for the many experiments on microbial processes measured by radiotracer techniques on samples taken from throughout the entire sediment column.

Because the absence of prokaryotic cell contamination from drilling and sampling operations is critical for the isolation of indigenous prokaryotes and measurement of their activities, a perfluorocarbon tracer (PFT) was continuously added to the drilling water. Tracer samples were taken on the catwalk or in the laboratory from all core sec-

tions and subsamples used for microbiology. It was demonstrated that PFT concentrations are typically higher at the periphery than at the sampled center of whole-round core segments. The microbiology subsamples had PFT concentrations below or near the detection limit. This limit corresponds to the potential introduction of 0.01 μL seawater/g sediment. Such seawater introduction could maximally introduce 5 cells/g, based on the mean cell density in seawater (5×10^{-8} cells/L). An additional contamination test uses fluorescent microbeads dispersed on impact at the head of the core barrel. At Site 1228, this test consistently indicates that contamination is unlikely. This method releases 2×10^{11} prokaryote-sized beads at the most sensitive position during drilling, and the tests on microbiological samples showed no beads or, at most, one bead in the >60 microscopic fields of view routinely scanned. The extensive contamination tests applied at this site thus confirm the high quality of microbiology samples that can be taken by careful techniques from APC cores without visible disturbance.

OPERATIONS

Transit to Site 1228

The 167-nmi transit between Sites 1227 and 1228 took 15.8 hr at an average speed of 10.6 kt. A positioning beacon was deployed at 1900 hr on 3 March 2002, ~75 m north of the Global Positioning System coordinates of Site 680, as reported on the first page of the Site 680 chapter in the Leg 112 *Initial Reports* volume (Shipboard Scientific Party, 1988b) and corroborated by the Ocean Drilling Program (ODP) Drilling Services Department operations report for Leg 112, in 273.6 m water depth (below rig floor). The vessel was moved to a position 50 m north of these coordinates to begin operations at Site 1228.

Hole 1228A

Continuous APC coring was initiated with Core 1H, which arrived on deck at 2155 hr on 3 March. Coring continued through Core 23P (0.0–200.9 mbsf) (recovery = 68%). Cores 1H through 8H (0.0–71.4 mbsf) had average recovery >100%, with the exception of Core 5H (recovery = 80%). Core 6H had a full core barrel but the liner was shattered, resulting in a severely disturbed core. Cores 9H through 23P (71.4–200.9 mbsf) were variably successful in terms of recovery, ranging from empty barrels (Core 17H), to poor-recovery intervals with soupy cores (Cores 11H, 12H, 15H; recovery = <20% for all), to cores with as much as 95% recovery of intact sediment. Core 10H did not advance and returned to the rig floor with the shear pins scored but not broken. We interpreted this to suggest that the bit was resting on a hard layer, obstructing penetration of the barrel. The core barrel was deployed again with the bit raised to 1 m off bottom so as to provide momentum for the piston core prior to penetration. The barrel still would not extend beyond the bit, indicating that there was an obstruction inside the throat of the bottom-hole assembly. An extended core barrel (XCB) was deployed to dislodge the obstruction, but the subsequent APC barrel (still identified as Core 10H) only pushed a short distance out of the bit and returned an intensely disturbed, low-recovery core. We drilled to the equivalent depth of a full piston stroke (9.5 m) and deployed Core 11H, which also misfired because of impact with a hard interval, and re-

turned a core in much the same condition as the previous one, comprising a mixture of mud, sand, and gravel. While discussing our operational strategy, we deployed the Fugro Percussion Corer (FPC) (Core 13M) (109.4–110.4 mbsf; recovery = 40%), which returned a collapsed core barrel partially filled with gravel at ambient pressure.

Since our science objectives would be better served with a few meters of intact APC recovery than with any partial recovery the XCB might return, we chose to continue APC advancement, recovering what material we could and drilling down through multiple hard intervals. Recovery was sporadic (Cores 14H through 22H; 110.4–194.9 mbsf) (see Table T1), but in most cases we recovered sufficient intact core to meet our microbiological and geochemical objectives. Hole 1228A was terminated when the pressure coring sampler (PCS) cutting shoe dislodged and stuck in the bottom of the hole.

The DVTP was deployed at 42.9, 80.9, 137.9, and 194.9 mbsf, and the Davis-Villinger Temperature-Pressure Probe (DVTP-P) was deployed at 99.9 and 196.9 mbsf. We attempted twice to collect bottom-water samples with the Water Sampling Temperature Probe (WSTP) just above the mudline before beginning operations and after Core 1H, but both attempts suffered mechanical failure. A mudline temperature was measured with the Adara temperature tool before collecting Core 1H. A logging run with the triple combination (triple combo) tool string was completed in Hole 1228A. PFT was pumped continually during all coring operations at Site 1228 as part of our microbiological contamination testing protocol. In addition, fluorescent microspheres were deployed on Cores 2H, 5H, 11H, and 12H to help assess the potential of contamination in cores where heavy microbiological sampling was planned.

Holes 1228B, 1228C, 1228D, and 1228E

Since the location of the positioning beacon was ~20 m due north of the location of Hole 1228A and we were operating in shallow water, we were required to arrange our subsequent occupations relatively close to the beacon, while avoiding drilling into it. Offsets of 22 m north-northeast, 13 m north-northwest, 12 m northwest, and 20 m north were chosen for Holes 1228B, 1228C, 1228D, and 1228E, respectively.

Hole 1228B comprised six continuous APC cores (Cores 201-1228B-1H through 6H; 0.0–54.3 mbsf) (recovery = 107%). The upper five cores were sampled for shipboard high-resolution paleoceanography and paleomagnetism objectives. In addition, Core 201-1228B-6H was taken to fill gaps in the continuous geochemical and microbiological profile from Hole 1228A. The FPC was deployed at the bottom of Hole 1228B (Core 201-1228B-7M; 54.3–55.0 mbsf) and recovered 0.42 m of sediment.

The last three holes drilled at this site were cored for high-resolution shore-based sampling (Hole 1228D; Cores 201-1228D-1H through 3H [0.0–27.0 mbsf; recovery = 101%]) and shipboard geochemistry and microbiology (Hole 1228C; Core 201-1228C-1H; 0.0–7.5 mbsf [recovery = 100%], and Hole 1228E; Core 201-1228E-1H; 0.0–7.3 mbsf [recovery = 100%]). A WSTP sample was collected above the mudline in Hole 1228E. The FPC was deployed at the bottom of Hole 1228E (Core 201-1228E-2M; 7.3–8.3 mbsf). In addition to continuous PFT contamination monitoring, fluorescent microspheres were deployed on Core 201-1228E-1H. Operations at Site 1228 ended when the bit passed through

T1. Coring summary, Site 1228, p. 60.

the rig floor at 1200 hr on 6 March, and we began our short transit to Site 1229.

LITHOSTRATIGRAPHY

At Site 1228, we recovered a 200.9-m-thick sequence of biogenic and siliciclastic Pleistocene and Pliocene sediments that were deposited on the Peruvian shelf. Based on textural, color, and compositional variations, sediments from Site 1228 were divided into two lithostratigraphic units (Fig. F1). The proposed lithostratigraphy is mostly based on Hole 1228A, as it was the only hole at Site 1228 that was continuously cored from the sediment surface to a depth of 200.9 mbsf. The lithostratigraphic description of the sedimentary sequence is based on visual observation of sediment color and sedimentary structures (visual core description), smear slide analysis, and color reflectance. X-ray diffraction (XRD) and laboratory measurements of magnetic susceptibility, density, and natural gamma radiation (NGR) (see “Physical Properties,” p. 17) were also used to detect lithologic and sedimentologic changes. As Site 1228 is located in close proximity (within 100 m) of Leg 112 Site 680, the age framework presented in this chapter follows the chronostratigraphic observations of the Leg 112 Shipboard Scientific Party (1988b).

Description of Lithostratigraphic Units

Unit I

Interval: 201-1228A-1H-1 through 7H-5
Depth: 0–56.7 mbsf
Age: Pleistocene–Holocene

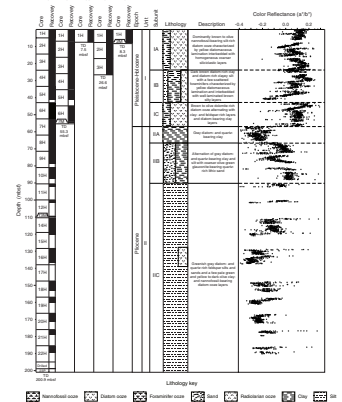
Lithostratigraphic Unit I is characterized by alternating predominantly biogenic sediments (mostly laminated diatom ooze) and silt- and clay-sized predominantly siliciclastic sediments. These alternations presumably reflect shifts in the relative dominance of the two main sources for sediments at the Peruvian continental margin: hemipelagic upwelling-derived diatomaceous oozes and reworked terrigenous clay, silt, and sand. The further subdivision of this unit into three subunits is based on smaller-scale lithologic and compositional changes and variations of other parameters including color reflectance and magnetic susceptibility (Fig. F1).

Subunit IA

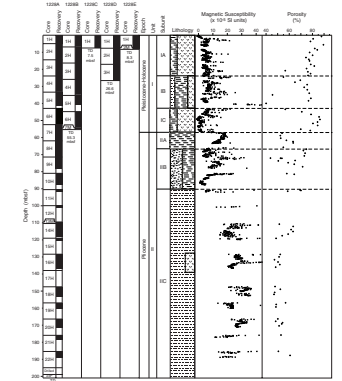
Interval: 201-1228A-1H-1 through 3H-CC
Depth: 0–24.0 mbsf

The uppermost 3 m of this unit is dominated by dark olive, weakly laminated nannofossil- and diatom-bearing silt. The base of this interval is marked by a sedimentary layer of increased terrigenous (quartz and lithic fragments) and glauconitic components, which correlates with a small peak in magnetic susceptibility (Fig. F2). A few centimeter-thick light gray volcanic ash layers are present in Sections 201-1228A-1H-1 and 1H-2 (Fig. F3A). Section 201-1228B-1H-2 contains a pink F-phosphate nodule (XRD Sample 201-1228A-1H-2, 121–122 cm; friable phos-

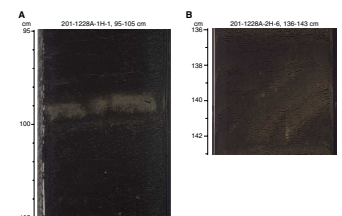
F1. Lithostratigraphic summary, p. 30.



F2. Lithostratigraphy vs. magnetic susceptibility and porosity, p. 31.



F3. Site 1228 features, p. 32.



phate, according to Leg 112 classification; Shipboard Scientific Party, 1988b).

Below 3 mbsf, the sediment grades into a greener and more strongly laminated nannofossil-bearing silt-rich diatom ooze. Several fish remains including vertebrae are present through Core 201-1228A-1H. The lamination is caused by an alternation of pale green to yellow and darker layers. These layers range in thickness from a few millimeters to a few centimeters. The lighter-colored laminae are rich in diatom frustules. Although most laminae show horizontal orientation, cross-, low-, and high-angle laminations were also observed (e.g., in Sections 201-1228A-2H-7 and 2H-6). In Section 201-1228A-2H-6 between 142 and 146 cm, laminae are present at a very high angle and are probably the result of rotational slumping (Fig. F3B).

Below ~5 mbsf, the dominant laminated diatom oozes alternate with darker, more homogeneous and siliciclastic-rich sediments that are similar to the sediments of the uppermost 3 m. Pale gray ash layers containing rare opaque clasts and abundant clay are also present throughout this subunit. In particular, volcanogenic material was observed in Cores 201-1228A-1H and 3H, where three ash layers varying in thickness from 4 to 6 cm show graded bedding and sharp basal contacts, indicating a redistribution of terrigenous and volcanic material on the seafloor. Small cream or pink nodules of F-phosphate were observed throughout the unit and are particularly abundant in Core 201-1228A-3H.

Subunit IB

Interval: 201-1228A-4H-1 through 5H-CC
Depth: 24.0–42.9 mbsf

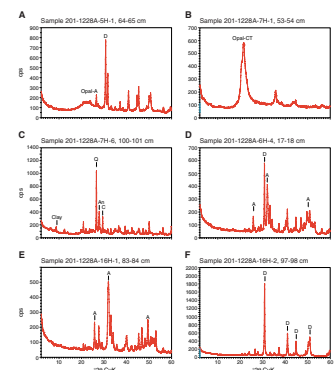
This subunit is characterized by an increase in terrigenous components, which include both clay and silt fractions. The boundary between Subunits IA and IB is also highlighted by a positive excursion in magnetic susceptibility (Fig. F2) (see also “Physical Properties,” p. 17).

The dominant lithology is dark brown to black diatom-rich clay and diatom-rich clayey silt with a few scattered foraminifers. Yellow diatomaceous laminae are composed of opal-A and dolomite (Fig. F4A) (see also “Mineralogy,” p. 10). Clay layers are poorly laminated and are interbedded with brown to green well-laminated silt layers composed of calcite, quartz, feldspar, and variable amounts of dolomite (XRD Sample 201-1228A-4H-5, 125–126 cm). Several of the silt layers show graded bedding and erosive basal contacts. At Section 201-1228A-4H-5, 62 cm, a carbonate-cemented layer (presumably dolomite) is present within a lighter-colored interval. Pyritized radiolarians and foraminifers are common. Three volcanic ash layers are present in Section 201-1228A-4H-6. In Core 201-1228A-5H, several centimeter-thick silty sand layers with sand-sized foraminifers alternate with dark brown to yellowish brown clay-rich diatom ooze layers. Normal grading, erosional contacts, bioturbated intervals, and sigmoidal fluid escape structures (particularly abundant in Section 201-1228A-5H-4) are common sedimentary features of these silty sand layers.

Subunit IC

Interval 201-1228A-6H-1 through 7H-5
Depth: 42.9–56.7 mbsf

F4. X-ray diffractograms, p. 36.



Subunit IC is composed of several lithologies. The dominant lithology is a brown to olive dolomite-bearing diatom ooze that shows varying degrees of lamination. The diatom ooze alternates with light brown clay-, quartz-, and feldspar-rich silt layers and diatom-bearing clay layers. Two ash layers with both parallel and cross lamination were observed at Sections 201-1228A-6H-4, 60 cm (Fig. F3C), and 6H-6, 60 cm. Yellow diatom-rich laminae are common, and several pink phosphate nodules were observed throughout the subunit (e.g., XRD Sample 201-1228A-6H-6, 14–15 cm). Fluorapatite is the main component of black, hard phosphate concretions (e.g., XRD Samples 201-1228A-6H-4, 17–18 cm; 6H-4, 137–138; and 6H-6, 14–15 cm) (Fig. F3D) (D-phosphates, according to Shipboard Scientific Party, 1988b), some of which also contain dolomite (Fig. F4D) (see also “*Mineralogy*,” p. 10). In interval 201-1228A-6H-2, 70–100 cm, and at Section 7H-2, 70 cm, two dolomite layers are present (Fig. F3E). A black vitreous opal-CT porcelanite lens was found at 52.9 mbsf in Hole 1228A (XRD Sample 201-1228A-7H-1, 53–54 cm; Fig. F4B) (see also “*Mineralogy*,” p. 10). In Section 201-1228A-7H-4, a black phosphatic layer, probably a hardground, has a basal erosional surface indicative of a hiatus at this depth.

Unit II

Interval: 201-1228A-7H-3 through 22H-CC
Depth: 56.7–195.0 mbsf
Age: Pliocene

The top of Unit II corresponds to the end of a sedimentary regime in which sedimentation was strongly dominated by the terrigenous input of clay, silt, and sand. Hemipelagic biogenic input was only secondary. The top of Unit II at 56.7 mbsf coincides with a shift of color reflectance, a sharp peak and an overall increase of magnetic susceptibility, and a decrease of porosity (Figs. F1, F2). Three subunits were recognized in Unit II. These subunits differ mainly in the proportions of terrigenous and biogenic components.

Subunit IIA

Interval: 201-1228A-7H-3 through 8H-3
Depth: 56.7–66.4 mbsf

The main lithology of Subunit IIA is gray diatom- and quartz-bearing clay (XRD Sample 201-1228A-7H-6, 100–101 cm; Fig. F4C). This portion of the sedimentary record is mostly homogeneous and grades into green laminated diatom- and quartz-bearing clay and silt toward the base of the subunit. A sharp peak in magnetic susceptibility indicates a higher concentration of magnetic minerals at this level (Fig. F2). The upper boundary of this subunit is well defined by prominent variation of color reflectance (Fig. F1).

Subunit IIB

Interval: 201-1228A-8H-3 through 10H-CC
Depth: 66.4–90.0 mbsf

Subunit IIB is characterized by alternations of gray diatom- and quartz-bearing clay and silt with coarser green-olive glauconite-bearing quartz-rich lithic sand. Sediments dominated by biogenic components such as diatoms and nannofossils are rare and are mostly present in clay-

rich layers in the uppermost part of the subunit. Cross lamination and erosional contacts at the base of coarser-grained layers are common features. Scattered greenish laminated layers of diatom-rich silt, clay, and volcanic glass shards are also common in this subunit (Fig. F3F, F3G).

Drilling disturbance strongly affected this portion of the cored interval. The top of most cores is marked by as much as 40 cm of pebbles and/or angular clasts of different sizes and lithologies (including dolostones and phosphates as well as well-rounded rock pebbles of terrigenous origin). These core-top layers probably originated from the collapse of higher stratigraphic levels within the hole. Drilling disturbance is also suggested by the homogenized and “soupy” appearance of many of the sections recovered from this interval.

Subunit IIC

Interval: 201-1228A-11H-1 through 22H-3

Depth: 90.0–195.0 mbsf

Cores retrieved from Subunit IIC were commonly poorly preserved and soupy. For this reason, detailed lithologic and sedimentologic observation could only be performed in a few cores.

The main lithology of this subunit consists of greenish gray diatom- and quartz-rich feldspar silt and sand. Pale green and yellow to dark olive clay- and nannofossil-bearing diatom ooze with few scattered diatom laminae, pink F-phosphate, and dolomite nodules are also present in this subunit (e.g., Samples 201-1228A-16H-1, 83–84 cm, and 16H-2, 97–98 cm; Fig. F4E) (see also “*Mineralogy*,” p. 10). Between ~110 and 120 mbsf (Core 201-1228A-13H), sediments show higher silt and clay content.

Mineralogy

X-ray diffraction analyses were performed on 15 samples from Site 1228. The purpose of mineralogic sampling was to determine both small-scale compositional changes (e.g., differences between laminae of different colors) and the mineralogy of authigenic nodules. Overall, the mineralogic composition of the samples collected from Unit I reflects the high biogenic content of these upwelling-related hemipelagic sediments. Lamination, which is a prominent characteristic of this unit, is caused by episodic and possibly cyclic deposition of very pure opal-A diatomaceous ooze layers (Fig. F4A). Smear slide and XRD analyses also show that some of these diatomaceous laminae contain scattered dolomite rhombohedra (Fig. F4A). A high concentration of biogenic silica is perhaps the cause for the shallow depth of the opal-A to opal-CT phase change expressed by the presence of a black vitreous opal-CT porcelainite lens at 53 mbsf (Fig. F4B). Deposition of Unit II was mainly influenced by terrigenous input, especially in Subunit IIA, which consists of very fine grained gray silt composed of quartz, feldspar, and clay minerals (Fig. F4C).

At Site 1228, two kinds of authigenic minerals were observed, apatite and dolomite. Both minerals are present throughout the recovered interval but are concentrated in Subunits IC and IIB. Apatite is either present as small (a few millimeters) white to pink friable nodules (F-phosphate) (Fig. F4E) or as dark, hard nodules that often replace burrows and may have been formed during depositional hiatuses (D-phosphate) (Fig. F4D). Dolomite nodules are usually white to yellow and, in

a few cases, green. The XRD spectrum for a green dolomite nodule in Subunit IIC is shown in Figure F4F.

Summary

The upper 56.7 mbsf of the sedimentary sequence at Site 1228 is characterized by predominantly biogenic hemipelagic sediments (Unit I), formed in an upwelling environment analogous to today's setting along the Peruvian continental margin. In contrast, the lower part of the sediment column is dominated by fine-grained siliciclastic components that indicate the local sedimentary environment was influenced by terrigenous input and, thus, was different from its modern condition (Unit II). Lithostratigraphic Unit I consists of alternating intervals of predominantly biogenic (mostly laminated diatom ooze) and silt- and clay-sized predominantly siliciclastic sediments. Subunit IA grades from dark olive, weakly laminated nannofossil- and diatom-bearing silty sediments into a greener and more strongly laminated nannofossil-bearing silt-rich diatom ooze. Deeper in this subunit, diatom ooze alternates with darker, more homogeneous and again siliciclastic-rich sediments. Pale gray layers of volcanogenic origin and siliciclastic-rich sediments showing graded bedding and erosional basal contacts are present throughout the subunit, indicating a redistribution of terrigenous and volcanic material by bottom currents. The dominant lithology of Subunit IB is dark brown to black diatom-rich clay and diatom-rich clayey silt. Yellow diatomaceous laminae composed of opal-A and dolomite are frequently present. Clayey intervals are poorly laminated and alternate with brown to green well-laminated silt layers composed of calcite, quartz, feldspar, and variable amounts of dolomite. Diatom ooze of Subunit IC alternates with light brown clay- and feldspar-rich silt layers and diatom-bearing clay layers. Ash layers, diatom-rich laminae, and pink phosphate nodules are common throughout the subunit. Fluorapatite is the main component of black, hard phosphate concretions. A black phosphatic layer with an erosional base probably reflects the formation of a hiatus and marks the base of Unit I. The onset of Unit II corresponds to the beginning of a sedimentary regime strongly dominated by the terrigenous input of clay, silt, and sand. Subunit IIA is characterized by mostly homogeneous gray diatom- and quartz-bearing clay that grades into green laminated diatom- and quartz-bearing clay and silt toward the base of the interval. Subunit IIB shows an alternation of gray diatom- and quartz-bearing clay and silt with coarser olive-green glauconite-bearing quartz-rich lithic sand. Cross lamination and erosional contacts are common features of this subunit. Biogenic components such as diatoms and nannofossils are rare and are mostly present in clay-rich layers in the uppermost part of the subunit. Drilling disturbance strongly affected this portion of the sedimentary record. The main lithology of Subunit IIC consists of greenish gray diatom- and quartz-rich feldspar silt and sand; however, drilling disturbance and poor recovery precluded a more detailed description of the lowermost part of the cores from Site 1228.

Diagenetic processes in Site 1228 sediments are dominated by the formation of authigenic dolomite and phosphate nodules and concretions. Dolomite was especially common throughout the recovered interval, particularly in Subunits IC and IIB. Phosphate is present both as pink friable nodules (F-phosphate) and as dark, hard concretions (D-phosphate), which often replace burrows and form hardgrounds. Phosphate composition is usually fluorapatite, but smaller amounts of car-

bonate fluorapatite and dolomite were also detected. The presence of porcelanite at relatively shallow depth (~53 mbsf) and the presence of authigenic phosphate and dolomite minerals throughout the sediment column emphasize the wide range of diagenetic processes at Site 1228.

BIOGEOCHEMISTRY

At Site 1228, 49 interstitial water (IW) samples were collected from Hole 1228A to obtain high-resolution chemical profiles over 189 m, generally at three samples per core unless recovery was limited. Two samples were collected from Core 201-1228B-6H to cover an interval missed in Hole 1228A. Ten samples were collected from Hole 1228C and eleven samples from Hole 1228E to gain additional resolution over the uppermost 6.35 m.

Overall, microbially mediated reactions and the diffusion of brine from depth dominate interstitial water trends, with electron acceptors being supplied from both the top and bottom of the section. Local extremes in IW profiles indicate nonsteady-state conditions over certain depth intervals induced by changes in boundary conditions or differences in sediment composition. Microbial activity is not high enough to completely deplete IW sulfate.

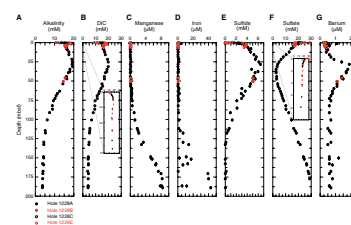
Interstitial Water

Alkalinity and DIC exhibit similar profiles downhole (Fig. F5A, F5B). Alkalinity ranges from 10.8 mM in the uppermost sample to 18.8 mM at 1.5 mbsf (Table T2). It then decreases to 15.6 mM at 4.5 mbsf and increases to a second maximum of 19.4 mM at 25.3 mbsf. Alkalinity decreases toward the base of the hole, where concentrations are <4 mM. DIC concentrations range from a low of 9 mM in the upper few centimeters below seafloor to 18.7 mM at 2 mbsf. They then decrease to 15.5 mM at 4.3 mbsf and increase to 19.8 mM at 25.25 mbsf. Concentrations below this second maximum decrease toward the bottom of the hole, where concentrations are <4.1 mM. The presence of two maxima in DIC and alkalinity probably reflects nonsteady-state conditions resulting from changes in bottom-water or sediment composition (i.e., see contents of TOC, Table T7, p. 97; Fig. F6B, p. 54, both in the “Site 1230” chapter). The convex-upward curvatures at the bottom suggests net removal.

There are two distinct intervals in the dissolved manganese profile (Fig. F5C). From the sediment/water interface to 56.75 mbsf, concentrations of dissolved manganese are low (<0.2 μM). Below this depth, concentrations steadily rise to 8.4 μM at 189 mbsf. Thus, the dissolved manganese profile at Site 1228 lacks the prominent maximum observed at the deep-sea locations, Sites 1225 and 1226, and the scatter observed at Site 1227.

Similar to Site 1227, concentrations of dissolved Fe (Fig. F5D) remain <1.5 μM to a depth of ~112 mbsf. Below this depth, concentrations rise erratically to 44 μM. The dissolved iron profile has an inverse relationship to total dissolved sulfide ($\Sigma\text{H}_2\text{S} = \text{H}_2\text{S} + \text{HS}^-$) (Fig. F5E); the dissolved iron is low where dissolved sulfide is high and vice versa. Most of labile iron hosted in the upper sediment column probably resides as iron sulfides. Dissolution of these phases may occur in the deeper part of the core where total sulfide drops to low concentrations and dissolved oxygen remains undetectable.

F5. Dissolved species in IW, p. 37.



T2. Dissolved species in IW, p. 62.

The dissolved sulfate profile exhibits features that clearly indicate nonsteady-state conditions and distinct intervals of relatively high rates of microbial respiration (Fig. F5F). Between the sediment/water interface and 1 mbsf there is a steep drop in sulfate concentrations from a seawater value (29 mM) to 17 mM by 1.4 mbsf. The gradient then decreases and is nearly linear until 25 mbsf. Below this depth, the profile reaches a minimum of 2.5 mM at 37.8 mbsf. From 53.8 mbsf to the bottom of the hole, concentrations of dissolved sulfate increase linearly, reaching 31 mM at 189 mbsf. The increase in concentrations in the deeper part of the hole is due to the diffusion of sulfate from a deeply buried brine.

Dissolved sulfide is 0.2 mM between 0 and 12 centimeters below seafloor (Fig. F5E). Sulfide concentrations rapidly increase to 3.8 mM at 1 mbsf. At greater depths, sulfide concentrations continue to increase with increasing depth but with a substantially smaller gradient. The break in the sulfide profile at 1 mbsf mirrors the sulfate profile and coincides with a peak in the concentration of DIC. A peak sulfide concentration of 6.4 mM is present at 28.2 mbsf, approximately the depth of the second maximum in DIC. Below 28.2 mbsf, sulfide concentrations linearly decrease to 0.006 mM at a depth of 132 mbsf. Concentrations of dissolved sulfide remain low (<0.006 mM) through the rest of the drilled section except for one sample at 189 mbsf (0.02 mM).

Interstitial water barium concentrations range between 0.2 and 2.1 μM (Fig. F5G). These values exceed those at deep-sea Sites 1225 and 1226 but are much lower than those at Sites 1227 and 1229. As at all other locations, dissolved barium displays an inverse relationship with sulfate. The lowest barium concentration is present at the sediment/water interface and at the bottom of the hole, where sulfate concentrations are high. The highest barium concentration is present between 28 and 38 mbsf, where sulfate concentrations reach a minimum. The solubility of barite and the distribution of sulfate probably determine the overall barium profile.

Methane was detected in all samples at Site 1228 (Table T3; Fig. F5H). Using the standard ODP headspace technique, methane concentrations are close to 2 μM at the sediment/water interface and increase to a maximum of 8.4 μM at 35-mbsf sulfate minimum. Below this depth, methane concentrations decrease to ~100 mbsf, where they stabilize at ~2 μM . Consistent with observations from the previous sites, the 1-day extraction procedure resulted in higher methane yields than the 20-min extraction used for safety purposes (Table T3). Maximum methane concentration at Site 1228 is several orders of magnitude lower than that at Site 1227. The lower methane abundances at Site 1228 are consistent with the fact that dissolved sulfate is never completely depleted in the interstitial waters at Site 1228.

Ethane was found in very low concentrations at Site 1228. Its highest values coincide with relatively high methane concentrations and low sulfate concentrations. Similar to methane, the vertical distribution of ethane in the sediment column is consistent with its biological production and consumption.

Acetate and formate concentrations were determined in 19 IW samples from Hole 1228A (Table T2; Fig. F5I). Concentrations are in the same range as those at Site 1226 (see “Biogeochemistry,” p. 13, in the “Site 1226” chapter). Acetate concentrations are between 0.5 and 2.5 μM , and formate concentrations are between 0.3 and 2 μM . As at previous sites, the highest concentrations of both compounds are present deeper in the section.

T3. Methane in headspace, p. 64.

Ammonium concentrations are $<100\ \mu\text{M}$ near the sediment/water interface and increase to a local maximum of $2500\ \mu\text{M}$ by 1.4 mbsf (Fig. F5J). This local maximum coincides with the local minimum in the sulfate profile and local maxima in the alkalinity and DIC profiles (Fig. F5A, F5B). Between 2 and 4.5 mbsf, ammonium concentrations decrease to $2000\ \mu\text{M}$. Below 4.5 mbsf, ammonium concentrations steadily increase to $4000\ \mu\text{M}$ at 34.8 mbsf. After a change in the slope of the profile, ammonium concentrations gradually increase with depth to $\sim 5000\ \mu\text{M}$ at 186.8 mbsf.

Dissolved phosphate concentrations were determined on samples previously analyzed for alkalinity, from which interfering hydrogen sulfide had been removed by acidification and degassing (as detailed in “**Biogeochemistry**,” p. 13, in the “Site 1227” chapter). Phosphate concentrations rise sharply below the sediment/water interface, from $4\ \mu\text{M}$ in bottom seawater to $47.7\ \mu\text{M}$ at 0.12 mbsf (Fig. F5K). Concentrations of phosphate remain between ~ 42 and $49\ \mu\text{M}$ in the upper 1.3 m of the sediment column but sharply decrease to $4.5\ \mu\text{M}$ by 4.6 mbsf. The decrease most likely results from the onset of authigenic apatite precipitation. There is a local increase to $9.7\ \mu\text{M}$ at ~ 8 mbsf. This is followed by a gradual decrease to $<3\ \mu\text{M}$ at ~ 45 mbsf. Except for one sample at 72.75 mbsf, values range between 1.5 and $4\ \mu\text{M}$ in the lowermost 124 m of the drilled section.

Dissolved silica concentrations are $860\ \mu\text{M}$ by 0.2 mbsf and reach $1017\ \mu\text{M}$ by 6.3 mbsf (Fig. F5L). Silica then ranges from ~ 900 to $1100\ \mu\text{M}$ between 6.3 and 186.8 mbsf. The profile is most likely controlled by biogenic silica solubility.

Chloride increases monotonically downhole to a concentration at 189 mbsf that is nearly twice that of seawater (Fig. F5M). This trend results from the diffusion of chloride from a deeply buried brine. The profile has two linear segments, with an apparent change in slope at 56.7 mbsf, the boundary between lithostratigraphic Units I and II (see “**Lithostratigraphy**,” p. 7). The slope change may reflect a difference in diffusivity between the two units. A change in diffusivity is consistent with the measured variation in formation factor and porosity between the two units (see “**Physical Properties**,” p. 17). The linear profiles constrain vertical advection velocities to $<0.002\ \text{cm/yr}$.

Dissolved strontium concentrations increase from $90\ \mu\text{M}$ near the seafloor to $\sim 400\ \mu\text{M}$ at 189 mbsf (Fig. F5N), a lower overall gradient than at Site 1227. As at Site 1227, however, the gradient changes downhole. The strontium gradient decreases with depth from $2.1\ \mu\text{M/m}$ over the upper 40 mbsf to $1.0\ \mu\text{M/m}$ over the lowermost 40 m of the drilled section.

Dissolved lithium concentrations increase from $27\ \mu\text{M}$ near the seafloor to $\sim 400\ \mu\text{M}$ at the bottom of the hole (Fig. F5O). As with strontium, the lithium gradient is lower at Site 1228 than Site 1227. The downhole enrichments in strontium and lithium relative to chloride are, respectively, $\sim 25\%$ – 35% smaller at Site 1228 than at Site 1227. These differences suggest that the brines at the two sites have different compositions.

Hydrogen incubations were conducted on 14 samples from Hole 1228A and 4 samples from Hole 1228E. All incubations were at 11°C (Table T4). Calculated interstitial fluid concentrations of the incubated sediments are shown in Figure F5P and fall in a narrow range, similar to those observed at Site 1227. All concentrations were between 0.16 and 0.95 nM, with most samples between ~ 0.2 and ~ 0.4 nM.

T4. Hydrogen concentrations, p. 66.

Sediments

Concentrations of TOC were determined by Rock-Eval Pyrolysis (Table T7, p. 97; Fig. F6B, p. 54, both in the “Site 1230” chapter). TOC values at Site 1228 are strikingly variable and range from >10% to >0.5%. All values >3% are restricted to the upper 45 mbsf.

MICROBIOLOGY

Microbiological sampling of Site 1228 covered the sulfate-reducing zone near the surface, the sulfate minimum between 30 and 80 mbsf, and the deeper brine interval layer at depths between 80 and 193 mbsf. One or two sections of each core were routinely sampled for deoxyribonucleic acid (DNA) analysis, measurements of sulfate reduction rates, hydrogen concentrations and turnover, methanogenesis rates, acetate turnover, thymidine incorporation, bacterial lipid biomarkers, adenosine triphosphate, fluorescent *in situ* hybridization (FISH), and iron/manganese/sulfur solid phases (Fig. F6). An additional abridged sampling program for iron/manganese/sulfur solid phases and sulfate reduction rates was performed at higher resolution throughout the upper part of the core (Cores 201-1228A-2H through 7H). Core 201-1228A-6H (43–52 mbsf) was not sampled because the core barrel shattered, resulting in a severely disturbed core. It was substituted with a core section from the same depth interval of Hole 1228B (Section 201-1228B-6H-3, 49.3–50.8 mbsf). A full suite of microbiological samples was taken on this section (Fig. F7). Every core that could be obtained from the deeper layers of the sediment column was sampled to analyze the prokaryote communities and activities in the deep sulfate-rich brine layer below the sulfate minimum (Sections 201-1228A-14H-3 through 22H-2) (Fig. F6). Sampling of four sections of the mudline core from Hole 1228E (Sections 201-1228E-1H-1, 1H-2, 1H-3, and 1H-4) aimed at fine resolution of the highly compressed chemical and prokaryote gradients at the top of the sediment column in order to provide good end-member data for the microbiological and geochemical analyses in deep sediment layers (Fig. F8).

Total Prokaryote Enumeration

Samples of 1-cm³ plugs for prokaryotic cell enumeration were taken on the catwalk from a total of 20 depths between the sediment surface and 187.4 mbsf at this site. These were between 7.9 and 187.4 mbsf in Hole 1228A (14 samples), at 48.9 mbsf in Hole 1228B, and between the sediment surface and 5.7 mbsf in Hole 1228E (5 samples). Additionally, 2-mL samples of 25% slurry were taken from the four slurries prepared in the laboratory. These samples will be processed as part of shore-based activities, and no data are presented here.

Contamination Tests

While drilling cores for microbiology, the potential for contamination with bacteria from the surface is highly critical. Contamination tests were continuously conducted using solutes (PFT) or bacterial-sized particles (fluorescent microspheres) to check for the potential intrusion of drill water from the periphery toward the center of cores and thus to confirm the suitability of the core material for microbiological research.

F6. Subsampling for MBIO sections, Hole 1228A, p. 40.

F7. Subsampling for MBIO sections, Hole 1228B, p. 41.

F8. Subsampling for MBIO sections, Hole 1228E, p. 42.

We used the chemical and particle tracer techniques described in ODP *Technical Note 28* (Smith et al., 2000). Furthermore, the freshly collected cores were visually examined for possible cracks and other signs of disturbance by observation through the transparent core liner. Core sections observed to be disturbed before or after subsampling were not analyzed further. Such disturbance phenomena are critical to the integrity of the core material and therefore also to its usefulness for microbiological studies.

Perfluorocarbon Tracer

The PFT was injected continuously into the drilling fluid during drilling of Holes 1228A and 1228E (see “[Perfluorocarbon Tracer Contamination Tests](#),” p. 26, in “Procedures and Protocols” in “Microbiology” in the “Explanatory Notes” chapter). PFT sampling focused on microbiology cores and especially on sections that were used for slurry preparation and cultivations.

To compare the PFT concentration in the center of a core to the PFT concentration at the periphery of the same core, two 5-cm³ samples were taken from the center of a core end and another 5-cm³ sample was taken at the core periphery, adjacent to the core liner. Whenever possible, the samples were taken directly on the catwalk because the PFT content of catwalk air was usually near zero.

Low levels of potential seawater contamination (Table T5) were found for the center portions of all tested cores of Holes 1228A and 1228E, not higher than 0.11 μL seawater/g sediment (average = 0.03 μL seawater/g sediment), with two of nine below detection (<0.01 μL seawater/g sediment). The outer portions of all tested cores had a significantly higher level of PFT tracer and potential seawater contamination (average = 0.17 μL seawater/g sediment). In all cases, the PFT content and potential seawater contamination levels were higher at the periphery of the core than in the center. Cores 201-1228A-15H and 22H were particularly wet cores and were, therefore, subsampled to investigate whether or not the visible water was contaminating seawater drilling fluid. In the case of Core 201-1228A-15H, the PFT concentration was measured in two different subcores. Both of these subcores indicated concentrations of PFT lower than would be expected for samples contaminated with drilling fluid. In the case of Core 201-1228A-22H, two samples were taken, one in a dry and one in a wet region of the microbiology section. Both showed similar low concentrations of PFT, representing 0.1 μL potential seawater contamination/g sediment.

Of the four master slurry samples taken from Site 1228 (Table T6), three showed small but detectable concentrations of PFT. These small concentrations represent 0.03 μL potential seawater contamination/mL slurry. Assuming 5×10^8 bacterial cells/L surface seawater, each 0.1 μL seawater contamination may represent as many as 50 contaminating cells if the sediment is porous enough to allow cells to travel with the PFT.

Particulate Tracer

Fluorescent microspheres (beads) were deployed on all four cores from which slurries were made at this site. The mode of deployment for bead packs was altered from that of the previous site, as a consequence of some previous deployment failures. During previous deployments, Whirl-Pak bags (4 oz) containing 20 mL of microsphere suspension

T5. Seawater contamination based on PFT, p. 67.

T6. Contamination of slurries based on PFT, p. 68.

were attached to one side of a spacer within the core catcher. However, at the previous site, some sediment cores were soft enough to slide past the attached bag without bursting it, so the microspheres were not released. As a modification, the bag was filled with twice the volume (40 mL), while keeping the number of microspheres constant, and heat-sealed at the ends. The bag was then placed across the spacer unit and tied in on both sides, with the heat seals outside of the spacer lumen. Sediment cores were consequently forced to burst through the bead bag when a core was taken. No failures were reported at this site.

For each slurry two subsamples were processed: (1) a sample of the slurry to check contamination and (2) a scraping from the outer surface of the core to confirm deployment of microspheres. Microsphere deployment was confirmed from the outer core scrapings in all four cores that were sampled for slurry preparation (Table T7). In two slurry samples, microspheres were detected (1/sample in each case). Further microscopic searching of the membrane failed to detect any additional microspheres. These single microspheres represent potential contaminations of 42 to 56 prokaryotic cells/mL sediment. It is believed that these data represent filter handling and processing effects rather than true contamination (see “**Fluorescent Microparticle Tracer,**” p. 27, in “Procedures and Protocols” in “Microbiology” in the “Explanatory Notes” chapter).

Cultivations

Slurries for cultivation were usually prepared by subcoring with two 60-mL syringes from the center of two freshly broken surfaces (after precutting the core liner with the ODP cutter). Bending the ends of the whole-round core upward allowed released particles to drop down into a bin. This technique provided untouched (although not always smooth) surfaces that were immediately sampled. All MPN dilutions and enrichments inoculated using samples from Site 1228 are listed in Table T8.

FISH-SIMS

¹³C substrate incubations were initiated for postcruise analysis by FISH-secondary ion mass spectrometry (SIMS) using material from Cores 201-1228A-2H, 5H, and 14H. In each case, 10 mL of the master slurry was injected into a bottle. The ¹³C substrates used were methane, acetate, and glucose. For Cores 201-1228A-2H and 5H, one of each bottle was inoculated. For Core 201-1228A-14H, two bottles with each substrate were inoculated.

PHYSICAL PROPERTIES

At Site 1228 we collected a full range of physical property data from all available cores in Hole 1228A, which extended from the seafloor to a depth of 200.9 mbsf. All cores except for two (Core 201-1228A-13M and the deepest one, Core 23P) were taken by APC. Four additional holes were drilled at Site 1228 to address high-resolution objectives and spot-coring needs. Each core was run through the multisensor track (MST), with Hole 1228E at high resolution and Holes 1228B, 1228C, and 1228D at standard resolution, but no discrete moisture and density (MAD) samples were collected from these subsequent holes.

T7. Contamination of slurries based on fluorescent beads, p. 69.

T8. Media inoculated with material from Site 1228, p. 70.

The physical property data from these cores are described below and compared with those from Site 680 (Shipboard Scientific Party, 1988b). The stratigraphic record was extended marginally from Leg 112, Hole 680B (195.5 mbsf) to 200.9 mbsf in Hole 1228A, with much improved recovery below 92.0 mbsf because of APC coring. Dolomitic hard-ground and gravels resulted in caving and out-of-sequence responses in the downhole trend of physical logs, but in most cases these are located at or near the ends of cores. Nonetheless, we were able to acquire a more complete interpretable record at a higher spatial resolution than Leg 112 scientists.

Whole-round cores were degassed for up to 2 hr on the catwalk when necessary for safety, were equilibrated to laboratory temperature (2–4 hr), and then each available section was run on the MST. The standard measurements were magnetic susceptibility (spacing = 5 cm, data acquisition scheme [DAQ] = 2×1 s), gamma ray attenuation (GRA) density (spacing = 10 cm, count time = 5 s), *P*-wave velocity (spacing = 10 cm, DAQ = 10), and NGR (spacing = 30 cm, count time = 15 s). Thermal conductivity measurements were made on the third section of each whole-round core in Hole 1228A, where possible. Some sections were removed from the catwalk for microbiology and interstitial water sampling. Physical properties were measured on these sections only if intact parts remained following the sampling. This limited the continuity and, hence, spatial resolution of the physical property record below ~90 mbsf.

MAD, *P*-wave velocity from the digital velocimeter, and resistance data (translated to formation factor, as detailed in “**Formation Factor,**” p. 47, in “Physical Properties” in the “Explanatory Notes” chapter) were collected regularly only from Hole 1228A. MAD samples were taken at one per section and at higher resolution in sections with many voids or lithologic transitions. MAD samples were co-located with the methane headspace extractions, where possible, to facilitate the volumetric analysis of methane concentrations. Spot sampling for MAD was also carried out in Hole 1228D, in order to confirm measurements from Hole 1228A. Even though core recovery decreased significantly below ~90 mbsf, the supplementary data are sufficient to allow characterization of the physical parameters of each lithostratigraphic unit and to be confident of the correspondence of our data to those from Site 680.

Instrumentation, measurement principles, and data transformations are further discussed in “**Physical Properties,**” p. 41, in the “Explanatory Notes” chapter.

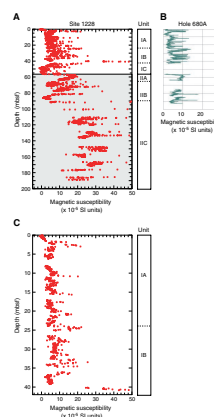
Infrared Scanner

The infrared scanner was not employed at this site, due to expected rapid recovery.

Magnetic Susceptibility

Low-field volume magnetic susceptibility was measured on the MST using the Bartington loop sensor as described in “**Magnetic Susceptibility,**” p. 44, in “MST Measurements” in “Physical Properties” in the “Explanatory Notes” chapter. The magnetic susceptibility record is shown in Figure F9. We have divided the cored interval into five susceptibility “zones” based on the downhole record. These zones compare readily with the lithostratigraphic subdivisions (see “**Description of Lithostratigraphic Units,**” p. 7, in “Lithostratigraphy”):

F9. Comparison of magnetic susceptibility, p. 43.



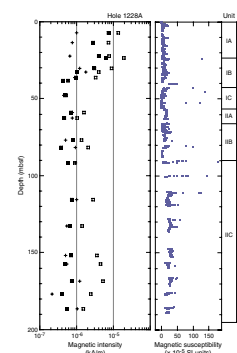
1. From 0 to 43 mbsf (Subunits IA and IB), the signal mostly varies between 2.5×10^{-5} and 10×10^{-5} SI units. Within this interval there are several peaks of up to 25×10^{-5} SI units (including at 2.5, 11, 21, and 35 mbsf). This record corresponds closely to the Site 680 data set (Fig. F9B) (Merrill et al., 1990). The peak at 2.5 mbsf emanates from a glauconite-bearing quartz-rich lithic silt. There is a significant increase in susceptibility at 24 mbsf, corresponding to the Subunit IA/IB boundary, which is best seen in the high-resolution data set (Fig. F9C). The remainder of the peaks in this interval are located near core or section ends and appear to be artifacts that do not correspond to obvious lithologic features.
2. Across the interval from 43 to 57 mbsf (lithostratigraphic Subunit IC), magnetic susceptibility decreases from 10×10^{-5} to 0×10^{-5} SI units, with peaks at 43 and 47 mbsf. As with zone 1 above, the higher susceptibility values are adjacent to the end of a core, making the reliability of the signal questionable.
3. At 57 mbsf there is an abrupt increase in magnetic susceptibility from $\sim 0 \times 10^{-5}$ to $15\text{--}20 \times 10^{-5}$ SI units. The magnetic susceptibility high is located within a 5-m interval that corresponds to a lithologic change from overlying diatom oozes of Unit I to the clay- and silt-dominated lithologies of Unit II (see “[Description of Lithostratigraphic Units](#),” p. 7, in “[Lithostratigraphy](#)”). From 57 to ~ 72 mbsf, susceptibility decreases from 20×10^{-5} to 5×10^{-5} SI units.
4. There is a peak of 30×10^{-5} SI units at 72 mbsf. This peak is located at the top of Core 201-1228A-9H and is possibly a result of accumulated gravel in the bottom of the hole prior to coring the next interval, although Section 201-1228A-9H-1 contained the stratigraphically highest recorded gravel in the sequence. Below 72 mbsf, magnetic susceptibility increases from 5×10^{-5} to 20×10^{-5} SI units at 120 mbsf. Although the record is incomplete, the most significant increase in the susceptibility record is located between 90 and 110 mbsf.
5. From 120 mbsf to the base of Hole 1228A, magnetic susceptibility is consistently higher, varying between 15×10^{-5} and 35×10^{-5} SI units. Core recovery was much lower below 90 mbsf, and several narrow peaks are present adjacent to missing sections and core tops. We interpret the highest readings across this interval as drilling artifacts.

Paleomagnetism

At Site 1228 we collected 21 discrete samples for paleomagnetic measurements. The sampling frequency was two samples from each core in Cores 201-1228A-2H through 5H (6.8–42.9 mbsf) and one sample from each core below this interval to the bottom of the hole (Cores 201-1228A-6H through 22H; 42.9–194.9 mbsf). Alternating-field (AF) demagnetization of the natural remanent magnetization (NRM) was conducted up to 40 mT in 10- or 5-mT steps. Anhyseretic remanent magnetization (ARM) was measured to 40 mT in 10-mT steps with a 29- μ T direct current–biasing field. AF demagnetization of the ARM was conducted to 40 mT in 10-mT steps.

Lithostratigraphic Subunits IA through IB and the lower part of Subunit IIC (see “[Description of Lithostratigraphic Units](#),” p. 7, in “[Lithostratigraphy](#)”) exhibit higher NRM intensity (Fig. F10). Dark

F10. Magnetic intensity and susceptibility, p. 44.



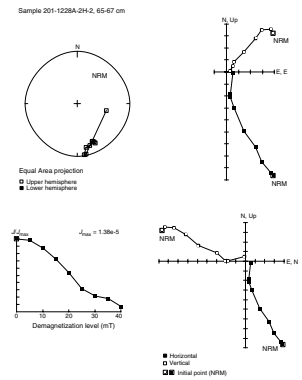
brown sand-sized foraminifer-bearing siliciclastic-rich diatom ooze (Samples 201-1228A-2H-2, 65–67 cm, and 4H-5, 32–34 cm) in lithostratigraphic Subunits IA and IB show stable magnetization (Fig. F11). Gray volcanogenic material containing silt (Sample 201-1228A-3H-7, 5–7 cm) shows stable magnetization after removing the downward drilling-induced overprint by 10-mT AF demagnetization (Fig. F12). Higher NRM intensity and susceptibility in lithostratigraphic Subunit IIC correlated with the coarse lithology, which is gray diatom and quartz-rich feldspar silt and sand. This interval has a low magnetic intensity after 20-mT AF demagnetization (Fig. F10).

Density and Porosity

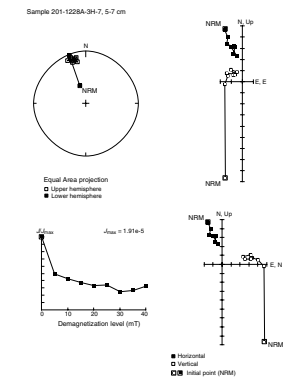
Density data were measured on the MST by the GRA densitometer (spacing = 10 cm, count time = 5 s) and calculated from split-core mass/volume measurements. Porosity was calculated from the split-core samples. The overall trend in the GRA density is increasing, from 1.2 g/cm³ at the top of Hole 1228A to ~1.7 g/cm³ at the base (Fig. F13). Moving averages of 5 m of Hole 1228A and Site 680 GRA densities illustrate consistent general trends, with both data sets highlighting the abrupt lithologic boundary at 57 mbsf (Fig. F14). The discrete sample MAD bulk densities track the MST density record very well, except for a few outliers in Unit I (Fig. F15A). The porosity decreases from ~80% at 0 mbsf to ~50% by 120 mbsf (Fig. F15C). At 90 mbsf, coincident with the Subunit IIB/IIC boundary, amplitude variations in the porosity data decrease. Below 120 mbsf, average porosity is relatively constant to the bottom of the hole. There is a strong correlation among the density, porosity, and magnetic susceptibility records, and the same five zones seen in magnetic susceptibility are apparent in both of the other records, delineated by noticeable peaks in density and lows in porosity:

1. The top 43 m, incorporating Subunits IA and IB, has a stationary downhole trend with density consistently between 1.2 and 1.5 g/cm³. The bottom of this zone is identified by a clear density peak of 2.0 g/cm³ at 42 mbsf, which corresponds to a porosity low of 35%.
2. From 43 to 57 mbsf (Subunit IC), the average MST bulk density decreases slightly from 1.3 to 1.2 g/cm³, with a similar decrease observed in the discrete sample data. We attribute this to a systematic increase in biogenic components of the sediment (grain densities fall to ~2.06 g/cm³) (Fig. F15B). Bulk density abruptly increases to ~2.0 g/cm³ at 57 mbsf, coincident with the Unit I/II boundary and a sharp porosity decrease.
3. From 57 to 72 mbsf (Subunit IIA), bulk density decreases from 1.8 to 1.4 g/cm³, with one excursion at 72 mbsf that corresponds to the stratigraphically highest gravel layer.
4. The zone from 72 to 120 mbsf has at least four cycles characterized by an upward increase in density and corresponding upward decrease in porosity, although the porosity record is more symmetrical than the density, especially in the lowermost of these cycles. Each cycle is 10–15 m thick. Core recovery greatly decreased below 90 mbsf, and gravel layers were consistently found at the top of cores, suggesting core disturbance. The wireline log density (Fig. F13) and porosity (Fig. F15C) records, however, show the same cycles, and partial records from the discrete samples support recognition of these trends.

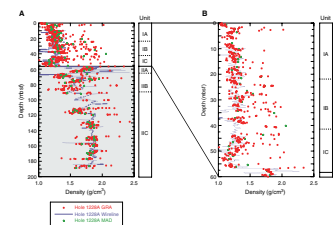
F11. Principal component analysis, 201-1228A-2H-2, 65–67 cm, p. 45.



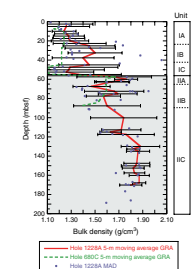
F12. Principal component analysis, 201-1228A-3H-7, 5–7 cm, p. 46.



F13. GRA and MAD density, p. 47.



F14. Comparison of GRA and MAD densities, p. 48.



- From 120 mbsf to the base of the hole, the average density is nearly constant at 1.8 g/cm³.

Grain density data from Holes 680A and 680B extend from 0 to ~90 mbsf (Shipboard Scientific Party, 1988b). Both sets of their density measurements are highly variable, and we have not included these data in our plots. The values are ~12% higher than Hole 1228A measurements shown in Figure F15B. In Hole 680B they range from 2.2 to almost 3.0 g/cm³. The poor resolution of their data shows no clear downhole pattern. A positive excursion is visible in the Hole 680A data at 60 mbsf, coincident with the one we identified in Hole 1228A, but apparently grain density lows were not detected between 45 and 50 mbsf or at ~72 mbsf.

Compressional Wave Velocity

P-wave data from the MST *P*-wave logger (PWL) were recorded (spacing = 10 cm, DAQ = 10) for all available APC cores from Holes 1228A, 1228C, and 1228D and at 2-cm spacing for Hole 1228B. The PWS3 velocimeter was used to measure *P*-wave velocities on split cores from Hole 1228A, with measurements taken at a minimum of one per section, depending on lithologic boundaries or evidence of diagenetic or other petrophysical changes. Most measurements were taken in the *x*-axis direction using the PWS3 contact probe. In intervals containing suspension-like material, most of which were silt or sand, insertion *P*-wave sensors 1 and 2 (PWS1 and PWS2), which measure along the core axis (*z*-axis) and across the core axis (*y*-axis), respectively, were used. These were used in Cores 201-1228A-16H, 19H, and 20H.

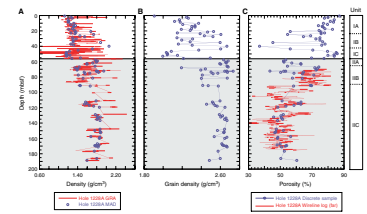
Between 0 and 40 mbsf, PWL measurements range from 1445 to 1680 m/s, whereas PWS3 velocities are within the range 1520–1625 m/s (Fig. F16). The PWS measurements were generally 30–40 m/s faster (similar to measurement differences at Site 1227). Between 40 and 90 mbsf, PWL measurements range from 1420 to 1680 m/s, whereas PWS3 velocities are bounded within 1520–1680 m/s (Fig. F16). This depth interval is characterized by more variable measurements. Below Core 201-1228A-11H (~90 mbsf), the PWL and PWS3 measurements are discontinuous but generally increase downcore from ~1550 to 1650 m/s, to a depth of ~160 mbsf.

There are several peaks in *P*-wave velocities that correspond to peaks found in other physical property measurements at 42, 57, and 72 mbsf. However, the resolution of small peaks (such as those at 2.5, 11, and 25 mbsf) is too poor to make any conclusive interpretation based on *P*-wave data alone. Below 90 mbsf, velocity peaks may be less dependable because the core liners were commonly not completely filled.

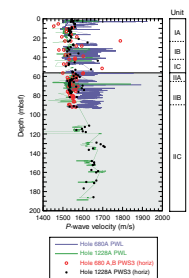
Natural Gamma Ray Emission

NGR was measured on the MST for all Site 1228 holes (spacing = 30 cm, count time = 15 s), except for Hole 1228B, which was run at a higher spatial resolution (spacing = 15 cm, count time = 15 s). In addition, natural gamma radiation was recorded with the NGR sonde during the triple combo wireline logging run. Both data sets are shown in Figure F17. There is reasonable correspondence between the trends in the wireline and MST NGR traces above 70 mbsf, where the wireline sonde was within the drill pipe and the record is attenuated. The most prominent peaks (~17 American Petroleum Institute gamma ray units [gAPI] at 3 mbsf and 24 gAPI at 57 mbsf) match those on the MST

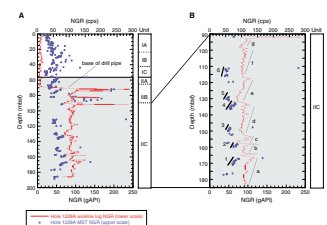
F15. Density and porosity, p. 49.



F16. *P*-wave velocity profiles, p. 50.



F17. MST and wireline NGR profiles, p. 51.



gamma log, but many of several other lesser peaks on the wireline record do not align easily with the MST data. This lack of alignment suggests minor drilling disruption or noise in the MST data. Below 70 mbsf the MST record is much less complete, but where intervals of five or more continuous meters were recorded, the trends match well with the corresponding depth-equivalent parts of the wireline record (Fig. F17B). From 70 to ~92 mbsf there are at least five spikes in the wireline data that may correlate with quartzo-feldspathic tuffs. The wireline record below 96 mbsf shows a succession of at least five cycles, each 10–15 m thick. Because the cores are incomplete below 90 mbsf, the record of a single cycle has not been entirely preserved.

Thermal Conductivity

Thermal conductivity measurements were made on Hole 1228A sediments at a rate of one per core (usually the third section, at 75 cm, if this was available). Values range between 0.71 and 1.29 W/(m·K) (average = 0.96 W/[m·K]) (Fig. F18). Thermal conductivities in excess of 1.20 W/(m·K) are present from 130 to 170 mbsf. This interval corresponds to the quartz-rich feldspar silts and sands of Subunit IIC, the interval of low downhole porosity. Average normalized thermal conductivity and bulk density show a high correlation (Fig. F18B), indicating that the thermal conductivity is a direct function of water content of the sediments. We note that the change in lithology between Unit I and II coincides with an abrupt change in the dominant grain thermal characteristics. Measurements where unfilled core liner or gravel slurry are present are flagged in Figure F18A.

Formation Factor

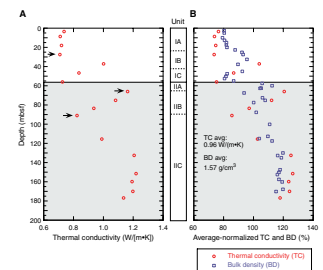
Formation factor (longitudinal and transverse) was determined for Hole 1228A as described in “Formation Factor,” p. 47, in “Physical Properties” in the “Explanatory Notes” chapter with a minimum of one sample per section or corresponding to distinct lithologic changes.

Longitudinal (parallel to core axis) formation factors range from 1.7 to 2.3 in the mainly biogenic sediments and 2.7 to 4.9 in the interbedded siliciclastic sediments of Unit I (Fig. F19). The layered character of Subunits IIA and IIB produce steplike changes in apparent conductivity, with formation factor measurements in quartz-bearing clays up to 5.8. Below 110 mbsf, the dominant lithology of feldspar silt and sand produces formation factors of 2.9–3.3. Low formation factors (~2.5) in this interval arise from the diatom ooze components of Subunit IIC. Electrical conductivity anisotropy typically ranges from 0% to 12% (average = 5%). Overall, the formation factor measurements track the changing lithostratigraphy, clearly delineating the sharp sedimentary changes in the upper 90 mbsf.

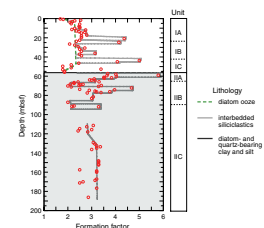
Summary and Discussion

Site 1228 has a complex physical property record. The signals result from a variety of lithologies—including silt and clay layers, ash layers, and gravel—and reflect drilling disturbance and include common hiatuses resulting from whole-round sampling. Discrete samples and wireline logs were essential for the interpretation of MST data. The characteristics of five distinct zones are summarized below:

F18. Thermal conductivity measurements, p. 52.



F19. Formation factor profile, p. 53.



1. 0–43 mbsf. The seafloor and a peak in magnetic susceptibility, density, and thermal conductivity at 43 mbsf bound this zone. It is characterized by fairly low magnetic susceptibility, density, and average *P*-wave velocities. It has common peaks that are present in magnetic susceptibility, density, porosity, and NGR records. The peaks correlate with silt layers in this interval. The zone corresponds to Subunits IA and IB.
2. 43–57 mbsf. This zone is bounded by peaks in magnetic susceptibility and density. Decreasing magnetic susceptibility and bulk density, low grain density, and high porosity are characteristic. It corresponds to Subunit IC. The boundary at 57 mbsf clearly marks the lithologic break between Units I and II.
3. 57–72 mbsf. This zone is bounded by peaks in magnetic susceptibility and density. High but variable bulk density and magnetic susceptibility, high grain density, and low porosity are characteristic. The peak at 72 mbsf is gravel located at the top of the core, and although this recovery position makes its apparent stratigraphic location suspect, it does represent the highest indication of gravel in the sequence. It is slightly below the Subunit IIA/IIB boundary.
4. 72–120 mbsf. This zone is bounded at the top by gravel at 72 mbsf and at the base by the termination of a series of physical property cycles. The cycles, each of which is at least 10 m thick, are characterized by gradual upward trends from low to high density and resistivity. Porosity is correspondingly low at the top of each cycle and high at the base. The partially complete lithostratigraphic record shows that the interval comprises interstratified clastic silts and silty sands, ashes, and biogenic layers. Although we have yet to correlate the lithologic and physical property records at a detailed scale, it seems clear that the cycles represent a variation of the terrigenous clastic input.
5. 120–200 mbsf. This zone is characterized by less clearly defined but still discernable trends in the partially complete physical property record. Overall magnetic susceptibility, bulk and grain density, and *P*-wave velocity are relatively higher than in the overlying sequence. Cycles present in the overlying zone are still present from 120 to 200 mbsf but are poorly defined by the density data. Instead, they stand out clearly on the NGR and are present in the resistivity logs. The cyclic pattern is also supported by the partial MAD and MST data.

Overall, the physical property data sets correlate well between the different measurements. A record of the compactional history is present with porosity decreasing downhole, whereas density and *P*-wave velocity increase. Superimposed on this general pattern at 10-m frequency is a record of the environmental fluctuation between marine and terrigenous sediment input within an overall transition from marginal to open-marine conditions. The wireline log and less complete MST and discrete sample physical data provide a template within which a sequence stratigraphic interpretation can be constructed.

DOWNHOLE TOOLS

At Site 1228, the downhole tools employed were the Adara temperature shoe, DVTP, DVTP-P, WSTP, APC-Methane (APC-M) tool, FPC, and

the PCS. The results of the temperature and pressure measurements at Site 1228 are described in the two sections below. A short summary of the other tool deployments is provided in the third section.

In Situ Temperature Measurements

Two reasonably good downhole temperature determinations were made in Hole 1228A using the DVTP. An Adara temperature shoe deployment before Core 201-1228A-1H yielded a value for the bottom-water temperature of 13.7°C. The WSTP deployments did not successfully record a value for bottom-water temperature. Figure F20 shows the data from the two successful DVTP deployments at 80.9 and 194.6 mbsf. Two other deployments at 42 and 137.9 mbsf resulted in records that could not be used. Table T9 summarizes all the temperature measurements and the observed problems.

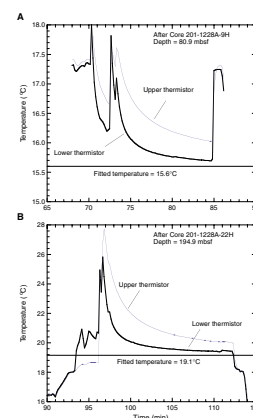
The results of the DVTP temperature estimates are displayed in Figure F21. In situ temperatures were estimated by extrapolation of the station data using thermal conductivities measured on adjacent cores to correct for the frictional heating on penetration as described in “Downhole Tools,” p. 49, in the “Explanatory Notes” chapter. For both of the successful Site 1228 deployments, the data from the lower thermistor were used to extrapolate the in situ temperature. Because we obtained only two good downhole temperature estimates at Site 1228, the results from Leg 112 Site 680 are given in the summary table and were included in the thermal gradient estimate.

The combined downhole temperatures of Sites 1228 and 680 define a gradient of 0.0336°C/m in the upper 196 m of the sediment column (Fig. F21). Extrapolating this gradient upward to the seafloor yields a bottom-water temperature 1.2°C lower than the measured value of 13.7°C. Specific data were not available on board the ship to verify whether 12.5°C is a reasonable value for the mean bottom-water temperature at Site 1228. The extrapolated temperature at the bottom of Hole 1228A, at 200.9 mbsf, is 19.3°C. Multiplying the gradient by an average thermal conductivity of 0.96 W/(m·K) (Fig. F18A) gives a conductive heat flow estimate of 32 mW/m² at Site 1228. This result is significantly lower than the 46-mW/m² estimate obtained for Site 680 by the Leg 112 Shipboard Scientific Party (1988b) but is closer to the estimates of 31 mW/m² obtained for Site 684 and 37 mW/m² for Site 1227. These lower values appear more reliable than the Site 680 estimate because they are based on measurements spanning a greater depth below seafloor.

Figure F21B shows a theoretical steady-state conductive temperature profile calculated using a constant heat flow of 31 mW/m² and the measured thermal conductivities from the Hole 1228A cores. The theoretical profile is noticeably curved because of the factor of 1.6 downhole increase in thermal conductivity (see Fig. F18). It is also worth noting that the measured temperature at 194.9 mbsf is 0.5°C higher than expected for a conductive trend.

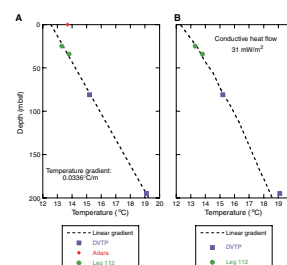
Comparing lithology and depth from locations that produced good and bad temperature data showed some differences that may be used to optimize future DVTP deployments. The two successful deployments were located at 80.9 and 194.9 mbsf. The sediments surrounding the first location were composed of diatom-rich silty clay, and recoveries averaged 70% (Cores 201-1228A-9H and 10H). The second location, near the base of the hole, was overlain by clay-bearing quartz feldspar sand, and recovery was 41% (Core 201-1228A-22H). Two failed deploy-

F20. DVTP temperature records, p. 54.



T9. Downhole temperature measurements, p. 71.

F21. Temperature data vs. depth, p. 55.

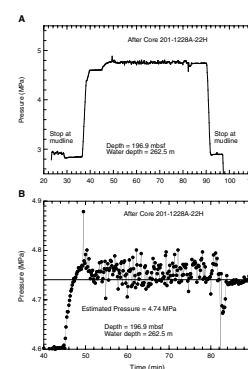


ments were located at 42.9 and 137.9 mbsf. The first interval was composed of silt, ash, and diatom ooze, and the recoveries for the surrounding cores (Cores 201-1228A-5H and 6H) were 80% and 98%. However, for sediments cored in Hole 1228B over this same interval, recovery dropped to 60% (Core 201-1228B-5H). The worst deployment was at 137.9 mbsf in sandy clay, where no sediments were recovered in the subsequent core (Core 201-1228A-17H). Site 1228 was located in shallow water at a depth of 261 m. These observations indicate that at shallow-water sites where recoveries can be poor, deployments may be more successful deeper in the hole and in intervals with higher recoveries.

Davis-Villinger Temperature-Pressure Probe

The DVTP-P was deployed once at Site 1228 at a depth of 196.9 mbsf (after Core 201-1228A-22H). The record displayed in Figure F22 shows only a small pressure increase when the tool was pushed into the sediments. The pressure dropped within 3 min to ~4.74 MPa, which equals the predicted hydrostatic value for the hole depth and measured salinity gradient. For the remainder of the 30-min deployment, the pressure oscillated at 4.76 ± 0.02 MPa. The amplitude of the oscillation corresponds to ~4 m of head, making it larger than the recorded ~1-m heave of the ship during the deployment. However, periodic displacement of the drill pipe in the borehole could amplify the oscillations caused by heave.

F22. DVTP-P pressure, p. 56.



Other Tools

After two failed deployments of the WSTP above Hole 1228A, a sample of bottom water was successfully collected from 10 m above the seafloor at Hole 1228C. Chlorinity data showed that this sample deviated <7% from International Association of the Physical Sciences of the Ocean standard seawater (see “[Interstitial Water](#),” p. 12, in “[Biogeochemistry](#)”). The APC-M tool was successfully run continuously from Cores 201-1228A-9H through 12H and on Core 14H. The tool appeared to function correctly, and the data will be analyzed postcruise. The FPC was tested three times at Site 1228 at 7.3, 54.3, and 109.4 mbsf (Cores 201-1228E-2M, 201-1228B-7M, and 201-1228A-13M, respectively). Because of a number of mechanical problems, the FPC failed to retrieve pressurized cores on any of the deployments. The one attempted use of the PCS (Core 201-1228A-23P) resulted in only 7 cm of recovery from the 2-m cored interval. This core released ~60 mL of air when it was opened to atmospheric pressure.

DOWNHOLE LOGGING

Operations

When the bit of the PCS was lost while coring Core 201-1228A-23P (see “[Hole 1228A](#),” p. 5, in “[Operations](#)”), it became impossible to drill any deeper with the APC in this hole and we decided to log Hole 1228A. One logging run was made with the triple combo tool string (see “[Downhole Logging](#),” p. 53, in the “[Explanatory Notes](#)” chapter). After recovery of the damaged PCS at 1300 hr on 5 March, the hole was conditioned for logging. A wiper trip indicated that there was no fill at the bottom of the hole. The hole was then displaced with 100 bbl of se-

piolite, and the bottom of the drill string was positioned at 80 mbsf. Logging rig-up started at 1715 hr. The 35-m-long logging string started downhole at 1930 hr, and two passes were made without difficulty. Both passes reached the bottom of the hole at the wireline depth 201 mbsf (477 meters below rig floor), and the bottom of the drill string was raised by 10 m during logging, allowing us to record data in the open hole to 70 mbsf. Logging operations and rig-down were completed by 0000 hr on 6 March (see Table T10 for a detailed summary of the operations).

Data Quality

The caliper log (Fig. F23A) shows that the borehole wall was generally smooth and that the caliper arm maintained good contact with the formation over the entire logged interval, a requirement for high-quality data recording. Because of the generally poor core recovery below 90 mbsf, physical property measurements were made on fewer samples than at the previous sites, but the MAD density and porosity data available generally agree with the logs (Fig. F23E, F23F). This agreement is particularly critical to the interpretation and relocation of the discrete measurements, as the average recovery below 70 mbsf was ~40%.

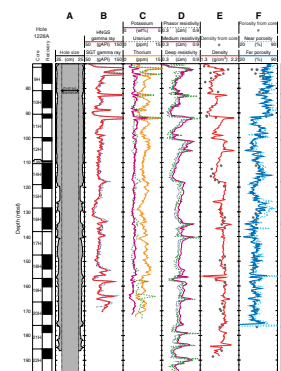
Because of the short length of the open hole interval (~130 m), a second pass was made over its entire length to ensure data quality. Figure F24 compares some of the logs of the two passes (pass 1 = dashed green line and pass 2 = solid red line). The density and resistivity logs from the two passes overlap almost perfectly. The gamma radiation values from the second pass are slightly higher than those for the first pass, indicating that the formation is still activated because of the minitron source of the Accelerator Porosity Sonde used during the first pass (see “Downhole Logging,” p. 53, in the “Explanatory Notes” chapter). However, despite this generally uniform offset, both gamma ray logs agree very well, except for a spike recorded during the first pass at 164 mbsf, which does not appear in the second pass. Figure F23C indicates that this spike is created by an increase in uranium. Because the two independent gamma ray sensors recorded this spike during the first pass (see Fig. F23B), it must correspond to some lithologic feature and could indicate the presence of a uranium-rich nodule near the borehole wall. Because the sensors follow different paths along the borehole wall during successive logging passes, a discrete uranium-rich module might be detected on one pass and missed on another.

Logging Stratigraphy

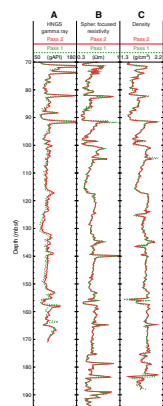
The general trend of the logs is characteristic of a transgressive margin. A high concentration of terrigenous sediments, predominantly clays and silts (see “Lithostratigraphy,” p. 7) generates generally high gamma ray values. Most logs, particularly the resistivity, gamma ray, and density logs, show a succession of sedimentation cycles indicating fluctuations in sea level over the depositional history of the site. Most cycles are 10 to 20 m thick and are characterized by an upward increase in density, resistivity, and gamma radiation. This is the signature of fining-upward facies typical of transgressive margins, where the finer clay-rich sediments settle on top of the sequence as sea level rises or the basin sinks (Rider, 1996). Based on variations in the trends of these cycles, we have identified three logging units, divided into logging subunits corresponding predominantly to individual cycles.

T10. Logging operations, p. 72.

F23. Main logs, p. 57.



F24. Two passes of the tool string, p. 58.



Logging Unit 1 (70–91 mbsf) is characterized by very strong peaks in gamma radiation and in uranium content. These peaks are present at the top of the two sedimentation cycles corresponding to logging Subunit 1A (70–82 mbsf) and logging Subunit 1B (82–91 mbsf) and are similar to features observed in the logs recorded in Hole 679E, located seaward of the Salaverry Basin. Similar spikes were attributed to the presence of uranium-bearing phosphorite layers created by the reworking of phosphate nodules (Shipboard Scientific Party, 1988a). Logging Unit 1 corresponds to the lower part of lithostratigraphic Subunit IIB, described as an alternation of diatom- and quartz-bearing clay and silt with quartz-rich lithic sand (see “[Description of Lithostratigraphic Units](#),” p. 7, in “Lithostratigraphy”).

The top of logging Unit 2 (91–135 mbsf) is identified by a strong peak in gamma radiation, resistivity, and density and by a sharp decrease in porosity, from values averaging 70% to values of ~50% (see Fig. [F23F](#)). Like the underlying logging Unit 3, this portion of the section was characterized by a low core recovery and is included in lithostratigraphic Subunit IIC, composed of diatom- and quartz-rich silts and sands. This logging unit is made of three sedimentation cycles identified as logging Subunits 2A (91–101 mbsf), 2B (101–118 mbsf), and 2C (118–135 mbsf). Logging Subunits 2A and 2B display clear increases upsection in resistivity and density, with a more subtle increase in gamma radiation. By comparison, the upsection increase in gamma radiation in logging Subunit 2C is more pronounced than the resistivity and density trends.

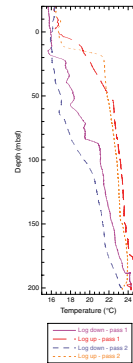
Logging Unit 3 (135–200 mbsf) is characterized by almost uniform porosity and density values and by a slight but steady decrease in resistivity with depth, interrupted by several spikes. These spikes are possibly created by layers of hard sandstone cemented by calcitic dolomite that were recovered by the Shipboard Scientific Party (1988b). Logging Unit 3 can be divided into three subunits based on the occurrence of these spikes, which could also correspond to deposition cycles less well defined than those in logging Unit 2. Logging Subunit 3A (135–156 mbsf) shows almost uniform gamma ray counts, despite a subtle increase in thorium, and a slight decrease with depth in resistivity and density. The top of logging Subunit 3B (156–176 mbsf) is defined by a negative spike in resistivity and density and by an increase in uranium. Logging Subunit 3B (176–200 mbsf) was logged fully only by the resistivity sonde, located at the bottom of the tool string (see “[Downhole Logging](#),” p. 53, in the “Explanatory Notes” chapter) but is defined by a clear decrease in resistivity and by a series of strong and closely spaced resistivity spikes, indicating cemented dolomitic layers.

Temperature Log

Temperatures were recorded with the Lamont-Doherty Earth Observatory Temperature/Acceleration/Pressure (TAP) memory tool attached at the bottom of the triple combo tool string. Because only a few hours had passed since the end of drilling operations and hole conditioning, the borehole temperature is not representative of the actual equilibrium temperature distribution of the formation. In the case of Hole 1228A, the surface seawater and the sepiolite mud pumped during and after drilling generated borehole fluid temperatures higher than the formation temperatures. Discrete measurements made with the DVTP indicate a maximum formation temperature of 19.1°C at 194.9 mbsf (see “[In Situ Temperature Measurements](#),” p. 24, in “Downhole Tools”),

whereas the maximum temperature recorded by the TAP tool at 201 mbsf is 24.75°C at 190 mbsf (see Fig. F25). The generally lower temperatures during pass 2 indicate a progressive return to equilibrium. The apparent anomalies measured at 70 and 80 mbsf while logging downhole correspond to the tool exiting the drill string. The changes in trends on the uphole passes correspond to increases of the tool velocity at the end of each pass. The absence of significant anomalies in this profile that could not be attributed to operations shows that any hydrologic activity is absent or of low intensity.

F25. Hole 1228A temperature log, p. 59.



REFERENCES

- Cragg, B.A., Parkes, R.J., Fry, J.C., Herbert, R.A., Wimpenny, J.W.T., and Getliff, J.M., 1990. Bacterial biomass and activity profiles within deep sediment layers. *In* Suess, E., von Huene, R., et al., *Proc. ODP, Sci. Results*, 112: College Station, TX (Ocean Drilling Program), 607–619.
- Fossing, H., 1990. Sulfate reduction in shelf sediments in the upwelling region off Central Peru. *Cont. Shelf Res.*, 10:355–367.
- Kastner, M., Elderfield, H., Martin, J.B., Suess, E., Kvenvolden, K.A., and Garrison, R.E., 1990. Diagenesis and interstitial-water chemistry at the Peruvian continental margin—major constituents and strontium isotopes. *In* Suess, E., von Huene, R., et al., *Proc. ODP, Sci. Results*, 112: College Station, TX (Ocean Drilling Program), 413–440.
- Merrill, D.L., Ohnstad, T., and McCabe, R., 1990. Magnetic susceptibility measurements of Leg 112 cores. *In* Suess, E., von Huene, R., et al., *Proc. ODP, Sci. Results*, 112: College Station, TX (Ocean Drilling Program), 677–683.
- Mossmann, J.-R., Aplin, A.C., Curtis, C.D., and Coleman, M.L., 1990. Sulfur geochemistry at Sites 680 and 686 on the Peru margin. *In* Suess, E., von Huene, R., et al., *Proc. ODP, Sci. Results*, 112: College Station, TX (Ocean Drilling Program), 455–464.
- Parkes, R.J., Cragg, B.A., Fry, J.C., Herbert, R.A., and Wimpenny, J.W.T., 1990. Bacterial biomass and activity in deep sediment layers from the Peru margin. *Philos. Trans. R. Soc. London A*, 331:139–153.
- Parkes, R.J., Cragg, B.A., Getliff, J.M., Harvey, S.M., Fry, J.C., Lewis, C.A., and Rowland, S.J., 1993. A quantitative study of microbial decomposition of biopolymers in Recent sediments from the Peru Margin. *Mar. Geol.*, 113:55–66.
- Rider, M., 1996. *The Geological Interpretation of Well Logs* (2nd ed.): Houston (Gulf Publishing Co.).
- Rowe, G.T., and Howarth, R., 1985. Early diagenesis of organic matter in sediments off the coast of Peru. *Deep-Sea Res.*, 32:43–55.
- Shipboard Scientific Party, 1988a. Site 679. *In* Suess, E., von Huene, R., et al., *Proc. ODP, Init. Repts.*, 112: College Station, TX (Ocean Drilling Program), 159–248.
- , 1988b. Site 680. *In* Suess, E., von Huene, R., et al., *Proc. ODP, Init. Repts.*, 112: College Station, TX (Ocean Drilling Program), 249–304.
- Smith, D.C., Spivack, A.J., Fisk, M.R., Haveman, S.A., Staudigel, H., and ODP Leg 185 Shipboard Scientific Party, 2000. Methods for quantifying potential microbial contamination during deep ocean coring. *ODP Tech. Note*, 28 [Online]. Available from the World Wide Web: <<http://www-odp.tamu.edu/publications/tnotes/tn28/INDEX.HTM>>. [2002-03-30]
- Suess, E., von Huene, R., et al., 1988. *Proc. ODP, Init. Repts.*, 112: College Station, TX (Ocean Drilling Program).
- Yamano, M., and Uyeda, S., 1990. Heat-flow studies in the Peru Trench subduction zone. *In* Suess, E., von Huene, R., et al., *Proc. ODP, Sci. Results*, 112: College Station, TX (Ocean Drilling Program), 653–661.

Figure F1. Lithostratigraphic summary at Site 1228. TD = total depth.

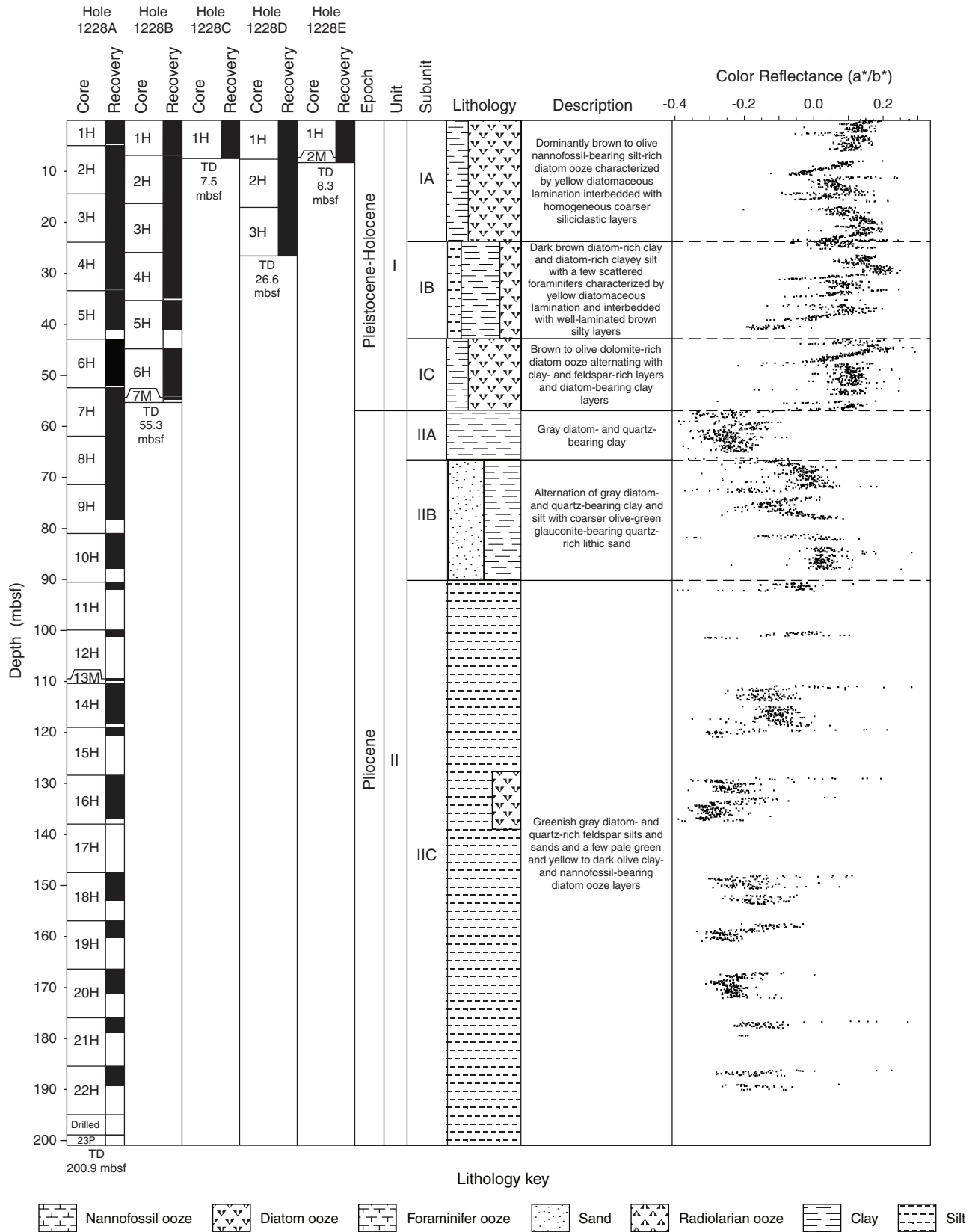


Figure F2. Lithostratigraphic summary for Site 1228 compared with magnetic susceptibility and porosity data. TD = total depth.

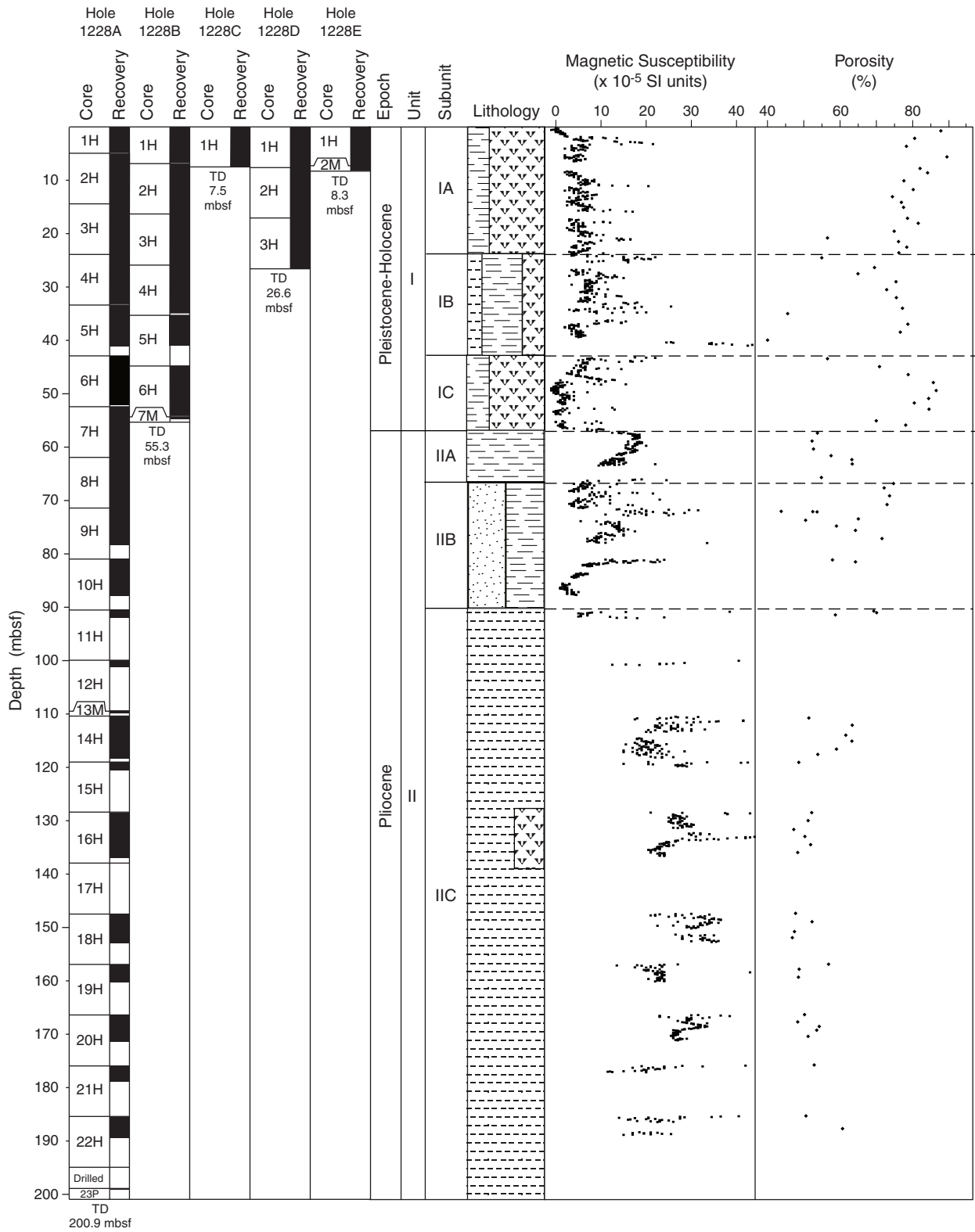


Figure F3. Close-up photographs. A. Gray volcanic ash layers in Subunit IA. B. High-angle lamination, probably due to rotational slumping in Subunit IA. (Continued on next three pages.)

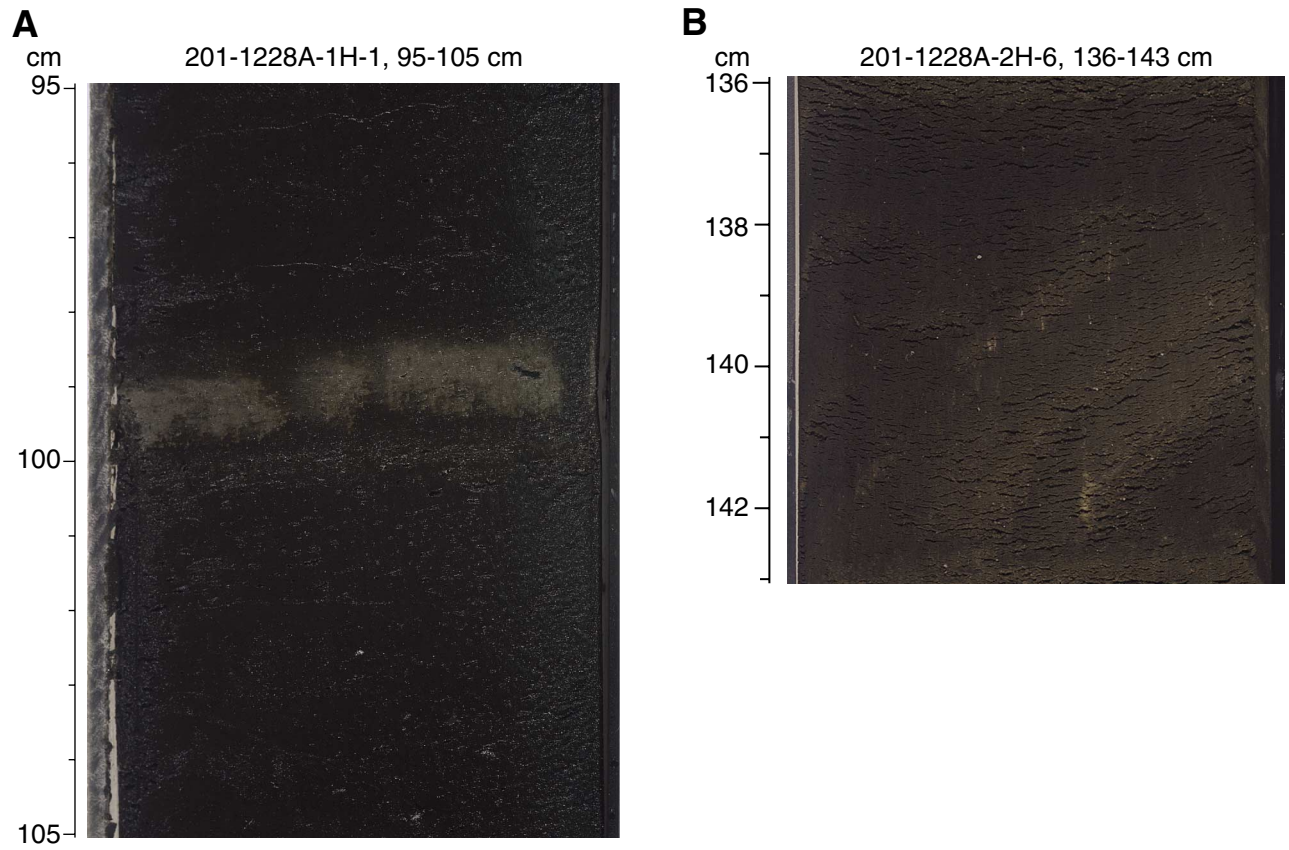


Figure F3 (continued). C. Characteristic features of Subunit IC including cross-lamination of silty layers and a gray clayey layer. D. Dark D-phosphate concretions (probably hardground) in Subunit IC. (Continued on next page.)

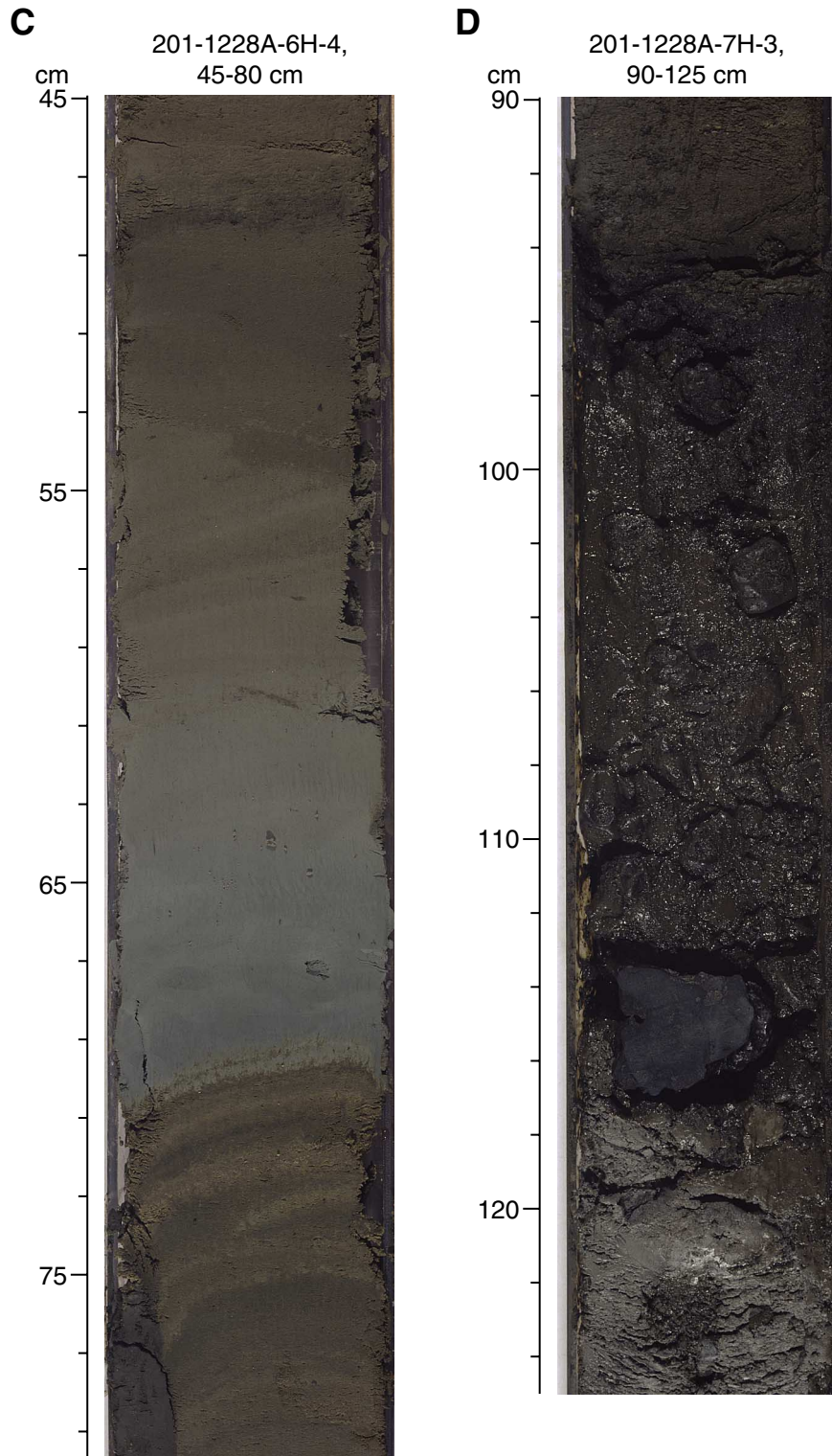


Figure F3 (continued). E. Yellow dolomite lens replacing a former silt-sized sediment in Subunit IC. F. Cross-lamination and gray clayey layer in Subunit IIB. (Continued on next page.)

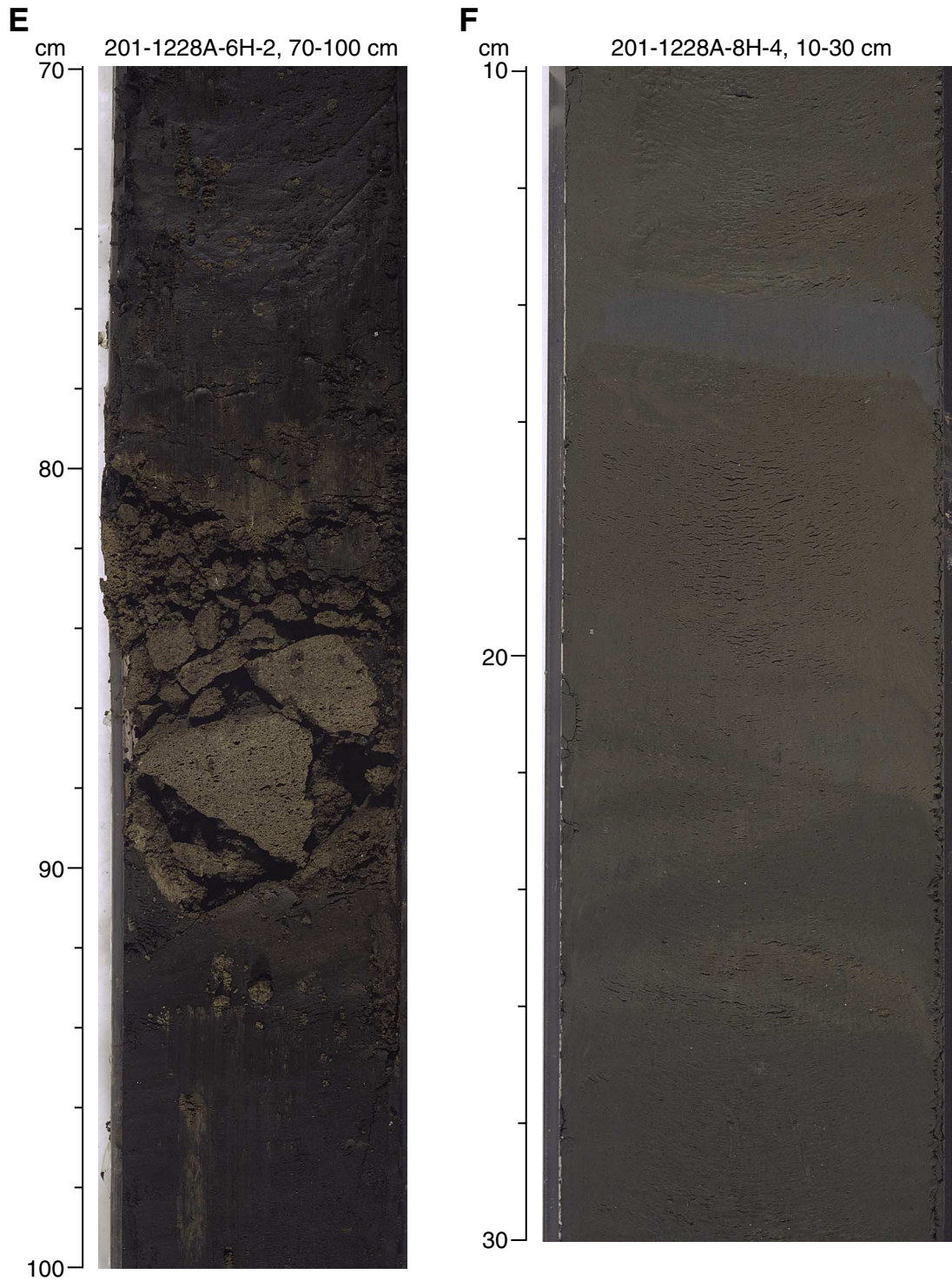


Figure F3 (continued). G. Erosional contact between cross-laminated sand to silt-sized layers (above 47 cm) and diatom-rich silty clay (below 47 cm) in Subunit IIB.

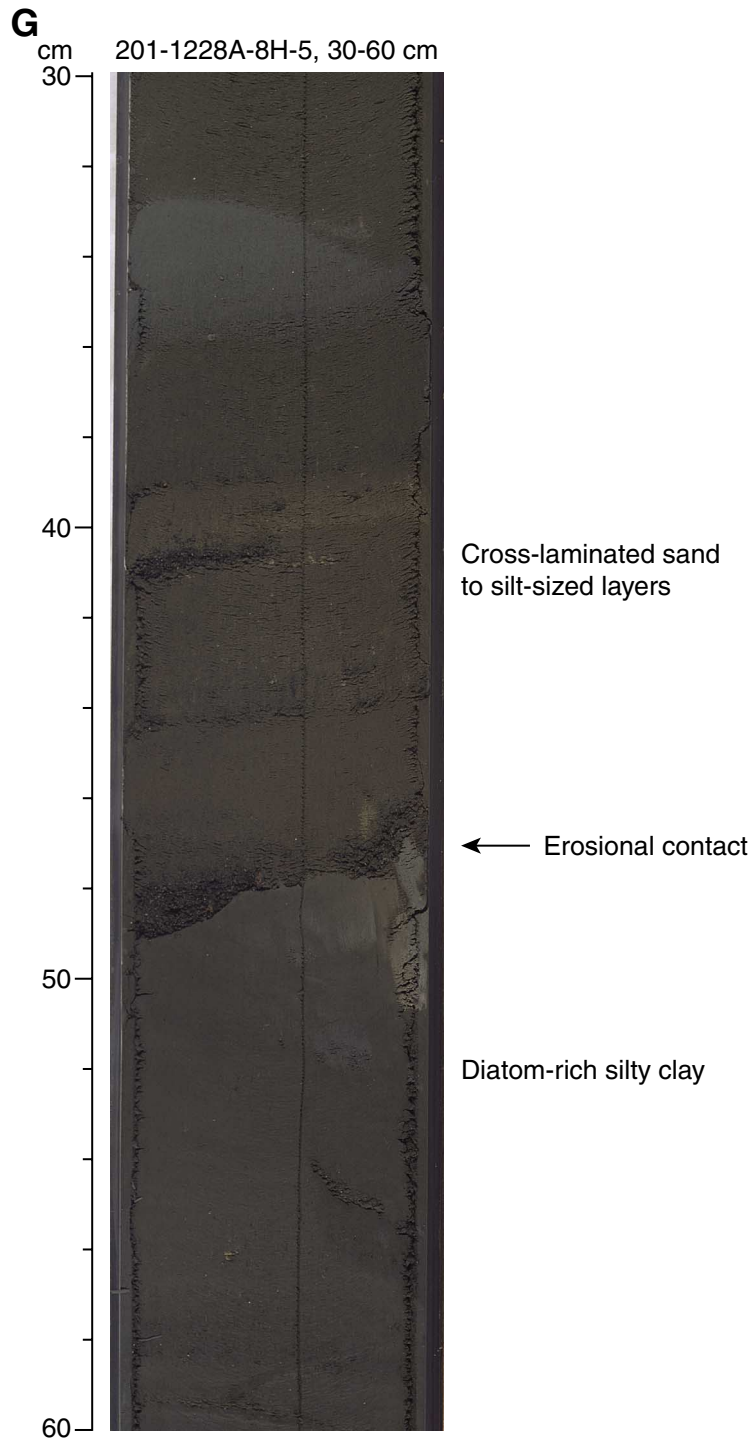


Figure F4. X-ray diffractograms of selected lithologies from Site 1228. **A.** Yellow diatom-rich layer containing opal-A and dolomite in Subunit IB. **B.** Black vitreous porcelanite nodule from Subunit IC. **C.** Gray homogeneous silt layer from Subunit IIA. **D.** Black D-phosphate nodule from Subunit IC. **E.** Pink F-phosphate apatite nodule from Subunit IIC. **F.** Green dolomite nodule from Subunit IIC. D = dolomite, Q = quartz, An = plagioclase (anorthite), C = calcite, A = apatite.

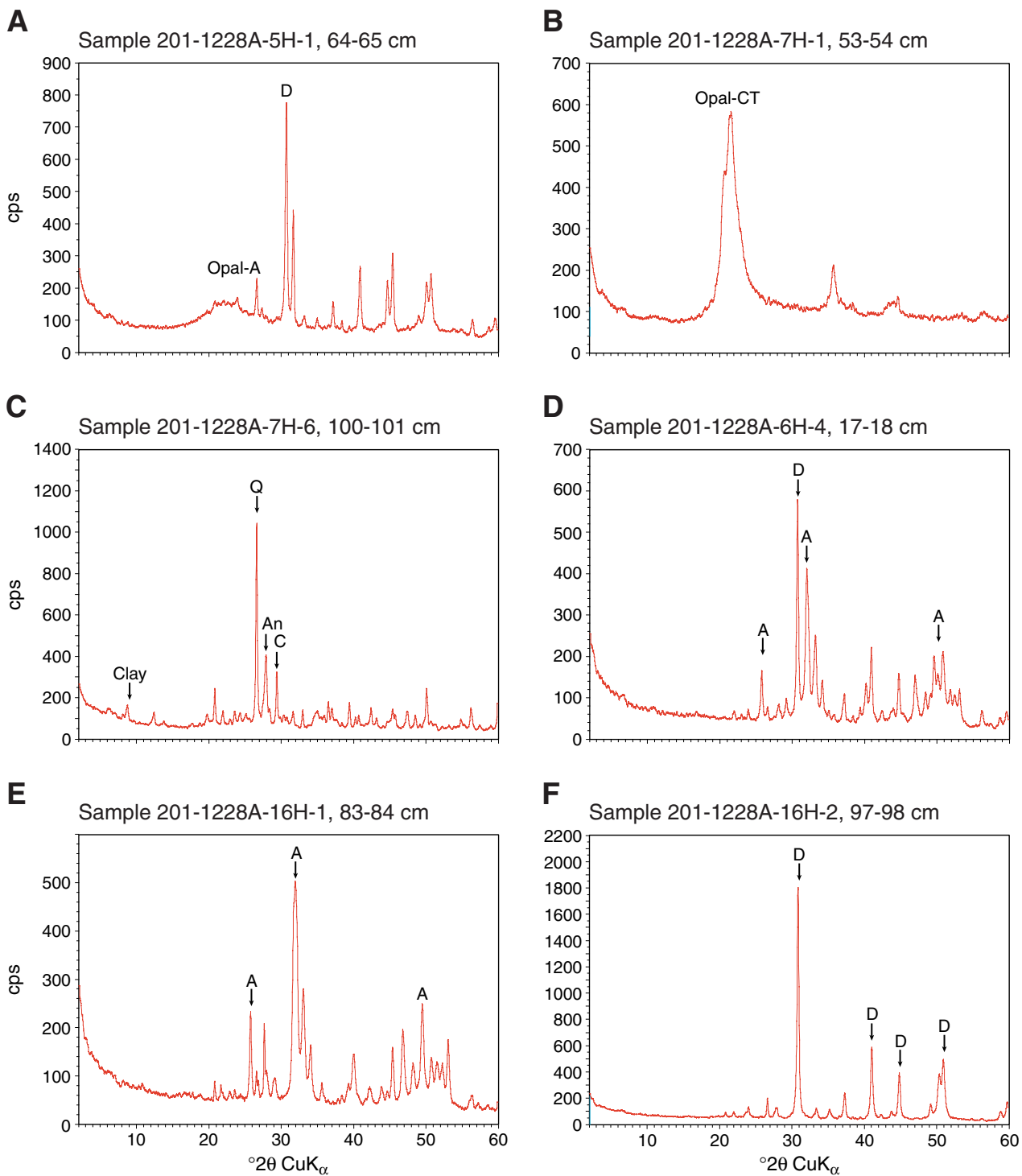


Figure F5. Concentrations of various dissolved species in interstitial waters from Site 1228. A. Alkalinity. B. Dissolved organic carbon (DIC). C. Manganese. D. Iron. E. Total sulfide. F. Sulfate. G. Barium. (Continued on next two pages.)

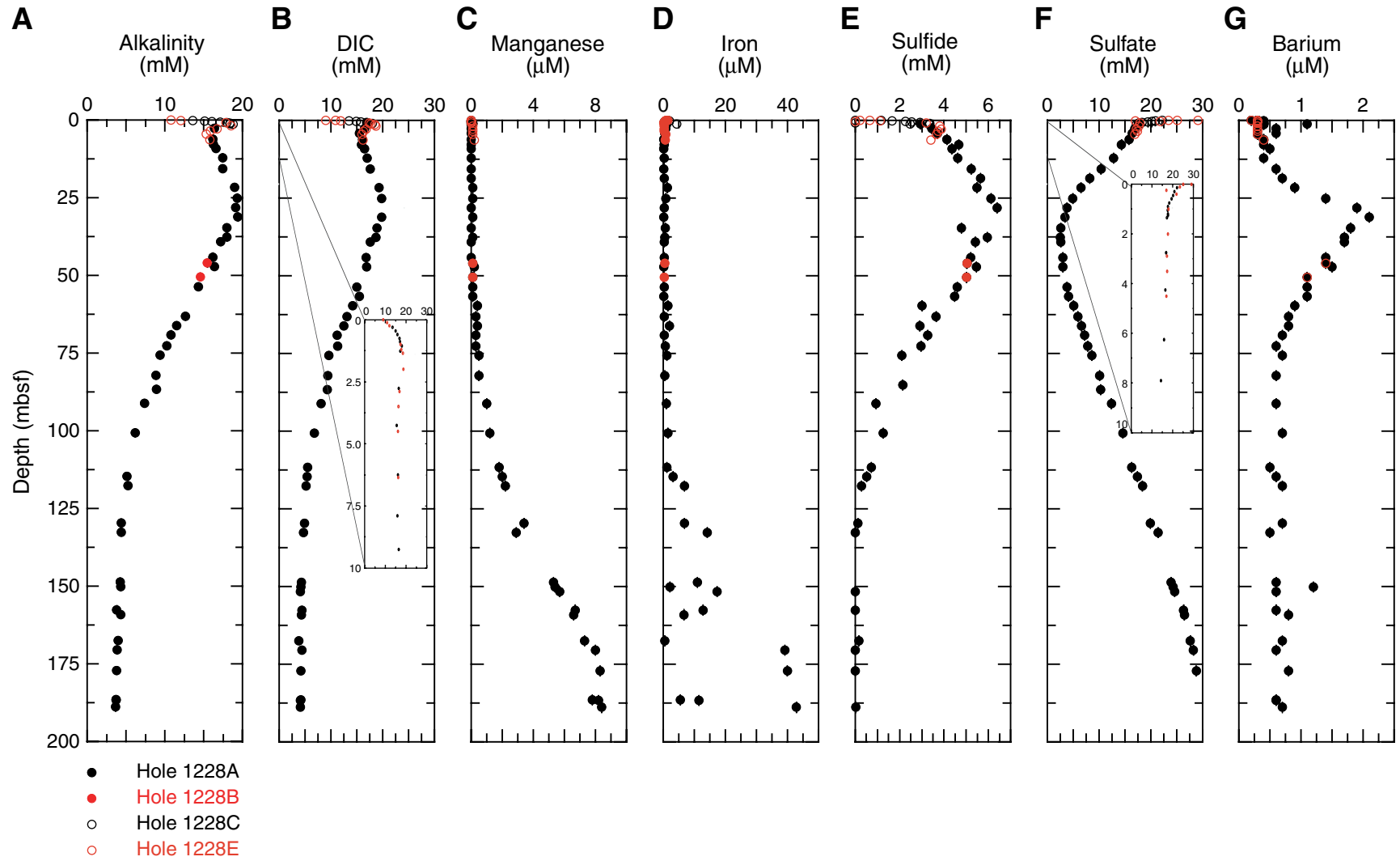


Figure F5 (continued). H. Methane. I. Acetate and formate. J. Ammonium. K. Phosphate. L. Silica. M. Chloride. N. Strontium. (Continued on next page.)

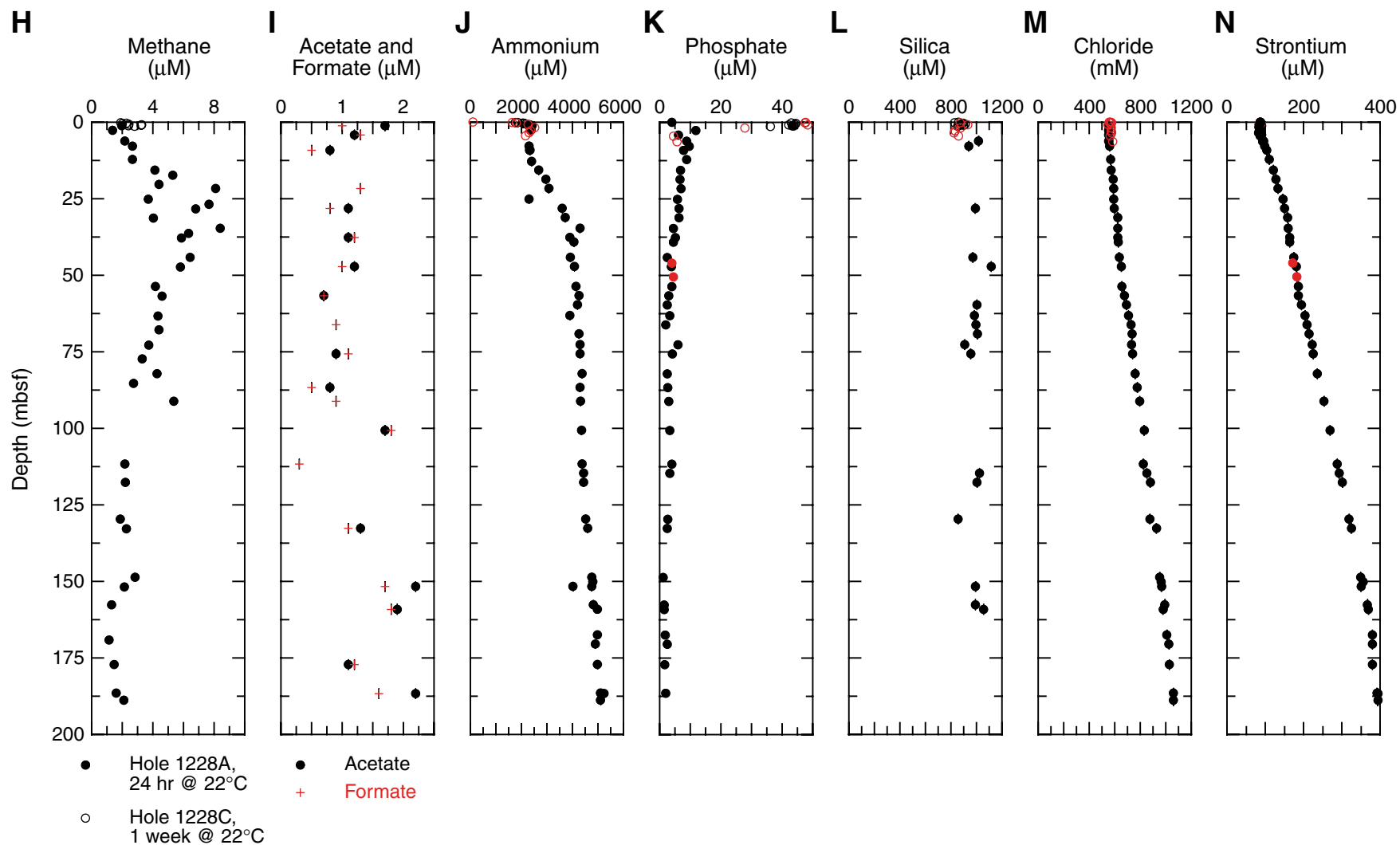


Figure F5 (continued). O. Lithium. P. Hydrogen.

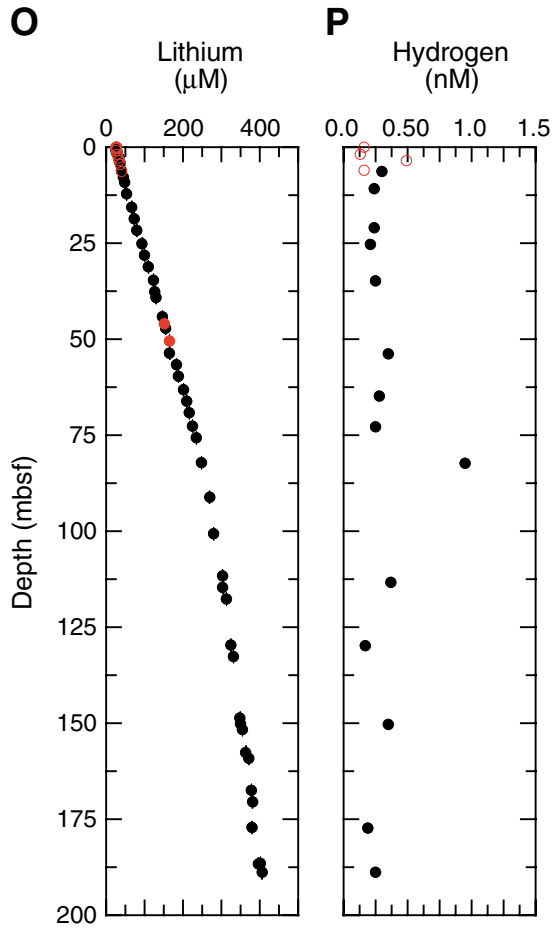


Figure F9. Comparison of magnetic susceptibility data. A. MST for Hole 1228A. B. Postcruise data from Hole 680A (Merrill et al., 1990). C. Expanded plot from Hole 1228A, 0–42 mbsf.

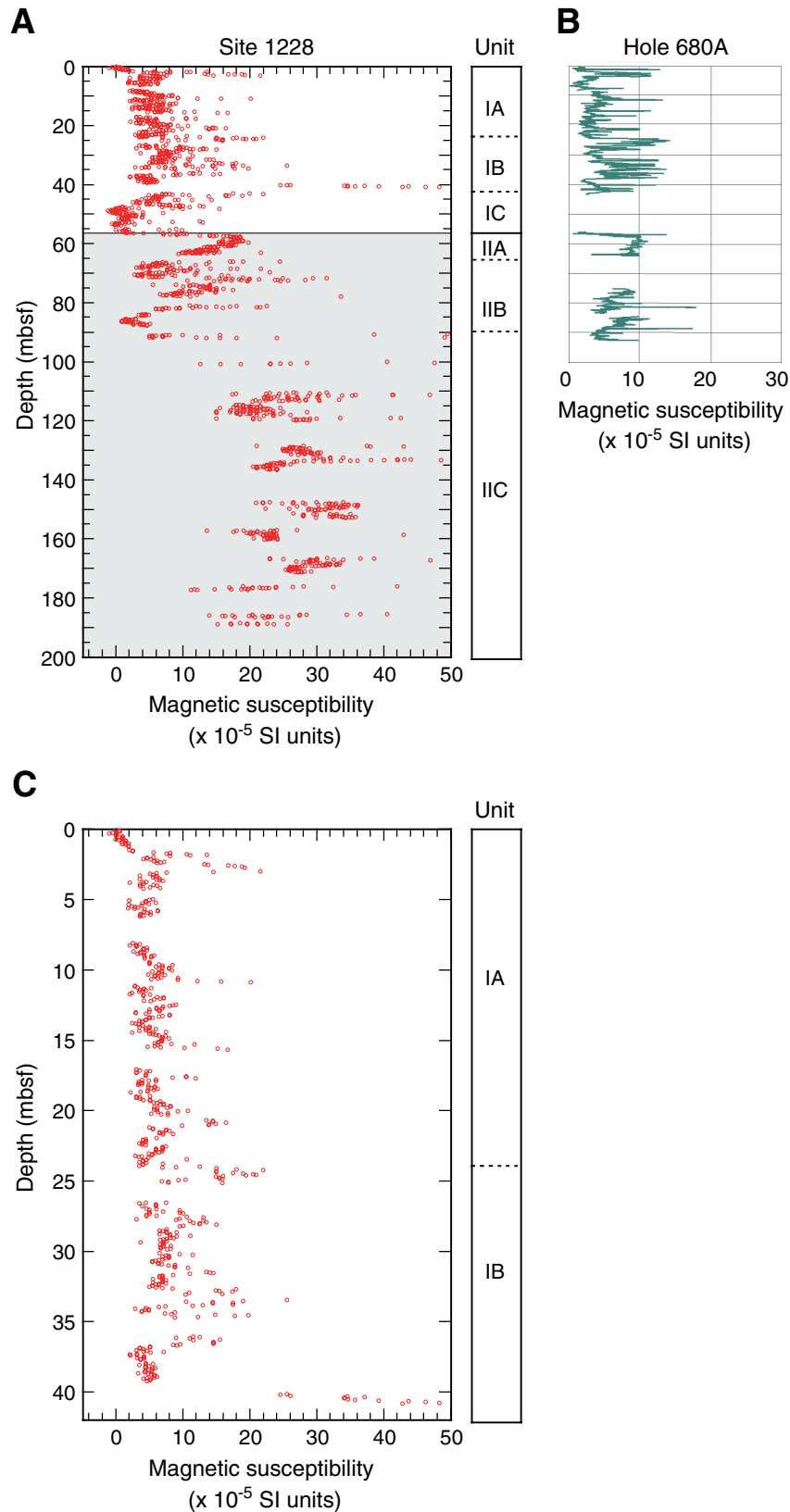


Figure F10. Magnetic intensity and susceptibility in Hole 1228A. Open squares = NRM intensity, solid squares = intensity after 20-mT AF demagnetization.

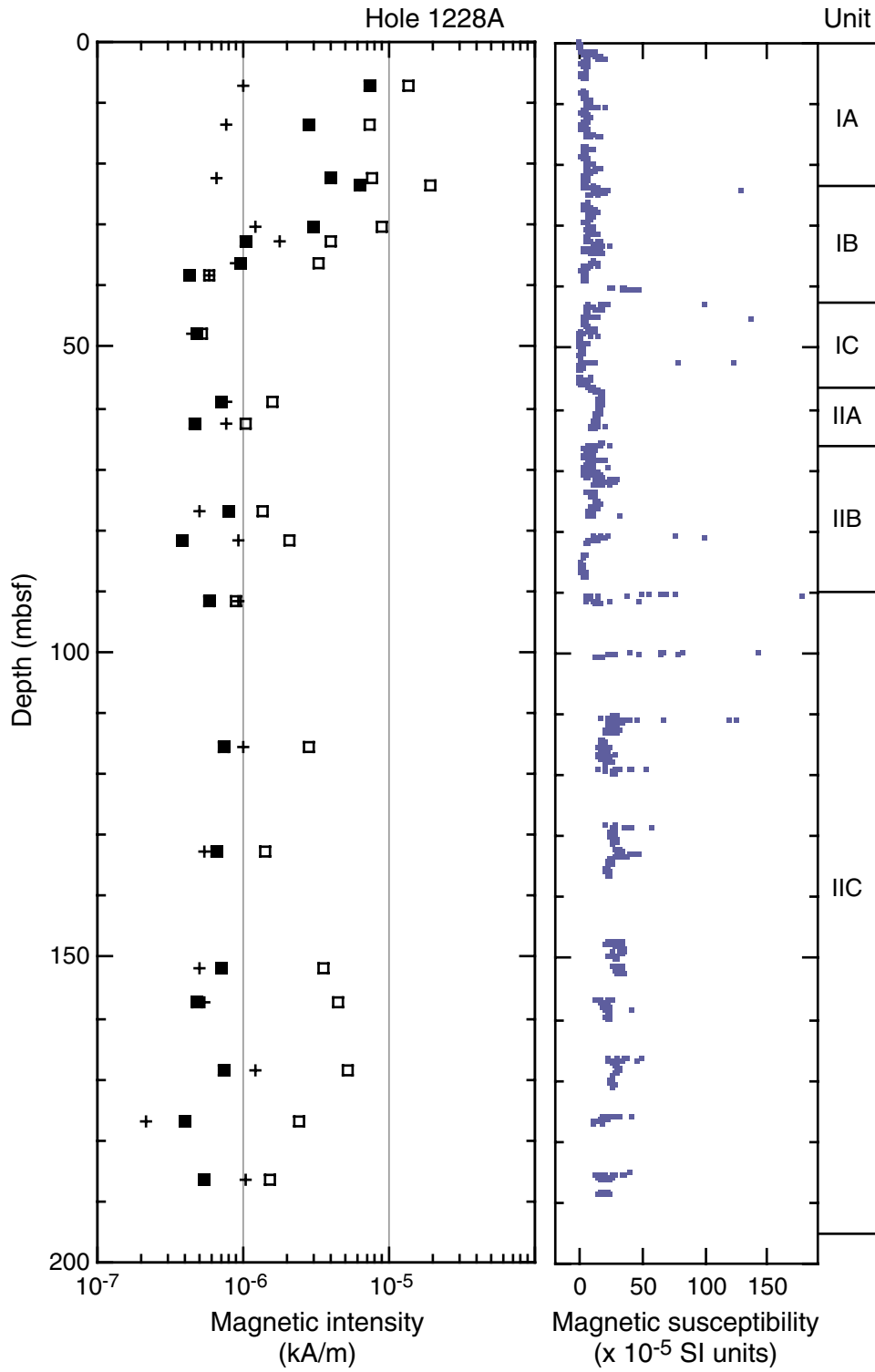


Figure F11. Principal component analysis of natural remanent magnetization (NRM) of Sample 201-1228A-2H-2, 65–67 cm, including equal area projection of directions of magnetization during demagnetization, intensity of magnetization plotted vs. demagnetization, and vector component diagrams showing projection of magnetic vector's endpoints on horizontal and vertical planes.

Sample 201-1228A-2H-2, 65-67 cm

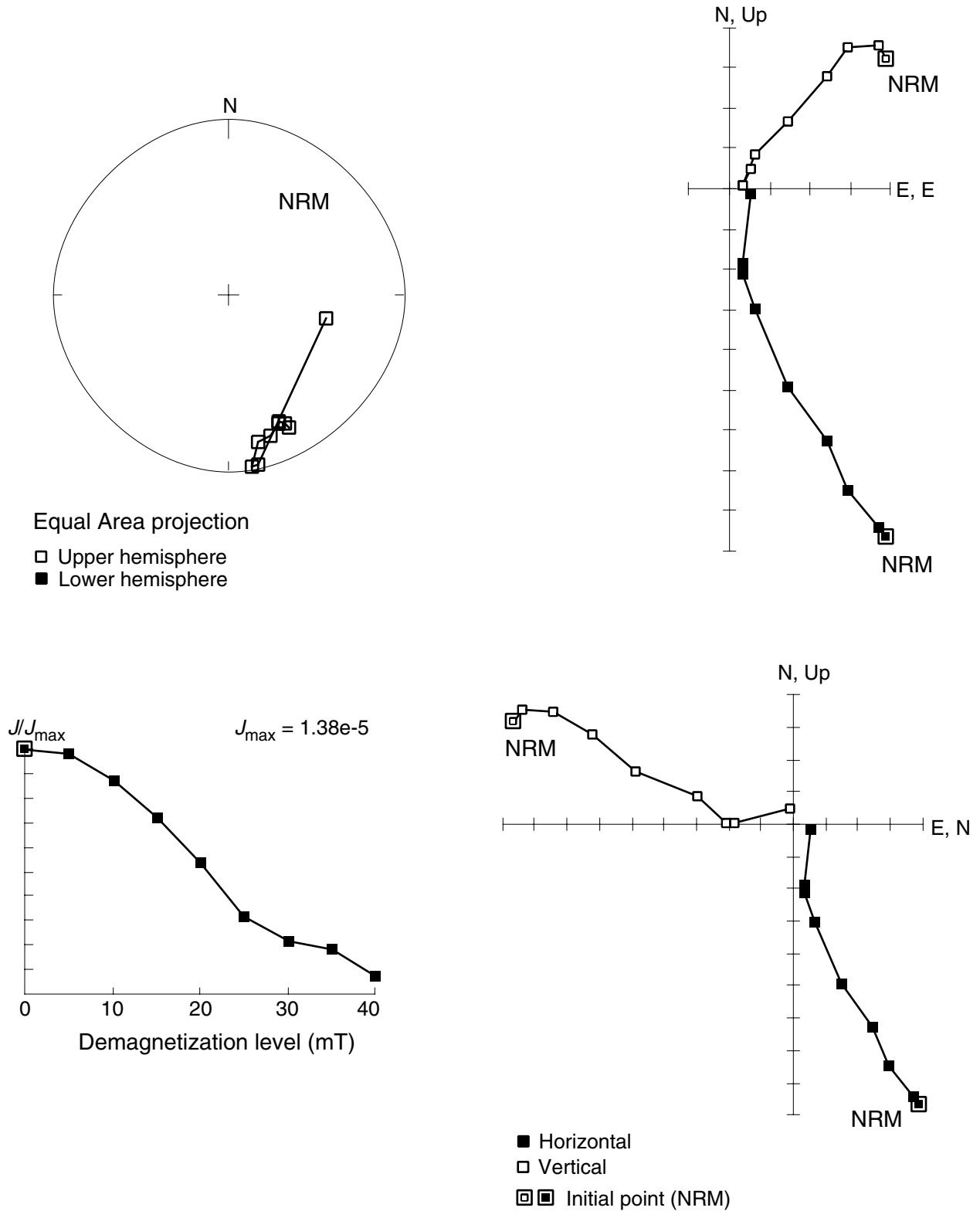


Figure F12. Principal component analysis of natural remanent magnetization (NRM) of Sample 201-1228A-3H-7, 5-7 cm including equal area projection of directions of magnetization during demagnetization, intensity of magnetization plotted vs. demagnetization, and vector component diagrams showing projection of magnetic vector's endpoints on horizontal and vertical planes.

Sample 201-1228A-3H-7, 5-7 cm

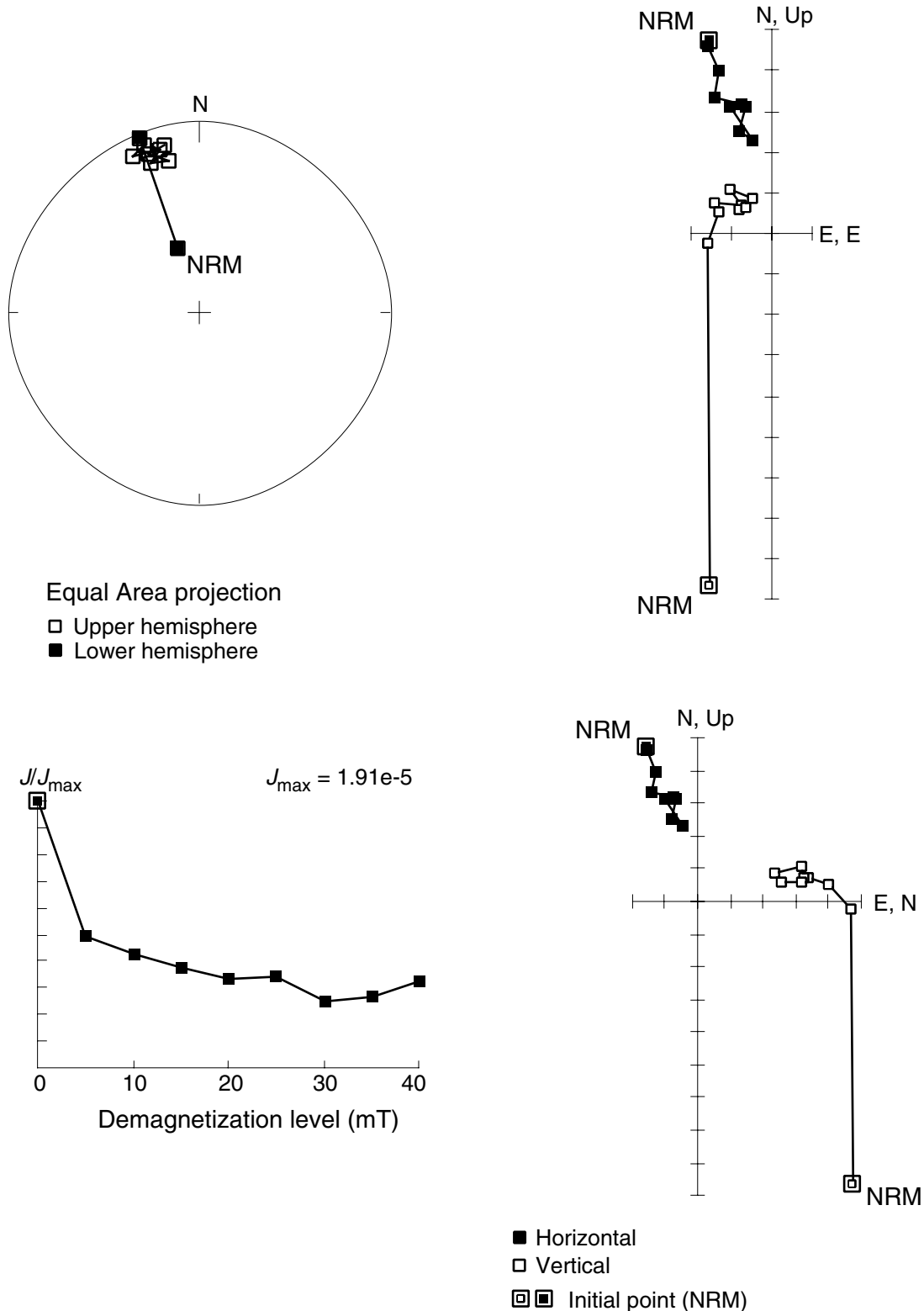


Figure F13. A. Gamma ray attenuation (GRA) bulk and moisture and density (MAD) data from Hole 1228A compared with the wireline density log from the same hole. B. Expanded depth scale for Unit I data.

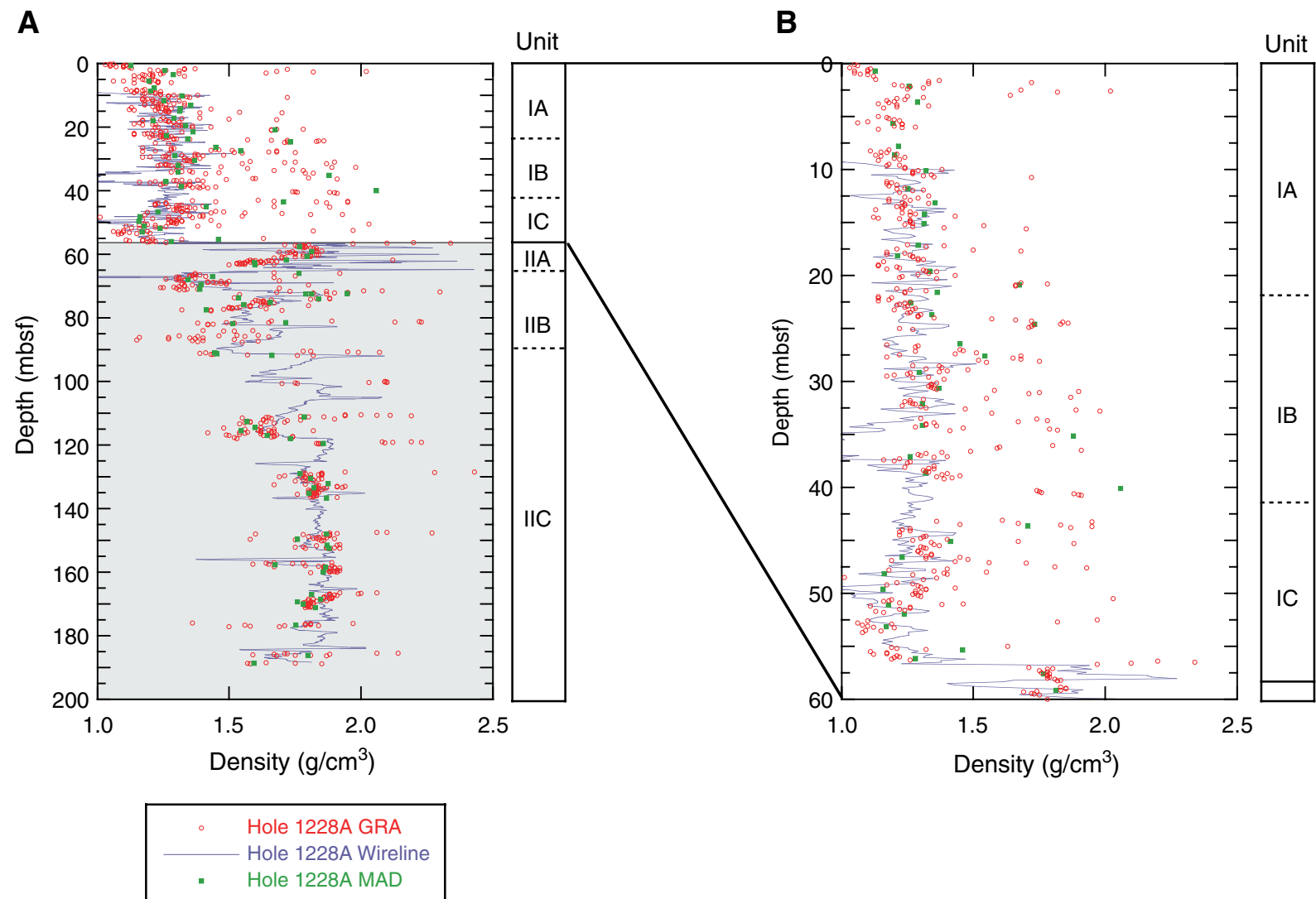


Figure F14. Comparison of 5-m moving averages of gamma ray attenuation (GRA) bulk density from Holes 1228A and 680A and mass/volume-based (MAD) densities measured on discrete samples from Hole 1228A.

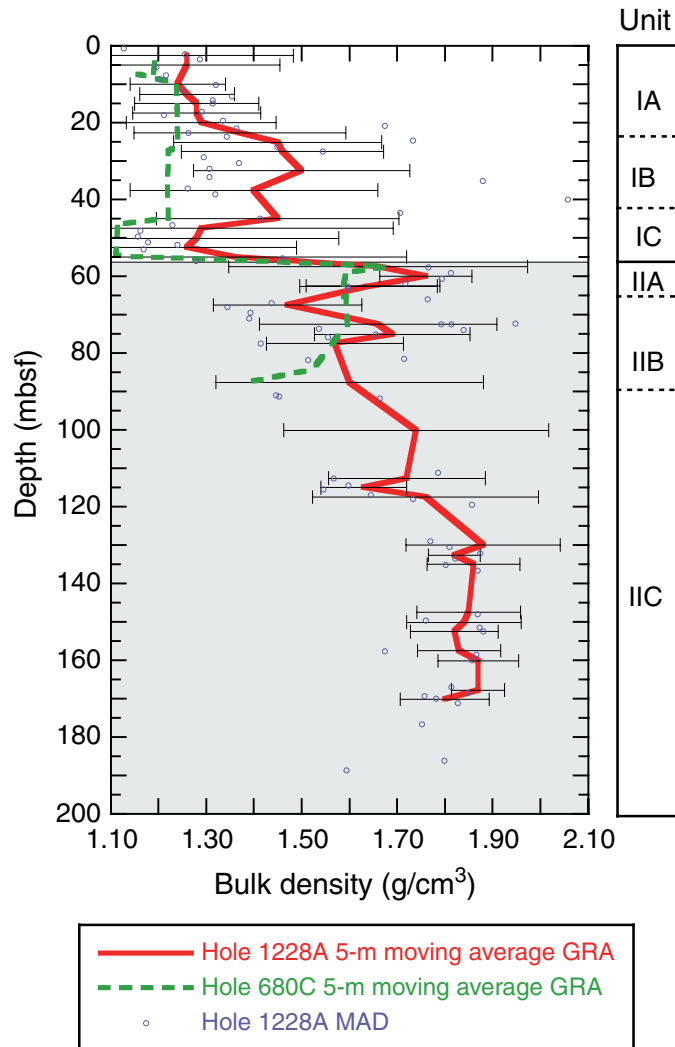


Figure F15. Mass/volume measurements for Hole 1228A. A. Gamma ray attenuation (GRA) and moisture and density (MAD) bulk density profiles. B. Grain density profile. C. Porosity profile.

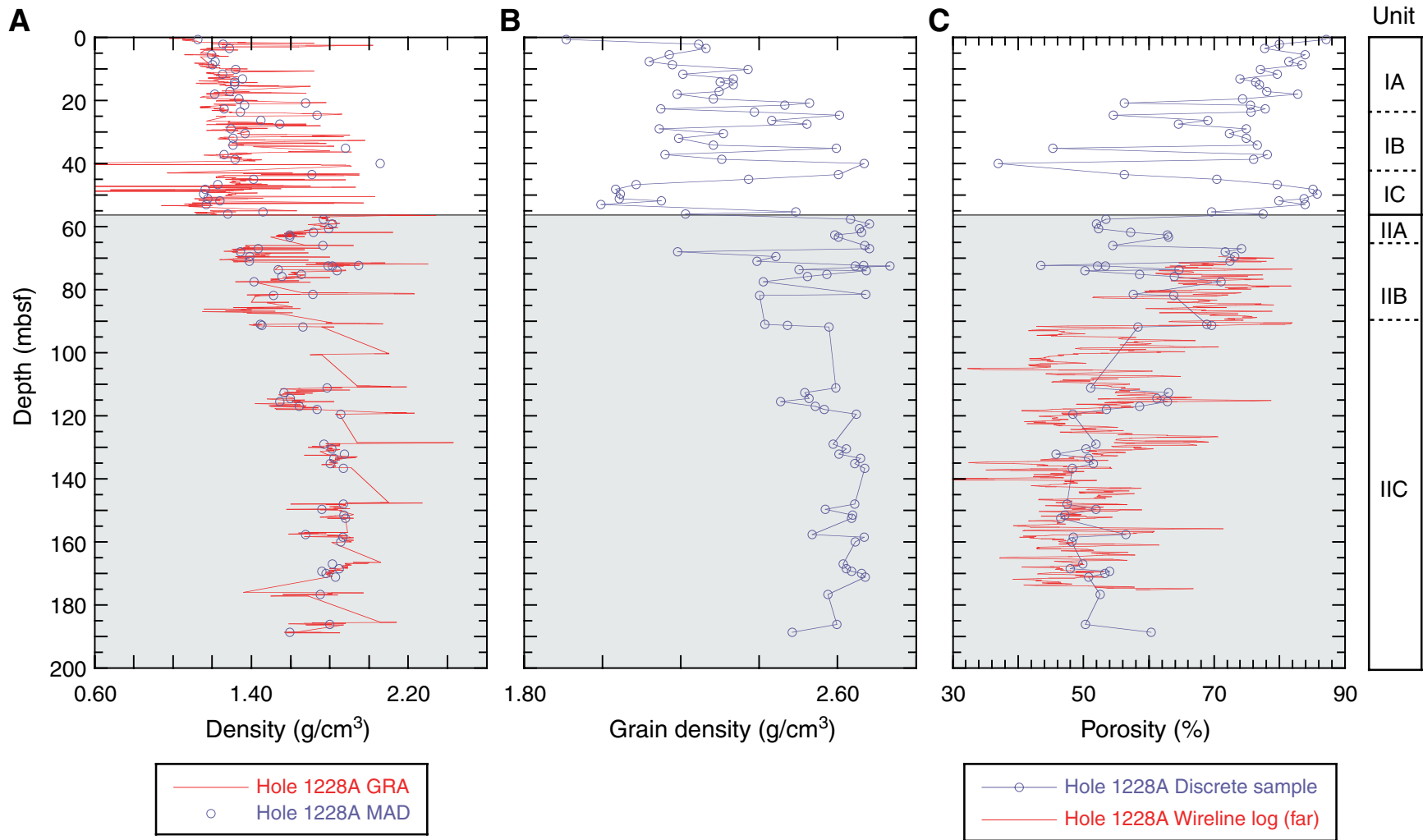


Figure F16. *P*-wave velocity profiles derived from *P*-wave logger (PWL) and PWS3 measurements for Hole 1228A and Hole 680A. Below 90 mbsf, PWL velocity peaks may be less dependable since the core liners were commonly incompletely filled or contaminated by drilling-induced gravel slurry.

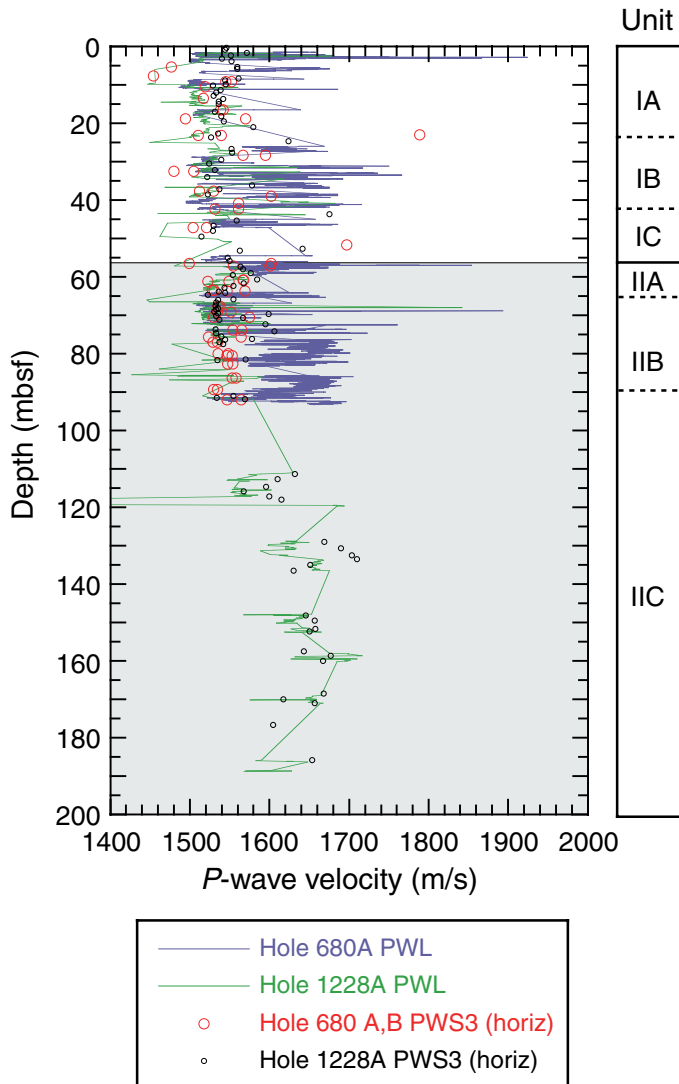


Figure F17. A. Natural gamma ray (NGR) profile from the multisensor track (MST) compared to the wireline log record for Hole 1228A. B. Expanded scale of Subunit IIC showing the gamma ray cyclotherms (labeled a–g) described in the text and the match with the partially complete MST record (1–6), across parts of these cycles.

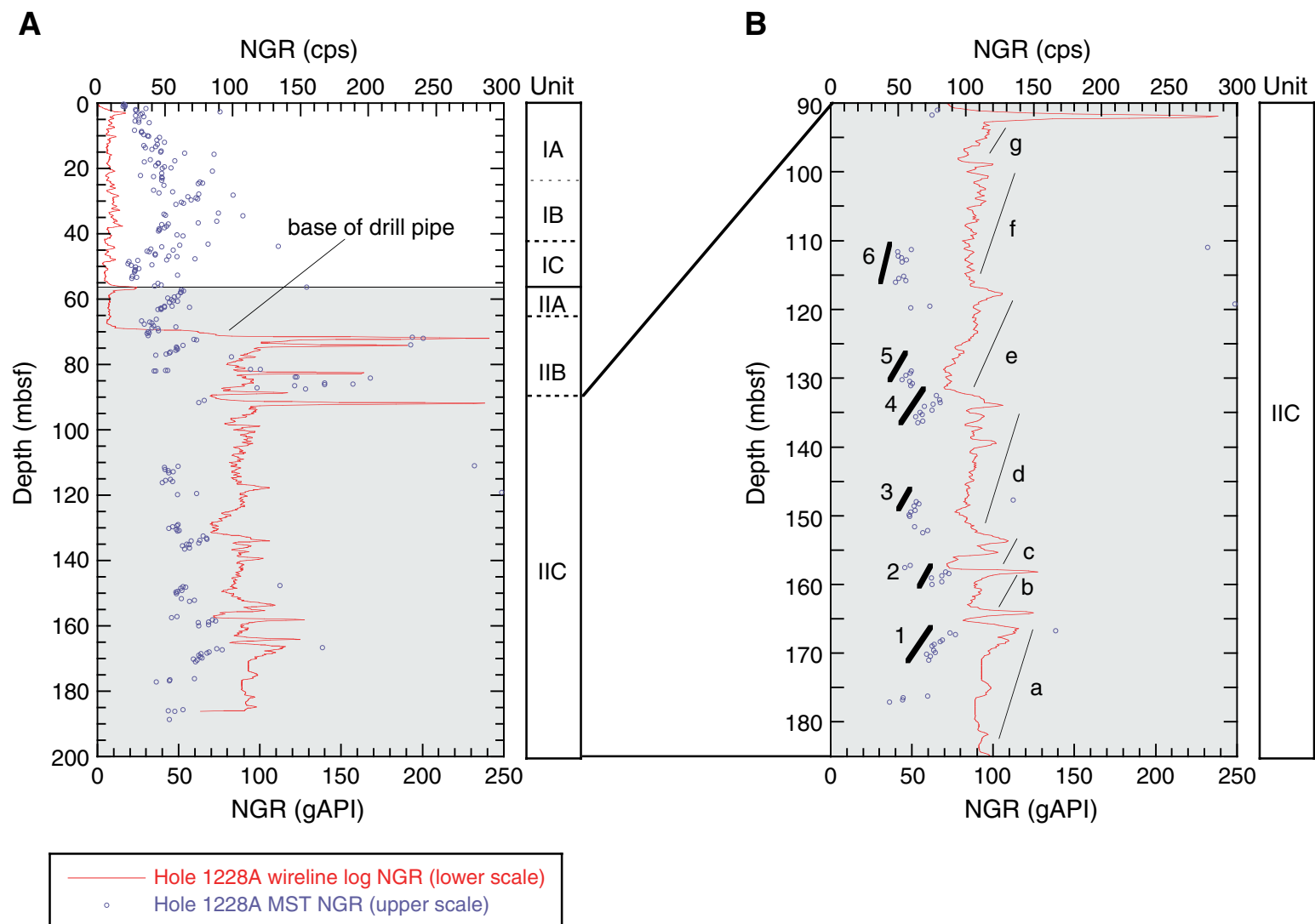


Figure F18. Thermal conductivity measurements for Hole 1228A. **A.** Thermal conductivity profile (needle probe method). Arrows mark measurements where unfilled core liner or gravel slurry are present. **B.** Mean-detrended bulk density and thermal conductivity profiles illustrate the controlling effect of water content variability on thermal properties.

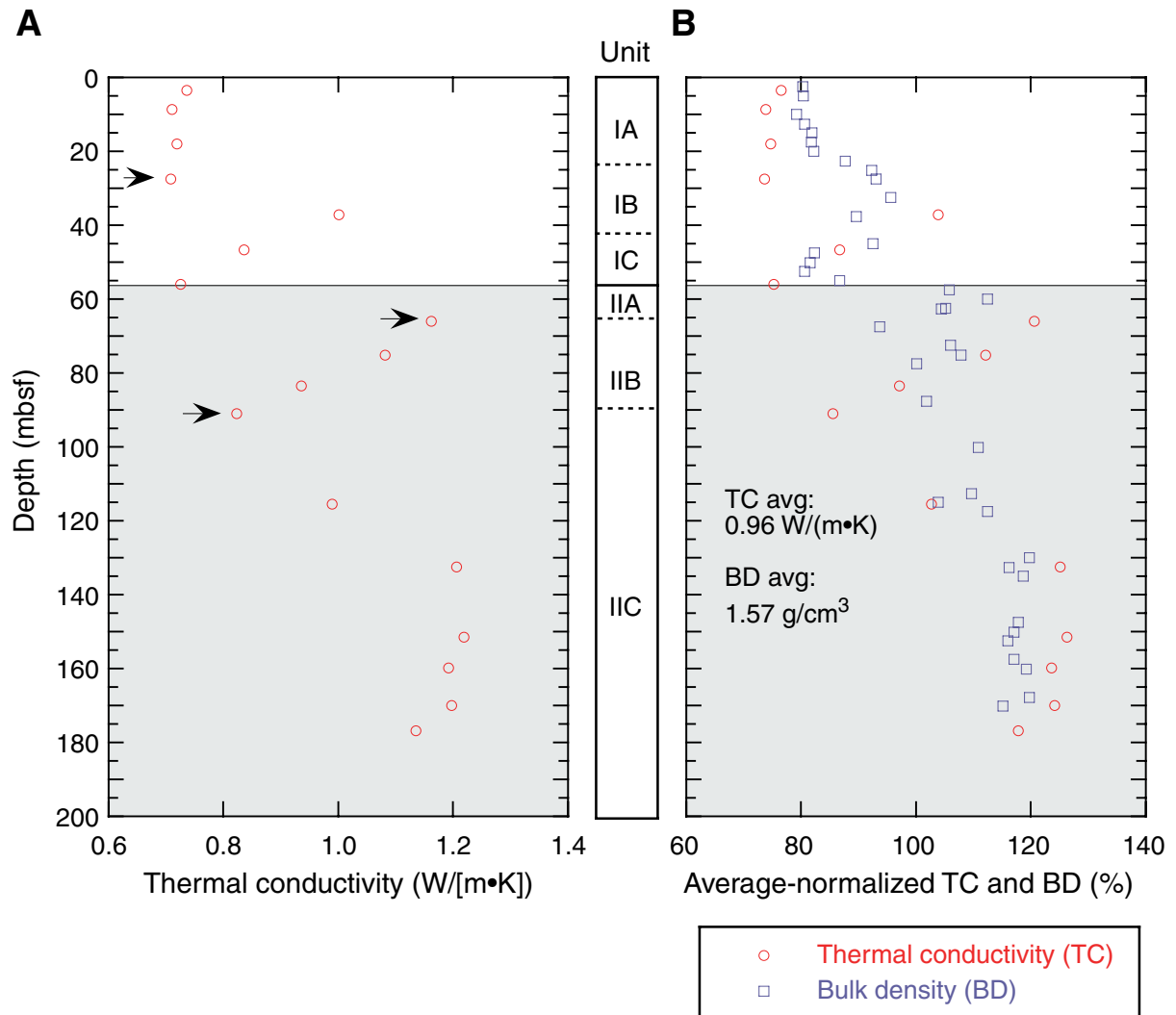


Figure F19. Formation factor profile for Site 1228A. Three lithologies are indicated by the thick lines, highlighting the identification of electrical conductivity boundaries between Subunits IA/IB, IB/IC, IC/IIA, and IIA/IIB, respectively.

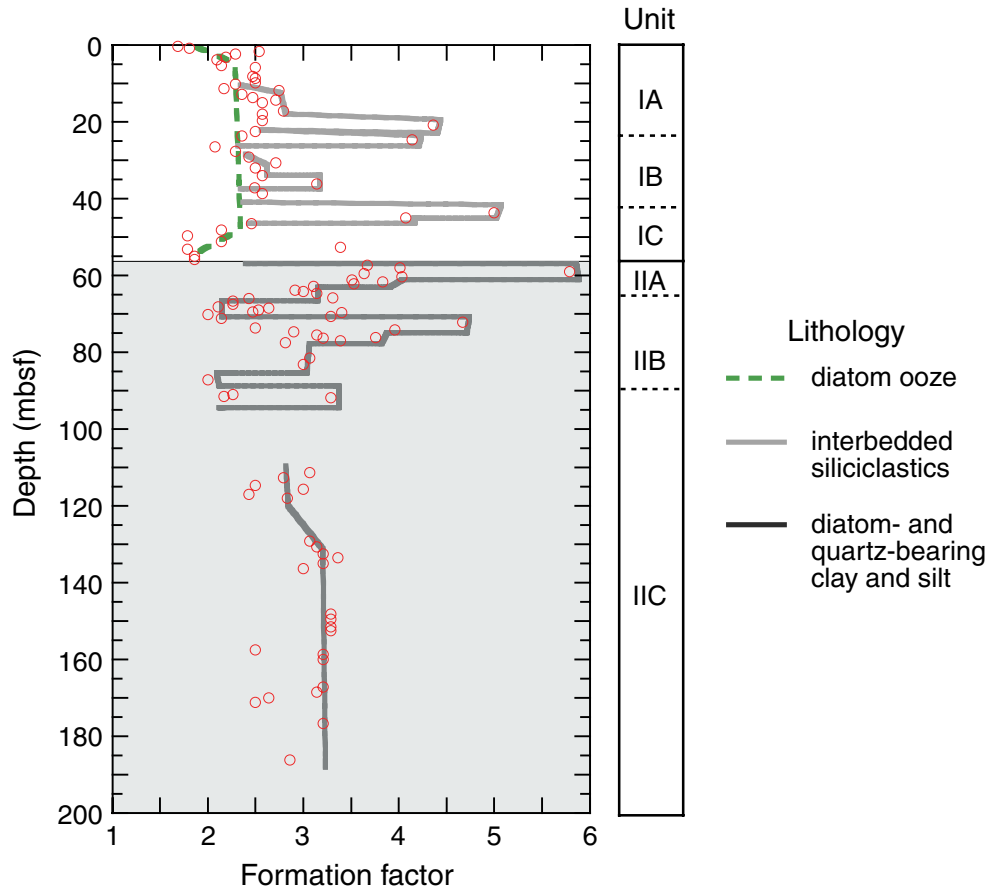


Figure F20. Temperature records from the two DVTP deployments at Site 1228 together with the extrapolated temperature. A. Record for the deployment after Core 201-1228A-9H at 80.9 mbsf. B. Records for the deployment after Core 201-1228A-22H at 194.9 mbsf.

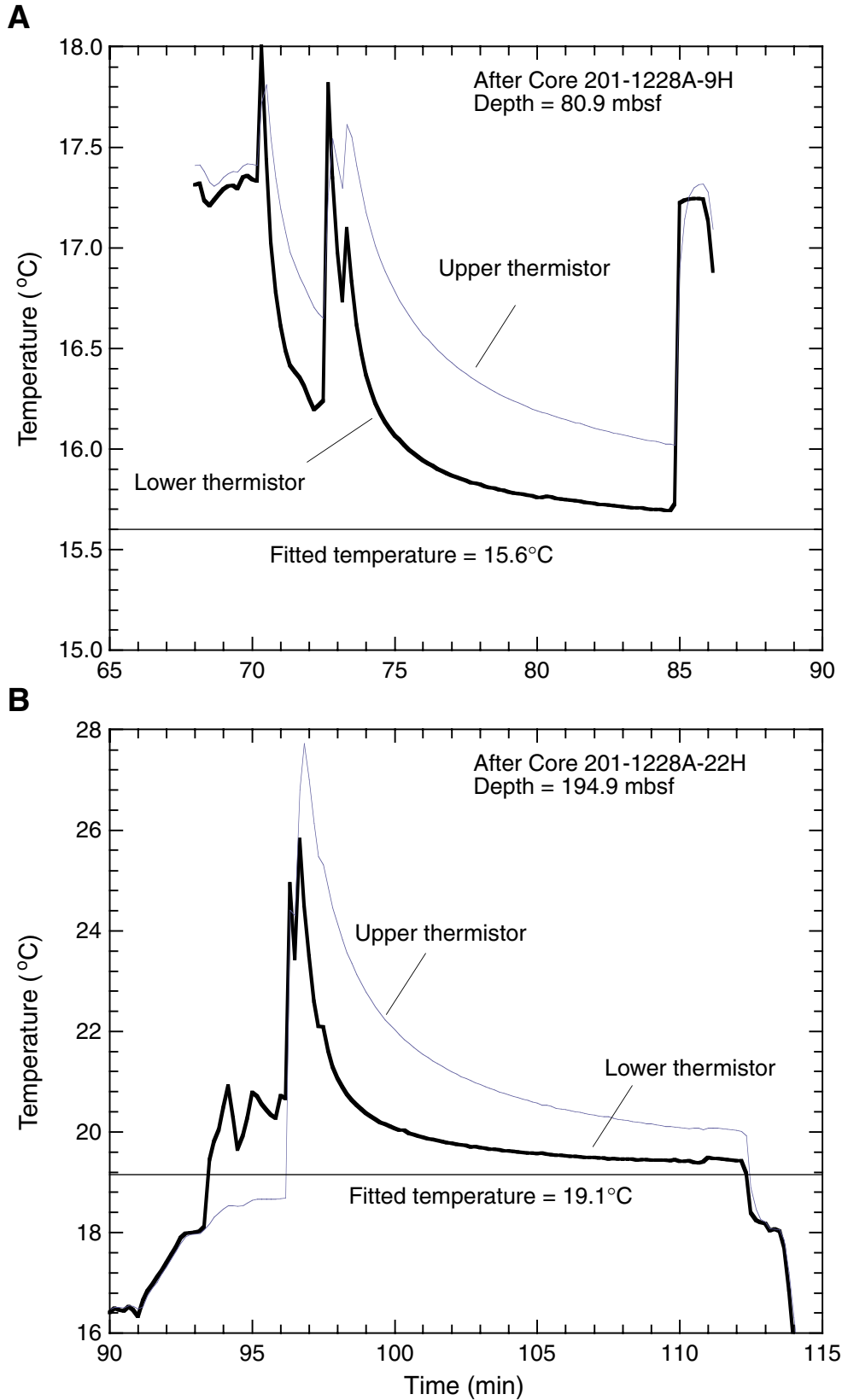


Figure F21. A. All temperatures measured in Hole 1228A together with the temperature data from Leg 112 Site 680 plotted vs. depth with a best-fit linear profile for the combined data. B. Temperature data with steady-state conductive temperature profile calculated using measured thermal conductivities from Hole 1228A and uniform heat flow.

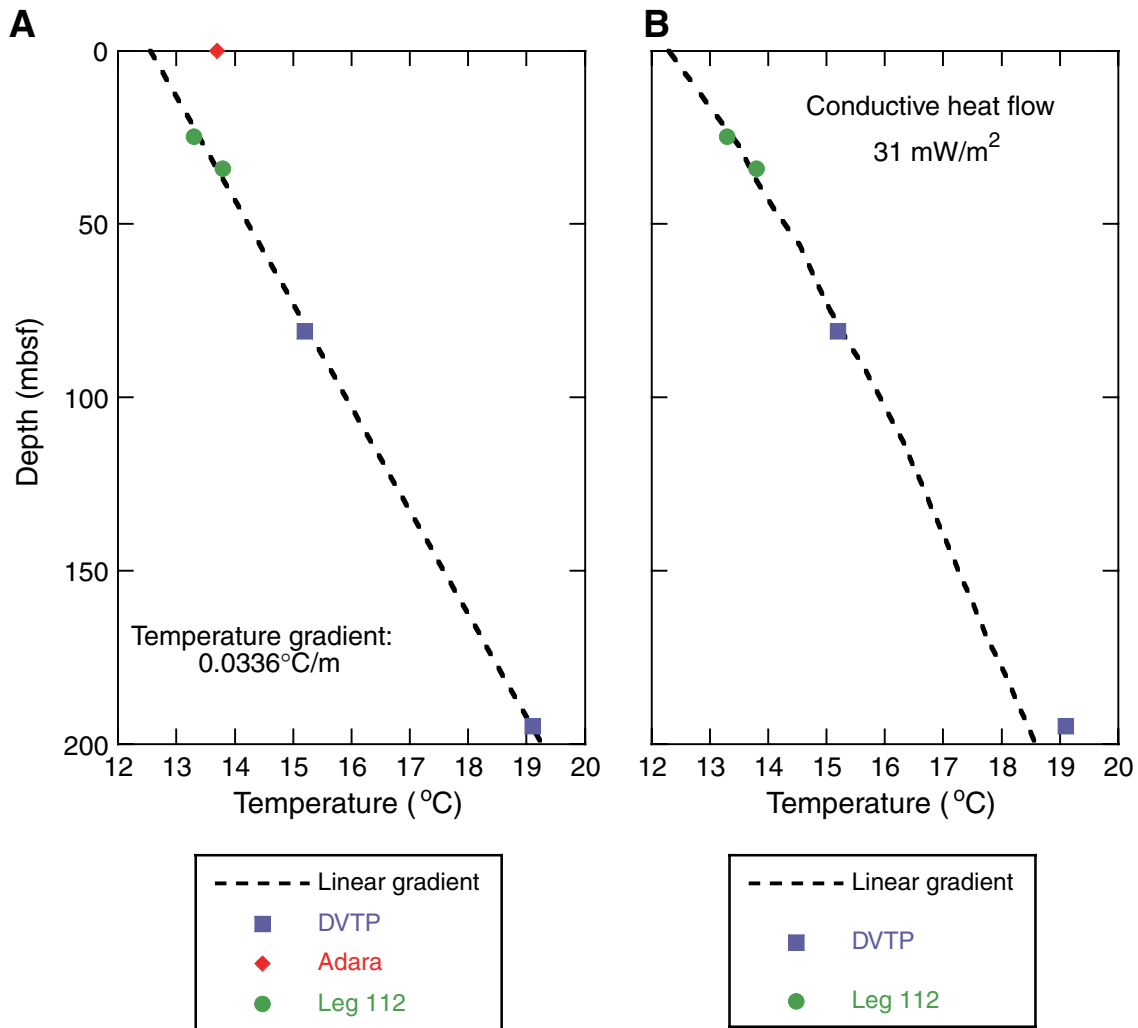


Figure F22. A. Pressure measured in Hole 1228A during the DVTP-P deployment after Core 201-1228-22H. B. Close-up of the pressure record showing the estimated measured pressure.

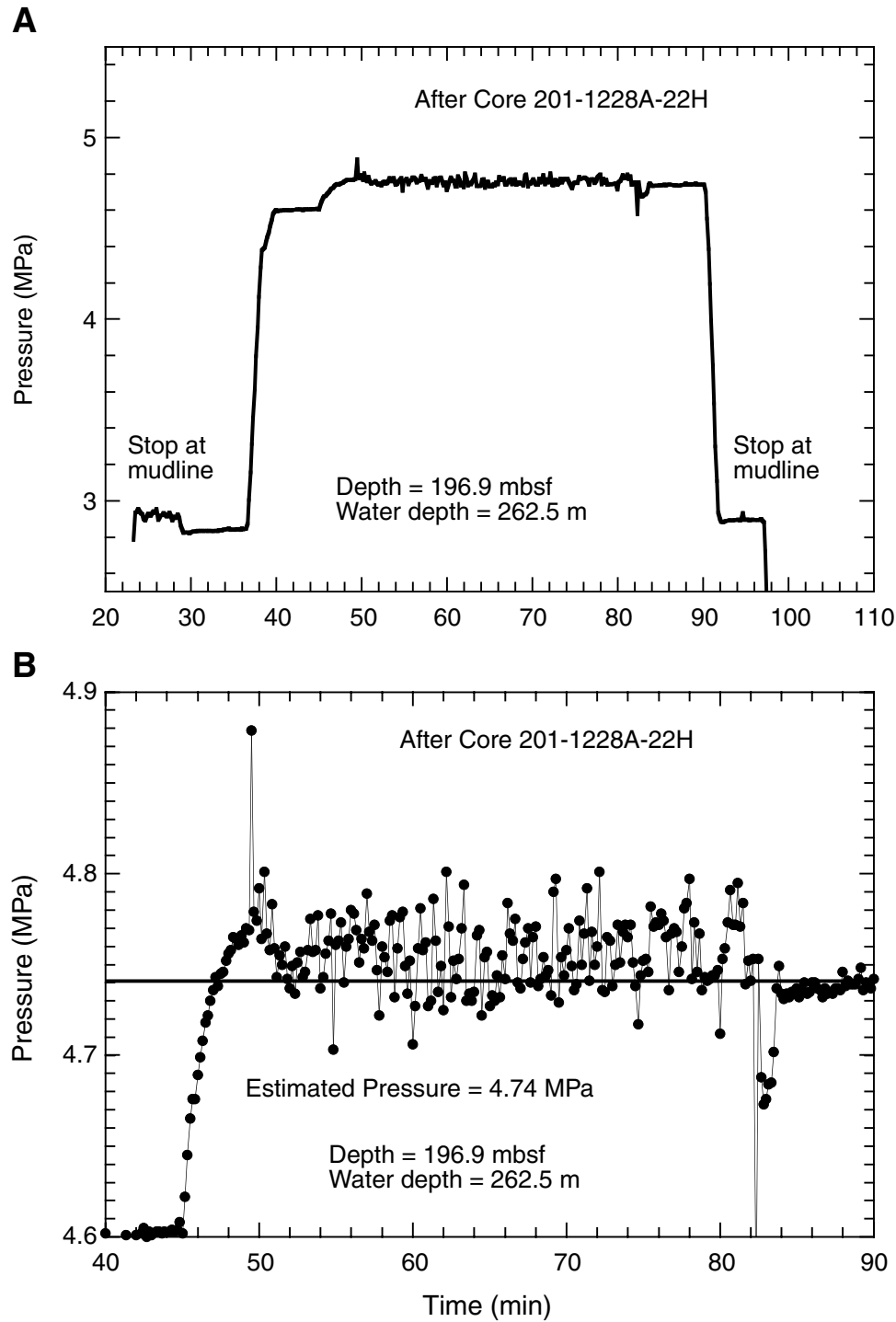


Figure F23. Main logs recorded in Hole 1228A. **A.** The hole diameter is measured by the caliper arm of the density sonde. **B.** The gamma ray log provides a measure of the natural radioactivity of the formation. **C.** Concentrations of potassium, thorium, and uranium derived from the gamma ray counts. **D.** Resistivity measured by the Phasor Dual Induction tool with three depths of investigation. **E.** Density log (red line) compared with density measurements made on core samples (shaded circles) (see “Density and Porosity,” p. 20, in “Physical Properties”). **F.** Porosity log for the two receiver spacings of the Accelerator Porosity Sonde (APS) compared with porosity measurements made on core samples (shaded circles) (see “Density and Porosity,” p. 20, in “Physical Properties”). HNGS = Hostile Environment Natural Gamma Ray Sonde, SGT = Scintillation Gamma Ray Tool.

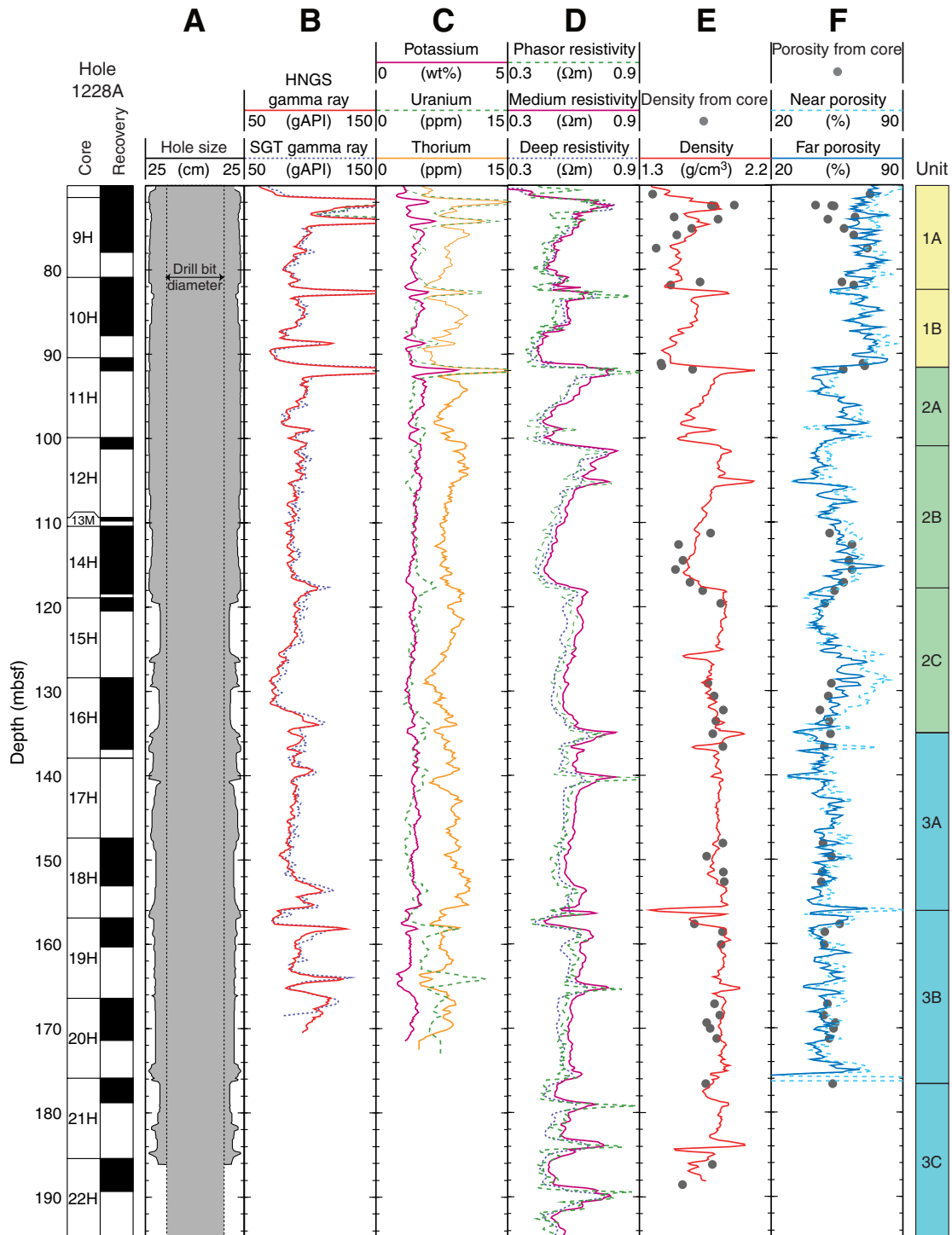


Figure F24. Comparison between data from the two passes of the triple combo tool string in Hole 1228A. A. Gamma ray. B. Resistivity. C. Density. Green dashed lines = data from the first pass, red solid lines = data from the second pass. HNGS = Hostile Environment Natural Gamma Ray Sonde.

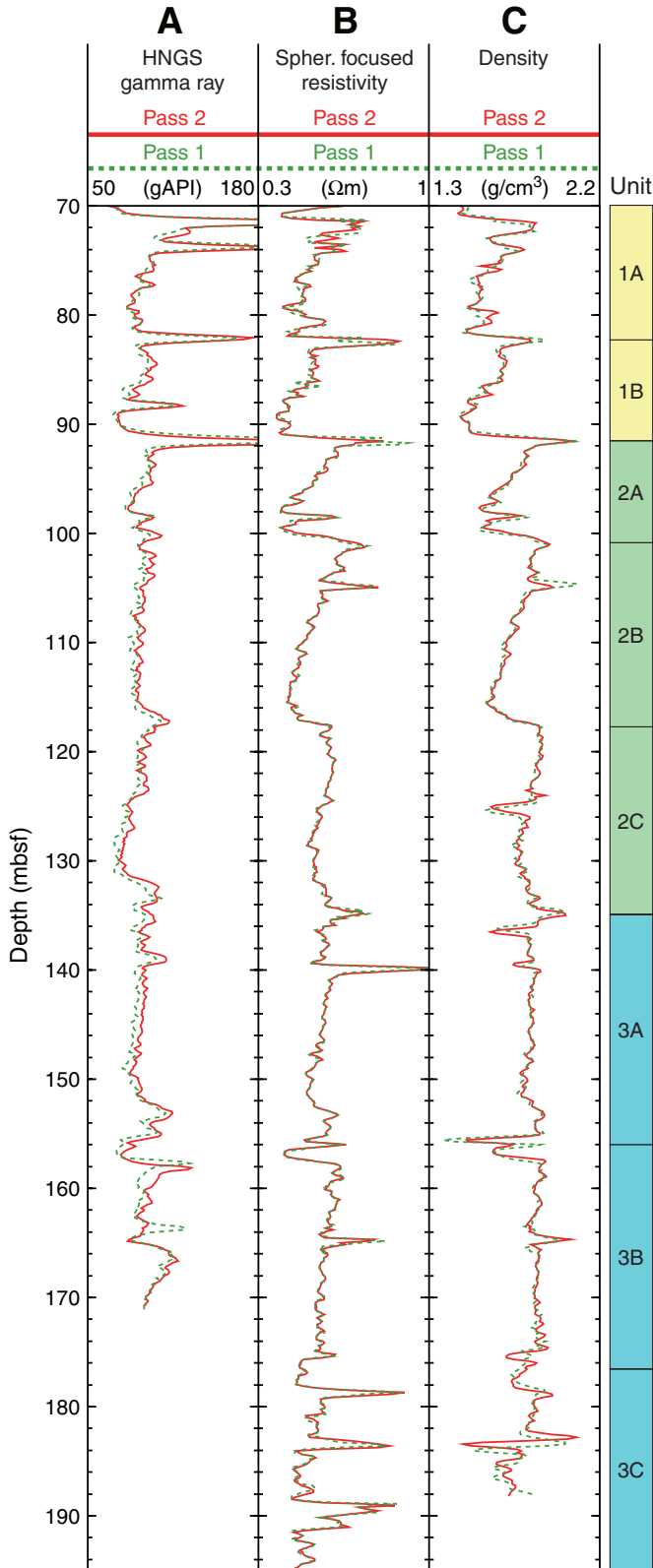


Figure F25. Temperature log recorded in Hole 1228A. Temperature data were recorded continuously during the two passes of the tool string.

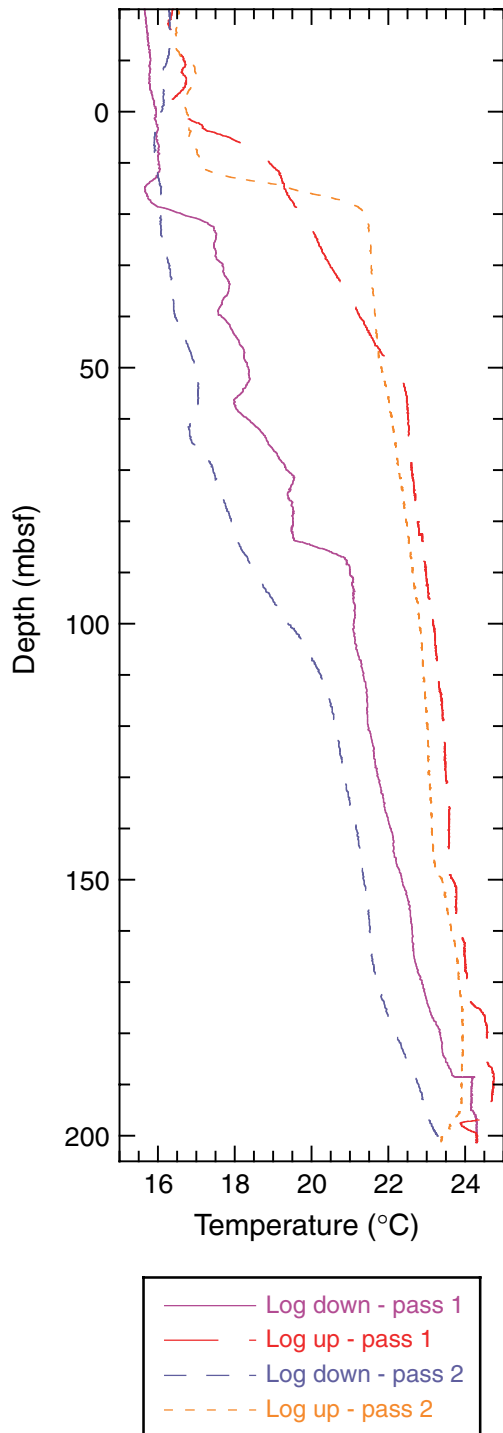


Table T1. Coring summary, Site 1228. (Continued on next page.)

Hole 1228A

Latitude: 11°3.8724'S
Longitude: 78°4.6700'W
Time on site (hr): 66.25 (1815 hr, 3 Mar–1230 hr, 6 Mar 2002)
Time on hole (hr): 54.08 (1815 hr, 3 Mar–0020 hr, 6 Mar 2002)
Seafloor (drill pipe measurement from rig floor, mbrf): 273.6
Distance between rig floor and sea level (m): 11.4
Water depth (drill pipe measurement from sea level, m): 262.2
Total depth (drill pipe measurement from rig floor, mbrf): 474.5
Total penetration (meters below seafloor, mbsf): 200.9
Total length of cored section (m): 196.9
Total length of drilled intervals (m): 4.0
Total core recovered (m): 126.35
Core recovery (%): 64.2
Total number of cores: 23
Total number of drilled intervals: 2

Hole 1228B

Latitude: 11°3.8615'S
Longitude: 78°4.6643'W
Time on hole (hr): 4.67 (0020 hr, 6 Mar–0500 hr, 6 Mar 2002)
Seafloor (drill pipe measurement from rig floor, mbrf): 273.8
Distance between rig floor and sea level (m): 11.5
Water depth (drill pipe measurement from sea level, m): 262.3
Total depth (drill pipe measurement from rig floor, mbrf): 329.1
Total penetration (meters below seafloor, mbsf): 55.3
Total length of cored section (m): 55.3
Total core recovered (m): 51.1
Core recovery (%): 92.4
Total number of cores: 7

Hole 1228C

Latitude: 11°3.8547'S
Longitude: 78°4.6657'W
Time on hole (hr): 0.75 (0500 hr, 6 Mar–0545 hr, 6 Mar 2002)
Seafloor (drill pipe measurement from rig floor, mbrf): 273.0
Distance between rig floor and sea level (m): 11.5
Water depth (drill pipe measurement from sea level, m): 261.5
Total depth (drill pipe measurement from rig floor, mbrf): 280.5
Total penetration (meters below seafloor, mbsf): 7.5
Total length of cored section (m): 7.5
Total core recovered (m): 7.53
Core recovery (%): 100.4
Total number of cores: 1

Hole 1228D

Latitude: 11°3.8511'S
Longitude: 78°4.6710'W
Time on hole (hr): 1.92 (0545 hr, 6 Mar–0740 hr, 6 Mar 2002)
Seafloor (drill pipe measurement from rig floor, mbrf): 272.9
Distance between rig floor and sea level (m): 11.4
Water depth (drill pipe measurement from sea level, m): 261.5
Total depth (drill pipe measurement from rig floor, mbrf): 299.5
Total penetration (meters below seafloor, mbsf): 26.6
Total length of cored section (m): 26.6
Total core recovered (m): 27.25
Core recovery (%): 102.4
Total number of cores: 3

Hole 1228E

Latitude: 11°3.8407'S
Longitude: 78°4.6691'W
Time on hole (hr): 4.83 (0740 hr, 6 Mar–1230 hr, 6 Mar 2002)
Seafloor (drill pipe measurement from rig floor, mbrf): 273.2
Distance between rig floor and sea level (m): 11.5
Water depth (drill pipe measurement from sea level, m): 261.7
Total depth (drill pipe measurement from rig floor, mbrf): 281.5
Total Penetration (meters below seafloor, mbsf): 8.3
Total length of cored section (m): 8.3
Total core recovered (m): 9.23
Core recovery (%): 111.2
Total number of cores: 2

Table T1 (continued).

Core	Date (Mar 2002)	Local time (hr)	Depth (mbsf)		Length (m)		Recovery (%)
			Top	Bottom	Cored	Recovered	
201-1228A-							
1H	3	2155	0.0	4.9	4.9	4.83	98.6
2H	3	2315	4.9	14.4	9.5	9.88	104.0
3H	4	0120	14.4	23.9	9.5	9.80	103.2
4H	4	0235	23.9	33.4	9.5	9.45	99.5
5H	4	0400	33.4	42.9	9.5	7.55	79.5
6H	4	0550	42.9	52.4	9.5	9.27	97.6
7H	4	0725	52.4	61.9	9.5	9.96	104.8
8H	4	0855	61.9	71.4	9.5	9.79	103.1
9H	4	1015	71.4	80.9	9.5	6.52	68.6
10H	4	1230	80.9	90.4	9.5	6.90	72.6
11H	4	1530	90.4	99.9	9.5	1.60	16.8
12H	4	1750	99.9	109.4	9.5	1.34	14.1
13M	4	1910	109.4	110.4	1.0	0.39	39.0
14H	4	2010	110.4	118.9	8.5	8.02	94.4
15H	4	2125	118.9	128.4	9.5	1.57	16.5
16H	4	2315	128.4	137.9	9.5	8.47	89.2
17H	5	0110	137.9	147.4	9.5	0.00	0.0
18H	5	0315	147.4	156.9	9.5	5.67	59.7
19H	5	0420	156.9	166.4	9.5	3.41	35.9
20H	5	0535	166.4	175.9	9.5	5.02	52.8
21H	5	0650	175.9	185.4	9.5	2.91	30.6
22H	5	0815	185.4	194.9	9.5	3.93	41.4
*****Drilled from 194.9 to 198.9 mbsf*****							
23P	5	1300	198.9	200.9	2.0	0.07	3.5
Cored totals:					196.9	126.35	64.2
Drilled total:					4.0		
Total:					200.9		
201-1228B-							
1H	6	0130	0.0	6.8	6.8	6.73	99.0
2H	6	0145	6.8	16.3	9.5	9.85	103.7
3H	6	0200	16.3	25.8	9.5	9.83	103.5
4H	6	0220	25.8	35.3	9.5	9.09	95.7
5H	6	0245	35.3	44.8	9.5	5.74	60.4
6H	6	0320	44.8	54.3	9.5	9.44	99.4
7M	6	0415	54.3	55.3	1.0	0.42	42.0
Cored totals:					55.3	51.10	92.4
201-1228C-							
1H	6	0530	0.0	7.5	7.5	7.53	100.4
Cored totals:					7.5	7.53	100.4
201-1228D-							
1H	6	0620	0.0	7.6	7.6	7.61	100.1
2H	6	0645	7.6	17.1	9.5	9.87	103.9
3H	6	0720	17.1	26.6	9.5	9.77	102.8
Cored totals:					26.6	27.25	102.4
201-1228E-							
1H	6	0950	0.0	7.3	7.3	7.33	100.4
2M	6	1035	7.3	8.3	1.0	1.90	190.0
Cored totals:					8.3	9.23	111.2

Table T2. Concentrations of dissolved species in interstitial water, Holes 1228A, 1228B, 1228C, and 1228E. (See table notes. Continued on next page.)

Core, section, interval (cm)	Depth (mbsf)	pH	Alk (mM)	Cl ⁻ (mM)	SO ₄ ²⁻ (mM)	H ₄ SiO ₄ (μM)	PO ₄ ³⁻ (μM)	NH ₄ ⁺ (μM)	Fe (μM)	Mn (μM)	Sr (μM)	Li (μM)	Ba (μM)	ΣH ₂ S (mM)	DIC (mM)	Acetate (μM)	Formate (μM)
201-1228A-																	
1H-1, 126-141	1.26	7.39		552.2	17.78		43.4	2400	1.2	0.1	90	29	1.1	2.94	17.23	1.7	1.0
1H-2, 135-150	2.76	7.21	16.4	554.5	16.88		11.8	2400	0.9	0.0	88	33	0.6	3.45	16.52		
1H-3, 135-150	4.26	7.18		550.9	16.43		6.1		0.5	0.0	90	37	0.6	3.70	15.49	1.2	1.3
2H-1, 135-150	6.25	7.14	16.2	553.7	15.77	1017	8.9		0.2	0.0	96	41	0.4	4.14	16.11		
2H-3, 0-15	7.90	7.23	16.2	559.7	14.35	940	9.7	2300	0.3	0.0	98	45	0.4	4.67	15.92		
2H-3, 135-150	9.25	7.15	16.6				7.8	2300	0.2	0.0	104	49	0.5	4.35	16.49	0.8	0.5
2H-5, 135-150	12.25	7.15	17.5	569.1	12.78		8.8	2400	0.4	0.0	111	54	0.4	4.62	17.03		
3H-1, 135-150	15.75	7.07	17.5	574.0	10.35		6.9	2700	0.2	0.0	121	66	0.6	5.23	17.65		
3H-3, 135-150	18.75			587.3	8.22		6.7	3000	0.4	0.0	128	73	0.7	5.65			
3H-5, 135-150	21.75	7.12	19.0	589.9	6.51		7.0	3100	1.3	0.1	133	79	0.9	5.48	19.35		1.3
4H-1, 135-150	25.25	7.19	19.4	589.7	4.96		5.9	2300	0.8	0.1	146	94	1.4	6.12	19.81		
4H-3, 135-150	28.25	7.07	19.1	598.1	3.84	990	6.4	3600	0.3	0.0	150	100	1.9	6.39		1.1	0.8
4H-5, 135-150	31.25	7.05	19.4	624.2	3.37		6.3	3700	0.2	0.1	159	110	2.1		19.78		
5H-1, 135-150	34.75	7.21	18.0	624.9	2.59		4.6	4300	0.7	0.0	160	123	1.8	4.78	18.88		
5H-3, 135-150	37.75	6.99	18.0	625.2	2.50		5.1	3900	0.5	0.1	164	126	1.7	5.95	18.73	1.1	1.2
5H-4, 135-150	39.25	7.04	17.2	628.7	2.60		4.5	4100	0.3	0.0	164	130	1.7	5.42	17.59		
6H-1, 135-150	44.25	7.06	16.2	633.4	2.97	972	2.5	3900	0.4	0.0	175	147	1.4	5.20	16.80		
6H-3, 135-150	47.25	7.01	16.4	653.5	3.06	1117	3.8	4100	0.2	0.2	181	155	1.5	5.46	16.86	1.2	1.0
7H-1, 135-150	53.75	7.02	14.3	655.9	3.85		4.0	4200	0.4	0.1	187	166	1.1	4.60	15.03		
7H-3, 135-150	56.75			674.8	4.12		2.9	4300	0.2	0.1	187	183	1.1	4.48	15.48	0.7	0.7
7H-5, 135-150	59.75			692.4	5.04	1005	2.5	4200	1.5	0.4	195	189	0.9	3.01	14.21		
8H-1, 135-150	63.25	7.06	12.7	707.3	5.89	985	3.4	3900	0.3	0.3	204	201	0.8	3.65	13.13		
8H-3, 135-150	66.25	7.20	11.5	727.7	6.65	995	2.1		1.9	0.4	210	210	0.8	2.91	12.48		0.9
8H-5, 135-150	69.25	7.16	10.8	737.7	7.22	1010		4300	0.3	0.3	215	217	0.7	3.27	11.23		
9H-1, 135-150	72.75	6.83	10.3	732.3	7.78	908	6.0	4300	0.6	0.3	223	225	0.6	2.96	11.28		
9H-3, 135-150	75.75	6.78	9.4	740.5	8.61	955	4.1	4300	1.1	0.5	225	235	0.7	2.11	9.56	0.9	1.1
10H-1, 135-150	82.25	6.94	8.9	758.4	10.09		2.5	4400	0.5	0.5	236	248	0.6		9.38		
10H-3, 135-150	85.25													2.14			
10H-4, 135-150	86.75	6.91	8.9	778.1	10.29		2.7	4300							9.34	0.8	0.5
11H-1, 85-100	91.25	6.90	7.4	794.8	12.35		3.0	4300	1.0	1.0	254	269	0.6	0.94	8.07		0.9
12H-1, 88-110	100.78	6.97	6.2	830.6	14.58		3.4	4300	1.5	1.2	269	280	0.7	1.26	6.82	1.7	1.8
14H-1, 135-150	111.75			824.8	16.27		4.0	4400	1.2	1.8	288	303	0.5	0.73	5.51		0.3
14H-3, 135-150	114.75	6.52	5.2	851.3	17.41	1024	3.3	4400	3.1	2.0	293	304	0.6	0.51	5.43		
14H-5, 135-150	117.75	6.80	5.2	879.6	18.34	1006		4400	6.9	2.2	302	314	0.7	0.29	5.18		
16H-1, 135-150	129.75	6.86	4.4	876.9	19.87	856	2.6	4500	6.9	3.4	319	325	0.7	0.13	4.88		
16H-3, 135-150	132.75	6.80	4.4	926.6	21.4		2.6	4600	14.1	2.9	325	332	0.5	0.0057	4.68	1.3	1.1
18H-1, 135-150	148.75	7.11	4.3	953.9	23.9		1.3	4800	11.1	5.3	349	349	0.6		4.33		
18H-2, 135-150	150.25	7.14	4.3	962.6	24.3			4800	2.1	5.4	356	351	1.2		4.18		
18H-3, 135-150	151.75			967.4	24.6	993		4700	17.3	5.7	350	355	0.6	0.0028	4.08	2.2	1.7
19H-1, 79-94	157.69	7.03	3.8	993.4	26.4	991	1.5	4800	12.8	6.7	367	364	0.6	0.00051	4.36		
19H-2, 135-150	159.19	7.07	4.3	979.7	26.4	1056	1.5	5000	6.7	6.6	370	372	0.8		4.31	1.9	1.8
20H-1, 120-135	167.60	7.40	4.0	1009.9	27.6		1.8	5000	0.5	7.3	380	379	0.7	<0.00017	3.76		
20H-3, 135-150	170.60	6.90	3.8	1024.9	28.2		2.5	4900	39.2	8.0	380	381	0.6		4.37		
21H-1, 135-150	177.25	6.94	3.8	1029.0	28.8		1.6	5000	39.9	8.3	380	380	0.8	0.0018	4.24	1.1	1.2
22H-1, 120-135	186.60	6.95	3.7	1061.3	30.9		2.0	5100	5.5	7.8	392	402	0.6		4.17		
22H-1, 135-150	186.75	7.04	3.8					5200	11.6	8.2	395	396	0.6	0.00	4.13	2.2	1.6
22H-3, 60-77	189.00	6.88	3.7	1059.5	31.1			5100	42.9	8.4	394	406	0.7	0.02	4.08		

Table T2 (continued).

Core, section, interval (cm)	Depth (mbsf)	pH	Alk (mM)	Cl ⁻ (mM)	SO ₄ ²⁻ (mM)	H ₄ SiO ₄ (μM)	PO ₄ ³⁻ (μM)	NH ₄ ⁺ (μM)	Fe (μM)	Mn (μM)	Sr (μM)	Li (μM)	Ba (μM)	ΣH ₂ S (mM)	DIC (mM)	Acetate (μM)	Formate (μM)
201-1228B-																	
6H-1, 130-150	46.10	6.98	15.5				4.0		0.5	0.1	172	152	1.4	5.03			
6H-4, 130-150	50.60	7.13	14.6				4.5		0.4	0.1	183	165	1.1	5.01	15.47		
201-1228C-																	
1H-1, 15-30	0.15				22.2	860		1750	1.3	0.0	87	26	0.3	1.17			
1H-1, 30-45	0.30	7.60	13.6		20.9	826	43.0	1860	2.0	0.0	87	25	0.4	1.65	13.48		
1H-1, 45-60	0.45	7.62	15.1		20.2	897	44.5	2060	0.8	0.0	89	27	0.3	2.27	14.92		
1H-1, 60-75	0.60	7.65	16.0		19.46	889		2120	0.4	0.0	88	26	0.3	2.54	15.81		
1H-1, 75-90	0.75	7.75	17.1		18.33	913	44.2	2170	0.6	0.0	86	26	0.4	2.91	16.93		
1H-1, 90-105	0.90	7.78	18.0		17.72	878	42.2	2300	0.5	0.1	84	26	0.4		17.05		
1H-1, 105-120	1.05	7.75	18.4		17.60	900		2330	0.6	0.0	84	26	0.3	3.37	18.00		
1H-1, 120-135	1.20	7.75	18.4		17.68	859	43.8	2340	4.4	0.1	83	26	0.4	2.47			
1H-1, 135-150	1.35	7.77	18.8		17.19	854	36.2	2380	0.8	0.0	84	26	0.4	3.33			
201-1228E-																	
1H-1, 0-1	0.00			569.1	29.1	20									9.00		
1H-1, 0-12	0.00			567.9	25.1	196			1.5	0.0	87	25	0.2	0.21	10.87		
1H-1, 12-25	0.12	7.76	10.8	556.6	23.4		47.7	100	1.0	0.0	88	26	0.3	0.66	11.95		
1H-1, 25-40	0.25	7.70	12.1	576.1	17.00	873	47.5	1630	0.7	0.0	88	26	0.3	1.11	17.35		
1H-1, 40-55	0.40			566.7	21.8			1810	0.7	0.0	86	26	0.3		17.76		
1H-1, 100-115	1.00	7.76	17.9	549.3	17.88	933	48.3	2270	0.2	0.0	85	26	0.3	3.19	18.46		
1H-2, 0-15	2.00	7.77	18.5	571.6	17.74	876	27.9	2510	0.3	0.1	84	29	0.3	3.81	18.71		
1H-2, 90-105	2.90	7.73	16.7	570.3	17.22	832		2350	0.3	0.1	85	31	0.3	3.87	16.82		
1H-3, 0-15	3.50	7.61	15.9	577.7	17.38	825		2310	0.4	0.1	83	33	0.3	3.74	16.30		
1H-3, 100-115	4.50	7.60	15.4	564.6	16.95	859	4.6	2160	0.8	0.1	87	36	0.3	3.66	16.01		
1H-4, 135-150	6.35	7.62	15.8	584.1	16.75		5.6		0.7	0.2	93	40	0.4	3.41	16.18		

Notes: Alk = alkalinity, DIC = dissolved organic carbon. This table is also available in [ASCII](#).

Table T3. Hydrocarbon gas concentrations in headspace, Holes 1228A and 1228B. (See table notes. Continued on next page.)

Core, section, interval (cm)	Depth (mbsf)	Methane (ppm in headspace)			Methane (μM)	Ethane (ppm in headspace)			Ethane (μM)
		20 min @ 60°C	24 hr @ 22°C	1 week @ 22°C		20 min @ 60°C	24 hr @ 22°C	1 week @ 22°C	
201-1228A-									
1H-1, 121-126	1.21		11.5		1.97				
1H-2, 130-135	2.71		7.8		1.35				
1H-3, 130-135	4.21	11.1			*				
2H-1, 130-135	6.20		12.6		2.18				
2H-2, 145-150	7.85		15.2		2.65				
2H-3, 130-135	9.20	9.6			*				
2H-5, 130-135	12.20		14.8		2.69				
2H-6, 145-150	13.85	11.6			*				
3H-1, 130-135	15.70		22.7		4.12				
3H-3, 0-5	17.40		28.5		5.29				
3H-3, 130-135	18.70	24.6			*				
3H-5, 0-5	20.40		23.7		4.40				
3H-5, 130-135	21.70		42.4		8.10				
3H-6, 0-5	21.90	22.1			*				
4H-1, 130-135	25.20		15.0		3.70		1.15		0.22
4H-3, 0-5	26.90		37.4		7.66				
4H-3, 130-135	28.20	14.7			*				
4H-4, 0-5	28.40		33.2		6.80				
4H4, 145-150	29.85	21.5			*				
4H-6, 0-5	31.40		19.8		4.05				
4H-7, 0-5	32.90	24.2			*	0.58			*
5H-1, 130-135	34.70		44.5		8.39				
5H-3, 0-5	36.40		26.5		6.32		1.11		0.21
5H-3, 130-135	37.70	22.9			*	0.64			*
5H-4, 0-5	37.90		31.2		5.87				
5H-4, 145-150	39.35	20.7			*				
6H-1, 130-135	44.20		38.2		6.43		0.61		0.11
6H-2, 0-5	44.40	23.4			*	0.55			*
6H-4, 0-5	47.40		28.3		5.80		1.31		0.22
6H-5, 0-5	48.90	29.0			*	0.56			*
7H-1, 130-135	53.70		22.7		4.17				
7H-3, 0-5	55.40	17.8			*				
7H-4, 0-5	56.90		17.0		4.59		1.01		0.19
7H-5, 0-5	58.40	12.3			*				
8H-2, 0-5	63.40		18.8		4.35				
8H-4, 0-5	66.40	11.8			*				
8H-5, 0-5	67.90		22.5		4.42				
8H-6, 0-5	69.40	14.4			*				
9H-2, 0-5	72.90		14.6		3.74				
9H-4, 0-5	75.90	11.9			*				
9H-4, 145-150	77.35		16.6		3.29				
10H-1, 130-135	82.20		21.5		4.27				
10H-4, 0-5	85.40		13.8		2.75		0.81		0.16
11H-1, 80-85	91.20		21.3		5.36				
11H-2, 0-5	91.40	5.6			*				
14H-1, 130-135	111.70		8.2		2.18		0.54		0.14
14H-2, 145-150	113.35	2.8			*				
14H-5, 130-135	117.70		8.0		2.20				
15H-1, 141-146	120.31	1.7			*				
16H-1, 130-135	129.70		6.5		1.87				
16H-2, 145-150	131.35	1.0			*				
16H-4, 0-5	132.90		7.9		2.27				
18H-1, 130-135	148.70		9.7		2.83				
18H-2, 145-150	150.35	2.1			*				
18H-4, 0-5	151.90		7.3		2.13				
19H-1, 74-79	157.64	2.2			*				
19H-1, 74-79	157.64		4.5		1.30				
20H-1, 115-120	167.55	1.8			*				
20H-3, 0-5	169.25		3.9		1.11				
21H-1, 135-150	177.25		5.4		1.46				
22H-1, 115-120	186.55		5.9		1.59				
22H-3, 55-60	188.95		7.7		2.08				
201-1228C-									
1H-1, 30-45	0.30			11.3	1.90			0.2	0.03

Table T3 (continued).

Core, section, interval (cm)	Depth (mbsf)	Methane (ppm in headspace)			Methane (μ M)	Ethane (ppm in headspace)			Ethane (μ M)
		20 min @ 60°C	24 hr @ 22°C	1 week @ 22°C		20 min @ 60°C	24 hr @ 22°C	1 week @ 22°C	
1H-1, 45-60	0.45			13.4	2.26				
1H-1, 60-75	0.60			11.9	2.01				
1H-1, 75-90	0.75			14.3	2.44				
1H-1, 90-105	0.90			19.2	3.27			0.32	0.05
1H-1, 105-120	1.05			18.9	3.24				
1H-1, 120-135	1.20			14.0	2.40				
1H-1, 135-150	1.35			16.3	2.80			0.38	0.07

Notes: * = concentrations were not calculated from samples processed according to the safety protocol due to systematically lower yield compared to longer extractions. This table is also available in [ASCII](#).

Table T4. Hydrogen concentrations, Holes 1228A and 1228E.

Core, section, interval (cm)	Depth (mbsf)	H ₂ (nM)	Incubation temperature (°C)
201-1228A-			
2H-2, 114–120	7.54	0.30	11
2H-5, 11–16	11.01	0.24	11
3H-2, 99–105	16.89	0.24	11
4H-2, 75–81	26.15	0.21	11
5H-2, 60–66	35.50	0.25	11
7H-2, 70–76	54.60	0.35	11
8H-3, 65–71	65.55	0.28	
9H-2, 55–61	73.45	0.25	
10H-2, 75–81	83.15	0.95	
14H-3, 78–84	114.18	0.37	
16H-3, 60–66	132.00	0.17	
18H-3, 50–56	150.90	0.35	
21H-2, 82–88	178.22	0.19	
22H-2, 108–114	187.98	0.25	
201-1228E-			
1H-1, 168–174	1.68	0.16	
1H-2, 20–26	2.20	0.13	
1H-3, 76–82	4.26	0.49	
1H-4, 60–66	5.60	0.16	

Note: This table is also available in [ASCII](#).

Table T5. Level of seawater contamination expected in cores based on the concentration of PFT observed in sediment, Holes 1228A and 1228E.

Core, section	Sample details	ng PFT/ g sediment	Potential μ L seawater/ g sediment
201-1228A-			
2H-2	Center	0.01	0.01
2H-2	Outside	0.56	0.56
5H-5	Center	BD	BD
5H-5	Outside	0.02	0.02
10H-2	Center	BD	BD
10H-2	Outside	0.22	0.22
14H-3	Center	0.01	0.01
14H-3	Outside	0.02	0.02
15H-1	Center	0.02	0.02
15H-1	Outside	0.07	0.07
15H-1	Wet subcore	0.06	0.06
22H-2	Wet subcore	0.08	0.08
22H-2	Dry subcore	0.11	0.11
201-1228E-			
1H-3	Center	0.01	0.01
1H-3	Outside	0.09	0.09

Notes: Detection limit = 0.01 μ L seawater/g sediment, BD = below detection. The potential for prokaryotic cell contamination is based on 5×10^8 cells/L surface seawater. This may be viewed as an upper limit for prokaryotic cell contamination because it requires the sediment be porous enough to allow all of the contaminating cells to travel with the PFT.

Table T6. Potential contamination of slurries based on PFT, Holes 1228A and 1228E.

Core, section	ng PFT/ mL slurry	Potential μ L seawater/ mL slurry
201-1228A-		
2H	BD	BD
5H	0.03	0.03
14H	0.03	0.03
201-1228E-		
1H	0.03	0.03

Notes: Detection limit = 0.025 μ L seawater/mL slurry, BD = below detection.

Table T7. Potential contamination of laboratory slurries obtained using fluorescent microspheres (0.5 μm diameter) as prokaryotic cell mimics, Hole 1228A and 1228E.

Core, section, interval (cm)	Sample type	Beads/fov	Beads/mL sediment	Delivery confirmed
201-1228A-				
2H-2, 50-64	Slurry	0/58	0	Yes
5H-5, 5-17	Slurry	1/63	56	Yes
14H-3, 35-49	Slurry	0/50	0	Yes
201-1228E-				
1H-1, 115-129	Slurry	1/83	42	Yes

Note: fov = fields of view under the microscope, each approximating an area of 22,800 μm^2 .

Table T8. Media inoculated with sample material from different depths, Holes 1228A and 1228E.

Hole:	201-1228A-					201-1228E-
Core:	2H	5H	7H	14H	22H	1H
Depth (mbsf):	7	40	53	114	186	1
Medium:						
Sed	15°C: MPN	15°C: MPN		15°C: MPN		15°C: MPN
Mono	15°C: MPN	15°C: MPN		15°C: MPN		15°C: MPN
Poly	15°C: MPN	15°C: MPN		15°C: MPN		15°C: MPN
Aro	15°C: MPN	15°C: MPN		15°C: MPN		15°C: MPN
Rad	15°C: MPN	15°C: MPN		15°C: MPN		15°C: MPN
Grad	15°C: EN	15°C: EN		15°C: EN		15°C: EN
FERM-Glyc: 8.0	60°C: EN	60°C: EN			60°C: EN	60°C: EN
FERM-Glyc: 8.8	60°C: EN	60°C: EN			60°C: EN	60°C: EN
FERM-Xyl: 8.0	60°C: EN	60°C: EN			60°C: EN	60°C: EN
FERM-Syl: 8.8	60°C: EN	60°C: EN			60°C: EN	60°C: EN
SRB: 8.0	60°C: EN	60°C: EN			60°C: EN	60°C: EN
SRB: 8.6	60°C: EN	60°C: EN			60°C: EN	60°C: EN
SRB benz: 8.0						60°C: EN
H ₂ /HCO ₃ ⁻ /FeIII: 7.9	60°C: EN	60°C: EN	60°C: EN		60°C: EN	60°C: EN
H ₂ /HCO ₃ ⁻ /FeIII: 8.5	60°C: EN	60°C: EN			60°C: EN	60°C: EN
H ₂ /HCO ₃ ⁻ /MnIV: 7.8		60°C: EN	60°C: EN			60°C: EN
H ₂ /HCO ₃ ⁻ : 7.8	60°C: EN	60°C: EN			60°C: EN	60°C: EN
H ₂ /HCO ₃ ⁻ : 8.8						
C-18-lipo: 7.8	60°C: EN	60°C: EN			60°C: EN	60°C: EN
C-18-lipo: 9.0	60°C: EN	60°C: EN			60°C: EN	60°C: EN
Chlor: 7.8		60°C: EN				60°C: EN
201-1	RT, 50°C, 80°C: EN					
201-2	RT, 50°C, 80°C: EN					
201-3	RT, 50°C, 80°C: EN					
201-4	RT, 50°C, 80°C: EN					
201-5	RT, 50°C, 80°C: EN					
201-6	RT, 50°C, 80°C: EN					
201-7	RT, 50°C, 80°C: EN					
201-8	RT, 50°C, 80°C: EN					
201-9	RT, 50°C, 80°C: EN					
201-10	RT, 50°C, 80°C: EN					
201-11	RT: EN					
Fe(III)red	RT: EN	RT: EN		RT: EN		RT: EN
Mn(IV)red	RT: EN	RT: EN		RT: EN		RT: EN

Notes: Enrichment assays were qualitative (EN) or quantitative (MPN) and incubated at the temperature given and/or at room temperature (RT = 21°–25°C). Media are defined in Table T9, p. 90, in the “Explanatory Notes” chapter (see also “Microbiology,” p. 14, Table T4, p. 84, T5, p. 85, and T7, p. 88, all in the “Explanatory Notes” chapter).

Table T9. Downhole temperature measurement summary, Hole 1228A.

Depth (mbsf)	Tool	Measurement location	Thermal conductivity (W/[m-K])	Temperature (°C)	Assessment
0.0	Adara	Seafloor, T Core 201-1228E-1H	—	13.7	Possible annual variation
0.0				12.5 [†]	
24.8	Adara	Core 112-680C-3H	—	13.3	
34.0	Adara	Core 112-680B-4H	—	13.8	
42.0	DVTP	B Core 201-1228A-5H	—	15.8	Curve wrong shape; value too high
80.9	DVTP 2	B Core 201-1228A-9H	0.93	15.2	Good
137.9	DVTP	B Core 201-1228A-16H	—	—	No decay profile; large oscillations
194.9	DVTP 1	B Core 201-1228A-22H	1.13	19.1	Good
200.9	—	—	0.96*	19.3 [†]	

Notes: DVTP = Davis-Villinger Temperature Probe. T = top of core, B = bottom of core. — = not applicable. * = average thermal conductivity, † = projected temperatures at seafloor and base of hole. The last line shows the temperature extrapolated to basement using linear fit in Figure F20, p. 54, and the mean thermal conductivity computed from data plotted in Figure F18A, p. 52.

Table T10. Detail of logging operations, Hole 1228A.

Date (Mar 2002)	UTC (GMT - 7 hr)	Tool depth (mbsf)	Remarks
5	1300		End of coring
5	1300-1715		Wiper trip; hole displaced with 100 bbl of sepiolite; bottom of pipe set at 80 mbsf
5	1715-1900		Logging rig-up
5	1930		Start going downward with triple combination tool string: TAP/DIT-E/HLDT/APS/HNGS/SGT
5	2000	0	Stop 5 min at mudline for temperature calibration
5	2010	80	Tool string in open hole
5	2025	201	Tool at TD; start logging upward at 900 ft/hr
5	2040		Pipe raised by 10 m
5	2045	70	Tool back inside pipe; speed up to 1500 ft/hr to log mudline
5	2100	0	Mudline indicated by gamma ray at 276 m below rig floor
5	2105	-21	End of pass 1; standing 5 min and start going back downward
5	2115	70	Tool string in open hole
5	2125	201	Tool at TD; start logging upward pass 2 at 900 ft/hr
5	2155	70	Tool back inside pipe
5	2200	51	End of pass 2; speed up to 8000 ft/hr
5	2225	0	Tool back on rig floor
5	2400		Finish rig-down

Notes: UTC = Universal Time Coordinated. TD = total depth. TAP = LDEO Temperature/Acceleration/Pressure tool, DIT-E = Dual Induction Tool, HLDT = Hostile Environment Litho-Density Tool, APS = Accelerator Porosity Sonde, HNGS = Hostile Environment Gamma Ray Sonde, SGT = Scintillation Gamma Ray Tool.